

# **POLITECNICO DI TORINO**

## **Master's Degree in Civil Engineering**



### **Master Thesis**

# **Scale Effects on Fracture Energy: Experimental Investigation and Comparison with RILEM Recommendation**

#### **Tutors**

Prof. Alberto CARPINTERI

Prof. Giuseppe LACIDOGNA

Dr. Federico ACCORNERO

Dr. Gianfranco PIANA

**Candidate**

Davide BARONE

**Academic Year 2017-2018**

*A Dalila*

## **Ringraziamenti**

Desidero ringraziare i miei relatori per la loro disponibilità e la loro costante guida nello sviluppo di questa tesi.

Voglio inoltre ringraziare il mio professore di storia e filosofia Giuseppe Scaramuzzo, i cui insegnamenti e il cui metodo di studio e di ricerca sono stati strumenti fondamentali nel corso dei miei studi.

Il ringraziamento più grande va però alla mia famiglia, papà, mamma e Dalila, i quali, nonostante la lontananza, sono sempre stati al mio fianco vivendo insieme a me tutti i momenti di gioia e le difficoltà che hanno caratterizzato questi anni di università, trasmettendomi la forza necessaria per raggiungere questo traguardo.

## Abstract

The aim of the present thesis is to analyse the scale effects on fracture energy and tensile strength of plain concrete. The former is the amount of energy necessary to create a unit area of a crack, and gives a measure of the material fracture toughness; the latter represents the force per unit area that causes the failure. These two material parameters, together with a geometric dimension of the structure, can describe the global structural behaviour, e.g., by means of brittleness numbers.

Fracture energy and tensile strength are often considered as material properties in concrete fracture mechanics. For instance, the cohesive crack model considers the cohesive law, i.e. the diagram in which cohesive stress is represented as a function of the crack opening displacement, as an intrinsic material property, and consequently the fracture energy, that is equal to the area under this diagram, is a parameter independent from the structural size, geometry and loading condition. According to this model, RILEM TC 50-FMC proposed an experimental method to determine the fracture energy of concrete. It consists in a three-point bending test, performed by using pre-notched specimens with recommended sizes, depending on the maximum diameter of the aggregate.

However, many experimental results demonstrate how the fracture energy and the tensile strength of quasi-brittle materials such as concrete are size dependent, and so they cannot be considered as material properties, unless they are evaluated on very large specimens. It was observed that fracture energy and toughness of concrete increase with the specimen size, whereas the tensile strength decreases. This phenomenon has been studied with intensive research activities, at least for two reasons: (i) experimental results obtained with tests performed on laboratory-size specimens cannot be easily extrapolated to large-scale concrete structures without a careful understanding of size effect; (ii) it is impossible for most laboratories to perform tests directly on large structure-like specimens. Many researchers have dealt with this problem, and many theories have been proposed in order to provide a theoretical explanation and a predictive model of the scale effects on fracture parameters.

In the first part of this work, after a short review of fracture mechanics fundamentals, a description of the principal scale effect models is presented. Particular attention is reserved to the fractal model proposed by Carpinteri: this will be used in the second part of the present thesis to interpret some experimental results. The fractal model explains scale effects by considering the fractal nature of fracture surfaces in disordered materials with a multi-scale heterogeneity. In fact, defining the tensile strength of concrete as a force on a surface with a fractal dimension lower than 2 (lacunar fractal), and the fracture energy as an energy dissipated on a surface having a dimension higher than 2 (invasive fractal), two renormalized size-independent properties of the material can be defined.

In the present work, three-point bending tests have been performed on plain concrete pre-notched specimens of different sizes. RILEM Recommendation was followed for the testing procedure and for the evaluation of fracture energy and bending strength. Scale effects on these two parameters were observed, and the fractal model was applied in order to define two power laws able to express these two parameters as a function of the beam depth and the corresponding fractal material property.

Furthermore, a renormalization procedure has also been extended to the kinematic aspect of the problem, taking into account the rotation angle of the mid-span section in the critical situation immediately before the final collapse. Thus a fractal cohesive law has been defined: it is function of the three size-independent renormalized values of fracture energy, bending strength and rotation angle.

Moreover, during the tests, two non-destructive techniques of damage monitoring were used: Dynamic Identification and Acoustic Emission analysis.

The former consisted in the evaluation of variations in the natural bending frequencies during damage progress; this was done in practice by analysing the free response signals consequent to external impulsive forces, for different loading steps.

On the other hand, the Acoustic Emission (AE) technique is based on the acquisition of the ultrasonic signals generated by cracks formation and extension in the bulk of the material. Crack classification was performed using the Rise Angle procedure. Moreover scale effects on the AE energy were observed, and described by a power law. Unlike the fracture energy, that is an energy dissipated in an invasive fractal domain, the AE energy seems to be an energy emitted in a lacunar fractal domain: the difference between the two physical fractal dimensions represents a further demonstration of the absence of correlation between dissipated and emitted energy.

# Table of contents

Ringraziamenti .....	II
Abstract .....	III
Introduction.....	1
1 Fundamental concepts .....	2
1.1 Fracture mechanics and scale effects on tensile strength and fracture energy .....	2
1.1.1 Review of Fracture Mechanics.....	3
1.1.1.1 Review of Linear Elastic Fracture Mechanics.....	3
1.1.1.2 Cohesive crack models .....	9
1.1.1.3 Scale effects and snap-back phenomenon .....	12
1.1.1.4 Experimental determination of fracture energy of concrete according to RILEM Recommendation .....	20
1.1.2 Review of scale effect models .....	23
1.1.2.1 Historical development of the principal scale effect models .....	24
1.1.2.2 Fractal model for scale effects on tensile strength and fracture energy .....	35
1.2 The Acoustic Emission Technique .....	45
1.2.1 General aspects.....	45
1.2.2 Parametric AE Analysis: Crack classification.....	48
1.3 Dynamic Identification .....	50
1.3.1 Non-destructive control based on vibrations .....	51
2 Experimental campaign and results .....	53
2.1 Outline of experiments .....	53
2.1.1 Test set-up (RILEM TC50-FMC Recommendation).....	54
2.1.1.1 Specimens characteristics.....	55
2.1.1.2 Material properties .....	56
2.1.2 Sensors and instruments .....	57
2.2 Numerical (FEM) models.....	59
2.2.1 Numerical bending modes and related natural frequencies .....	60
2.2.2 Numerical evaluation of the modal frequency variation during the crack growth.....	62
2.2.3 Numerical load-displacement curves .....	65
2.3 A scale-independent fractal cohesive law for bending .....	70

2.3.1	Experimental results: Load-deflection curves .....	70
2.3.2	Scale effects on bending strength.....	74
2.3.3	Scale effects on fracture energy .....	76
2.3.4	Renormalized load-deflection curves.....	78
2.3.5	Scale effects on the critical rotation angle: Kinematic aspects .....	79
2.4	Damage monitoring by Acoustic Emission and modal frequency analysis ...	83
2.4.1	AE Analysis .....	84
2.4.1.1	Cumulated AE energy .....	85
2.4.1.2	Characterization of the fracture mode by Rise Angle value and Average Frequency .....	87
2.4.1.3	Scale effects on the specific AE energy: A fractal explanation .....	89
2.4.2	Modal frequency variation.....	91
2.4.3	Correlations between the two monitoring techniques .....	100
2.5	Comparison between three and four point bending results .....	102
	Conclusions.....	104
	References .....	105

## Introduction

Scale effects in concrete and non-destructive damage monitoring techniques are the main topics of this thesis work.

The thesis has been divided into two parts.

The first part contains a review of the main concepts concerning Fracture Mechanics and the two damage monitoring techniques applied during the experimental campaign, namely Acoustic Emission (AE) and Dynamic Identification (DI). In section [1.1] the fundamental concepts of linear and non-linear Fracture Mechanics are reviewed; particular attention is given to the scale effects on the structural behaviour. After a brief description of the principal scale effect models, the fractal scaling laws and the renormalization procedure proposed by Carpinteri for fracture energy and tensile strength are presented in detail. Furthermore, the experimental method recommended by RILEM TC 50 – FMC to evaluate the fracture energy of concrete is described. Section [1.2] is about the AE analysis, while section [1.3] briefly explains the theoretical basis of damage monitoring techniques based on the dynamic response of the structure.

In the second part of the thesis, the experimental results obtained during three-point bending tests are discussed. Four different scales of plain concrete specimens are considered. In section [2.1], the experimental set-up is described. Section [2.2] shows the numerical (FEM) results concerning the natural frequencies of the specimens in both the initial configuration and the damaged configuration. The experimental results are presented in section [2.3]. Fractal scaling laws are defined for fracture energy, bending strength and rotation angle of the mid-span section in correspondence to the final failure. A scale independent cohesive law is eventually proposed for bending. Section [2.4] is a focus on the results of AE analysis and on the modal frequency variations for the different specimen sizes. Correlations between these two techniques are shown, highlighting their pros and cons. In section [2.5], the results of three and four-point bending tests made on specimens of the same size are compared, in order to emphasize the differences in terms of stability of the crack propagation process.

# 1 Fundamental concepts

## 1.1 Fracture mechanics and scale effects on tensile strength and fracture energy

After the introduction of Fracture Mechanics, the classical concept of strength was completely reconsidered. The ductility of a material can be described by introducing the concept of toughness. It represents the capacity of material to oppose the fracture propagation.

Nevertheless, it is necessary to distinguish the ductility of a material from the ductility of a structure. The former depends only on the intrinsic characteristics of the material (strength and toughness), the latter depends also on the size of the structure.

In compressed structures there is a transition between plastic collapse and buckling that depends on the slenderness of the structure. An interaction between two different collapse phenomena exists also in tensed structures, in which the transition from plastic to brittle collapse, in this case, is a function of the dimensional scale of the structure.

In particular, a ductile behaviour can be associated to relatively small structures, whereas a brittle behaviour, with an unstable crack propagation, characterizes the larger ones. This concept is expressed in Figure 1.1 (Carpinteri, 1992), where three notched beams under a three point bending test in laboratory are considered as an example. Even though the material is the same, the ductile-brittle transition appears clearly with the increasing of the element dimension.

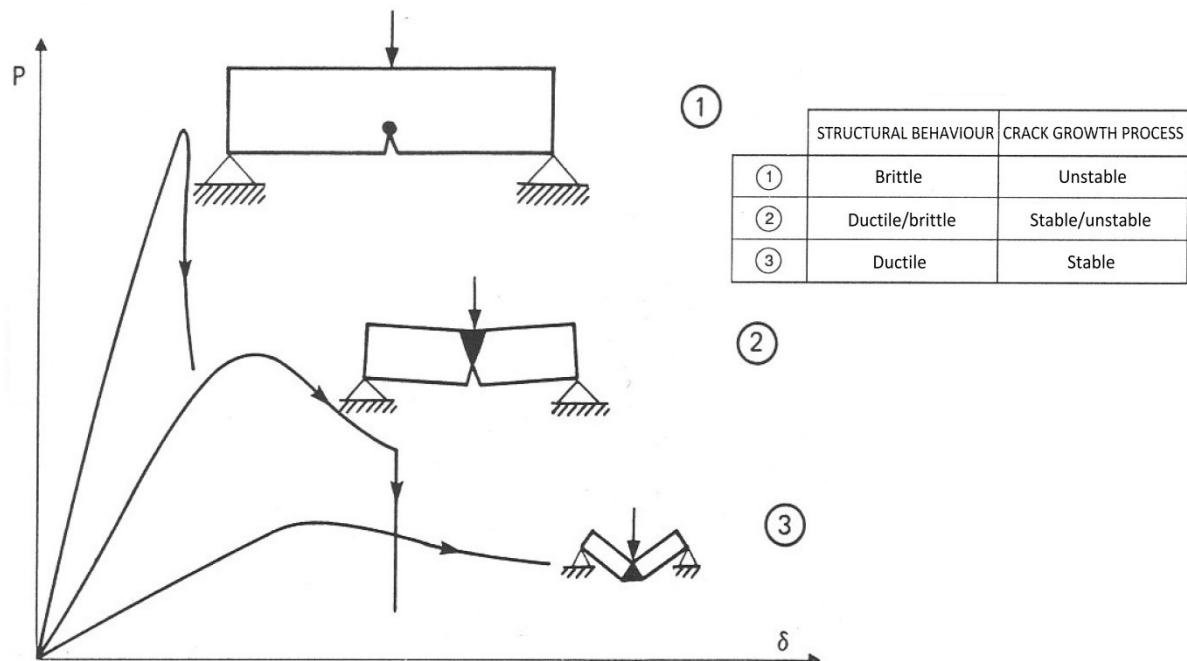


Figure 1.1 – Ductile-brittle transition with the increase of specimen size

In the following, some of the models introduced in Fracture Mechanics to explain and quantify the scale effects will be discussed. In particular, brittleness numbers are defined in order to describe the ductility of a structure with a single value. After a brief historical introduction in which different models proposed by different authors will be mentioned, particular attention will be given to the fractal model proposed by Carpinteri to explain the size effect on tensile strength and fracture energy of disordered materials like concrete. The fractal model will be used in Part II to interpret the experimental results.

### **1.1.1 Review of Fracture Mechanics**

In this paragraph the main concepts of Fracture Mechanics will be reported, starting from the classical linear theory up to the nonlinear ones. If the use of these concepts is already consolidated in the design of metal structures, their application in the field of quasi-brittle materials is very recent. Only during the late 1970s and the 1980s the research effort was dedicated to adapt the foregoing models to these materials, and to find experimental methods for the measure of the new parameters introduced in order to describe the heterogeneous nature especially of concrete.

The application of Fracture Mechanics into concrete design becomes important especially for the large size structures such as dams or nuclear reactor containments, because it may allow a better evaluation of safety coefficients with a consequent gain both in economic terms and in structure reliability.

Special comments will be reserved in section [1.1.1.2] for Hillerborg's fictitious crack model (Hillerborg, Mod er and Petersson, 1976) which was introduced for concrete. In section [1.1.1.3] the snap-back instability will be described for relatively large scales, together with brittleness numbers. In the last section [1.1.1.4] the technique provided by RILEM Recommendation to determine the fracture energy of mortar and concrete will be presented.

#### *1.1.1.1 Review of Linear Elastic Fracture Mechanics*

In this section a brief summary of the main concepts of Linear Elastic Fracture Mechanics (LEFM) is reported. Even though it represents a widely used basic tool for study the fracture in brittle conditions, LEFM can give good predictions only when the structure remains elastic, for the most part, up to the crack initiation. This is the reason why it is necessary to introduce nonlinear models to study the fracture in concrete or other quasi-brittle materials.

The stimulus for Fracture Mechanics arrived from a paper of Inglis (1913) in which an elastic solution is derived for the evaluation of stresses at the vertex of an ellipsoidal defect in an infinite solid subjected to tension. Previously, in 1898, Kirsch studied the problem of a circular cavity in an infinite slab subjected to tension: he found at the edges of the hole a stress concentration factor equal to 3 when the slab is subjected to uniaxial tension (Figure 1.2a). In the same situation, but in presence of an elliptical

defect, the stress concentration factor evaluated by Inglis is:  $(1 + 2 \cdot a/b)$ , where  $a$  and  $b$  are respectively the major and the minor semi-axes of the ellipse (Figure 1.2b). In other words, if the tensile strength of the material is  $\sigma_p$ , an infinite slab with an elliptical hole subjected to an uniaxial tension will collapse when the stress is equal to:

$$\sigma_{max} = \frac{\sigma_p}{(1 + 2 \cdot a/b)} \quad (1.1)$$

From Eq. (1.1), Kirsch's result can be obtained posing  $a = b$  (circular defect).

The stress concentration factor proposed by Inglis increases with increasing of the eccentricity of the ellipse: at the limit, when  $b \rightarrow 0$  and so  $a/b \rightarrow \infty$ , this factor tends to infinit (Figure 1.2c). Looking again at Eq. (1.1), it means that a slab subjected to tension with a linear crack has no resistance. However, this result is absurd. This means that the results proposed by Inglis cannot be applied to the fracture problem.

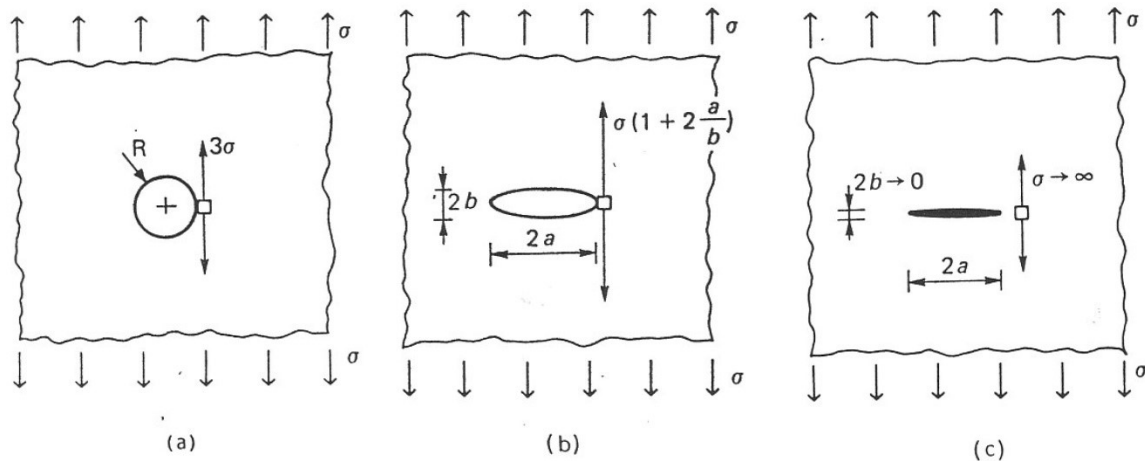


Figure 1.2: Stress concentration factor for different shapes of defects

The problem was overcome a few years later by Griffith (1921). He also thought that the fracture arises from pre-existing defects in the material. However, he proposed an energy failure criterion, introducing the concept of fracture energy, i.e. a parameter able to describe the material toughness. Thus, the distinction between strength and toughness became evident. Griffith considered a plate in plane stress conditions, subjected to a constant stress  $\sigma$ , containing a crack with a length  $2a$ . He assumed that the plate width is much larger than  $2a$ , so that  $a$  is the only geometric parameter of the problem. In order to have an increase of crack size, the potential energy in the plate must be sufficient to exceed the surface energy of the material; in other words, the elastic energy released for an incremental increase in the crack length,  $da$ , must overcome or be equal to the energy required for the formation of the new free surface:

$$\frac{dW_e}{da} \geq \frac{dW_s}{da} \quad (1.2)$$

where  $W_e$  is the elastic strain energy released by the uniformly stressed slab of unit thickness when a crack  $2a$  long is made. Griffith demonstrated that:

$$W_e = \pi \cdot a^2 \cdot \frac{\sigma^2}{E} \quad (1.3)$$

$W_s$  is instead the dissipated surface energy required to create a new fracture  $2a$  long:

$$W_s = 4 \cdot a \cdot \gamma \quad (1.4)$$

where  $\gamma$  is an energy per unit of area.

Substituting Eq. (1.3) and Eq. (1.4) in Eq. (1.2), and introducing the fracture energy:

$$G_F = 2 \cdot \gamma \quad (1.5)$$

Griffith obtained the following instability condition, represented in Figure 1.3:

$$\sigma \geq \sqrt{\frac{G_F \cdot E}{\pi \cdot a}} \quad (1.6)$$

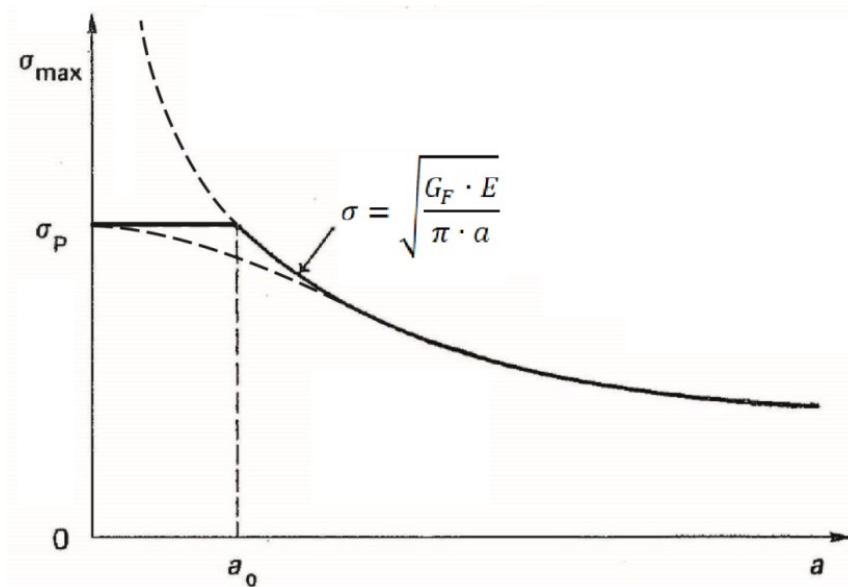


Figure 1.3: Ductile-to-brittle transition as a function of the half-length of the crack

The curve represented in Figure 1.3 has two asymptotes. The first one is horizontal: it means that slab resistance decreases with the increasing of crack length. The second one is vertical: it means that a slab without any cracks has infinite resistance. However, this latter result is wrong. The material has in fact its own resistance, indicated with  $\sigma_p$ . Thus a cut-off of the curve must be applied in correspondence of  $\sigma = \sigma_p$ . In this way a parameter  $a_0$ , only function of material properties, is obtained:

$$a_0 = \frac{1}{\pi} \cdot \frac{G_F \cdot E}{\sigma_p^2} \quad (1.7)$$

It represents the half-length of equivalent micro defect pre-existing in the material, and it can be seen as a measure of fracture material sensitivity. In fact:

- if  $a < a_0$  the slab will fail for plastic collapse, because the crack is too small and does not influence the material behaviour;
- if  $a > a_0$  the slab will fail for brittle fracture in correspondence of an external stress  $\sigma < \sigma_p$ .

Figure 1.3 shows clearly the analogy, already discussed at the beginning of section [1.1], between the unstable crack propagation, related to structures subjected to tension, and the instability of elastic equilibrium (Euler's hyperbole in Figure 1.4), related to structures subjected to compression.

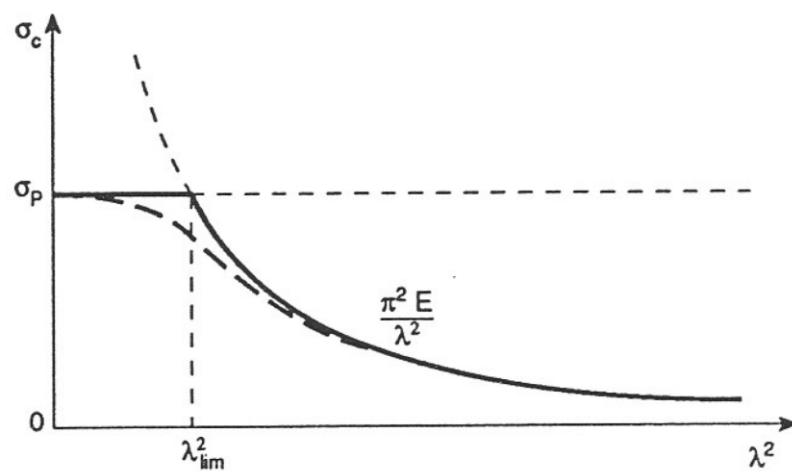


Figure 1.4: Transition from plastic collapse to buckling in compressed structures as a function of slenderness

Furthermore, Eq. (1.7) underlines that the tensile strength  $\sigma_p$  is not a material property, because it is a function of the half-length of equivalent micro defect pre-existing in the material.

The concept of stress concentration factor, used e.g. by Inglis in the study of the effects of an elliptical defect in a body subjected to tension, was therefore substituted, in the study of fractures, by the stress intensity factor: in correspondence of the crack tip, in fact, the stress tends to infinit. This singularity was determined by Westergaard (1939) with his method of complex potentials, and also by Williams (1952) with his series expansion method. In the immediate vicinity of the crack tip (i.e. for  $r \ll a$  with  $r$  horizontal coordinate with origin in correspondence of the crack tip) the stress in the perpendicular direction of the fracture is:

$$\sigma_Y = \frac{K_I}{\sqrt{2 \cdot \pi \cdot r}} \quad (1.8)$$

in which  $K_I$  is the stress intensity factor (the symbol “I” is referred to a mode I fracture: the crack classification will be discussed in section [1.2.2]). This factor depends on the boundary conditions (geometry of the problem, external loads, etc.), the dimensions of the structure and of the crack. In particular, in an infinite slab with a crack  $2a$  long, uniformly tensed by an external stress  $\sigma$  (Figure 1.5), it is equal to:

$$K_I = \sigma \cdot \sqrt{\pi \cdot a} \quad (1.9)$$

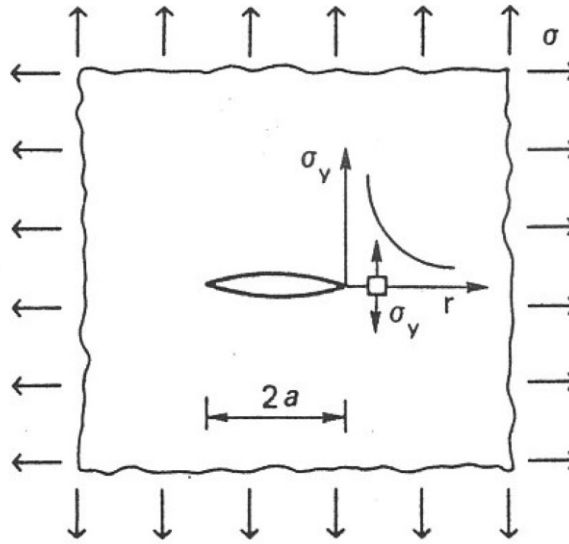


Figure 1.5: Stress intensification near the crack tip

The physical dimensions of  $K_I$  are unusual:  $[F] \cdot [L]^{-3/2}$ . This fact can be considered as a fundamental reason of the scale effects already discussed at the beginning of section [1.1]. Changing the geometry of the problem and the boundary conditions (loads and constraints), Eq. (1.9) must be substituted by:

$$K_I = \sigma \cdot \sqrt{\pi \cdot a} \cdot F \quad (1.10)$$

where  $F$  is a shape function that depends on the geometry of the problem. It is usually evaluated by a polynomial expression, function of the crack length and of the characteristic dimension of the structure. Some of these empirical formulas can be found in Tada, Paris, Irwin (1985) for the most common test specimens configurations. For instance, for a three-point bend (TPB) test specimen with a ratio  $S/b = 8$  (Figure 1.6a), Eq. (1.11) can be used:

$$F\left(\frac{a}{b}\right) = 1.106 - 1.552 \cdot \left(\frac{a}{b}\right) + 7.71 \cdot \left(\frac{a}{b}\right)^2 - 13.53 \cdot \left(\frac{a}{b}\right)^3 + 14.23 \cdot \left(\frac{a}{b}\right)^4 \quad (1.11)$$

Instead for a four-point bend (FPB) test specimen with a ratio  $a/b \leq 0.6$  (Figure 1.6b) it is possible to use Eq. (1.12), relative to a pure bending specimen:

$$F\left(\frac{a}{b}\right) = 1.122 - 1.40 \cdot \left(\frac{a}{b}\right) + 7.33 \cdot \left(\frac{a}{b}\right)^2 - 13.08 \cdot \left(\frac{a}{b}\right)^3 + 14.0 \cdot \left(\frac{a}{b}\right)^4 \quad (1.12)$$

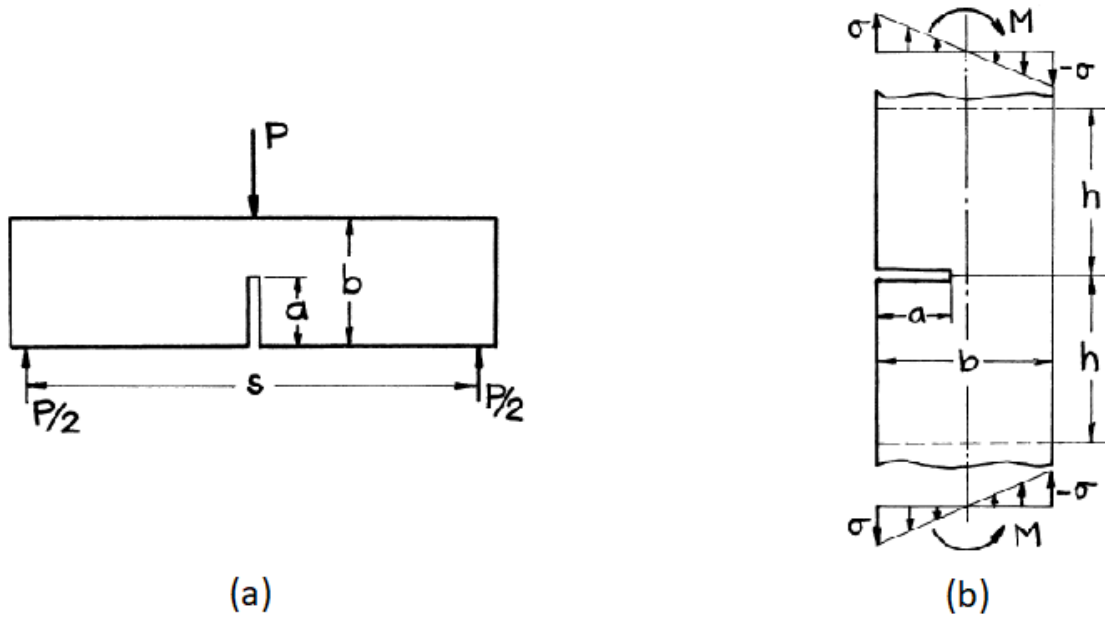


Figure 1.6: (a) TPB test and (b) pure bending specimens

When the stress intensity factor reaches its critical value  $K_{IC}$ , the unstable fracture propagation occurs.  $K_{IC}$  is usually considered as a material property, and it represents the material toughness. Using Eq. (1.8), and supposing that Eq. (1.9) can be used to express  $K_I$ , the instability condition becomes:

$$\sigma_Y = \frac{\sigma \cdot \sqrt{\pi \cdot a}}{\sqrt{2 \cdot \pi \cdot r}} \geq \frac{K_{IC}}{\sqrt{2 \cdot \pi \cdot r}} \quad (1.13)$$

and consequently:

$$\sigma \geq \frac{K_{IC}}{\sqrt{\pi \cdot a}} \quad (1.14)$$

Comparing the conditions (1.6) and (1.14), it is possible to conclude that:

$$K_{IC} = \sqrt{G_F \cdot E} \quad (1.15)$$

Eq. (1.15) expresses the relationship between the fracture energy and the critical value of the stress intensity factor. This fundamental result, that correlates the energy criterion of Griffith with the tensile approaches, was proposed in 1957 by Irwin. For this reason Eq. (1.15) is known as Irwin's relationship. Moreover he generalized the energy criterion of Griffith, proving its independence from the geometry and the loading process; he also defined the strain energy release rate  $G_I$  as the total potential energy per unit increment of fracture area, and demonstrated how Eq. (1.15), expressed in critical terms, can be rewritten also for general values of  $G_I$  and  $K_I$ .

### 1.1.1.2 Cohesive crack models

Even though LEFM represents the basic theory for the analysis of many structural problems, its application must be limited for materials that remain elastic up to the brittle propagation of fracture. The singularity  $r^{-1/2}$  that involves the stresses in presence of a fracture actually does not exist before a certain distance from the crack tip. In this region, in fact, plastic phenomena occur. For this reason the real value of the stress is lower than the theoretical one, because it remains equal to the tensile strength of material (Figure 1.7).

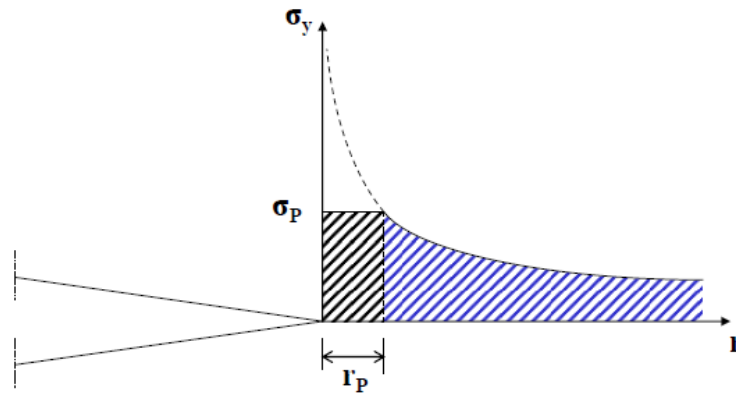


Figure 1.7: Plasticization of the material near the crack tip

Thus, around the crack tip, a plastic region develops. It can reach an important extension in materials that exhibit a ductile behaviour. Irwin (1960) demonstrated that, at the onset of crack propagation, this region has an extension:

$$a_{PC} = \frac{1}{\pi} \cdot \frac{K_{IC}^2}{\sigma_p^2} \quad (1.16)$$

Another evaluation of the size of the yielding zone at the crack tip in correspondence of the collapse was proposed by Dugdale (1960):

$$a_{PC} = \frac{\pi}{8} \cdot \frac{K_{IC}^2}{\sigma_p^2} \quad (1.17)$$

A fracture can be considered brittle when the plastic zone is much smaller than the pre-existing crack length and the structural dimension:

$$a_{PC} \ll a \quad (1.18)$$

$$a_{PC} \ll D \quad (1.19)$$

where  $D$  represents a characteristic dimension of the structure.

Generally this happens in many metallic materials, in which LEFM is usually available. In these cases the stresses in the plastic zone can be assumed increasing or constant at the increasing of the external loads. On the other hand, the Fracture Process Zone (FPZ) in concrete can assume a large size, and the stresses inside it

decrease with the increase of external loads. For these reasons, LEFM becomes unsuitable for materials such as concrete or tough steels, able to develop large yielding zones close to the crack tip before the unstable propagation.

Starting from the 1960s, various non-linear theories were proposed for the Fracture Mechanics. They can be distinguished into two major categories: the equivalent elastic crack models and the cohesive crack models. The latter, in particular, were developed just to simulate what really happens in the process zone of concrete. During the crack opening, from one face of the fracture to the other, stresses are still transferred. Barenblatt (1959) was the first to propose a cohesive model: in order to simulate the interatomic forces between the two crack faces, he introduced in this model distributed cohesive stresses, only in a small region near the crack tip; the values of these stresses were function of the separation between the fracture faces. Another important cohesive model was proposed by Dugdale (1960): unlike the Barenblatt's model, in which the microscopic atomic interaction was considered, in this case the goal was to simulate the macroscopic plasticity; in particular, a constant distribution of yield stresses (perfectly plastic behaviour) were introduced in the cohesive zone of a linear crack. Afterwards, other cohesive crack models have been developed with various names, in order to exceed the limits of LEFM, that moreover is able to describe crack propagation but not the crack initiation (in other words it inevitably needs the presence of a pre-existing defect). Among these, Hillerborg's fictitious crack model (Hillerborg, Mod er and Petersson, 1976) deserves particular attention. It was thought for concrete, and it can be applied also to initially uncracked solids. In this model the fracture zone develops at one point when the first principal stress reaches the tensile strength (Petersson, 1981). The fracture zone of a non-yielding material is characterized by a lot of micro-cracks, which make this zone weaker. Even though this part of material is partially destroyed, a stress transfer takes place between the two faces, until their distance is less than a certain value. These bridging stresses are physically due to zigzag cracking, aggregate interlocking, crack branching and eventually to the presence of fibers. The fracture zone, in which these interaction phenomena occur, is not a real fracture: indeed this crack, able to transfer stresses, is a fictitious crack (Figure 1.8). For this reason Hillerborg's model is known as Fictitious Crack Model. The value of these bridging stresses depends on the width of the fracture. In correspondence of a distance  $w_c$  between the slit faces the interaction is null. To describe correctly the stress-deformation properties of the non-yielding materials, two constitutive laws are therefore necessary:

- a relation between stress and relative strain ( $\sigma - \varepsilon$  curve: Figure 1.9a) to describe the deformation properties of the material outside the process zone;
- a relation between the stress and the widening of the crack in the stressed direction ( $\sigma - w$  curve: Figure 1.9b) to describe the deformation properties of the fracture zone.

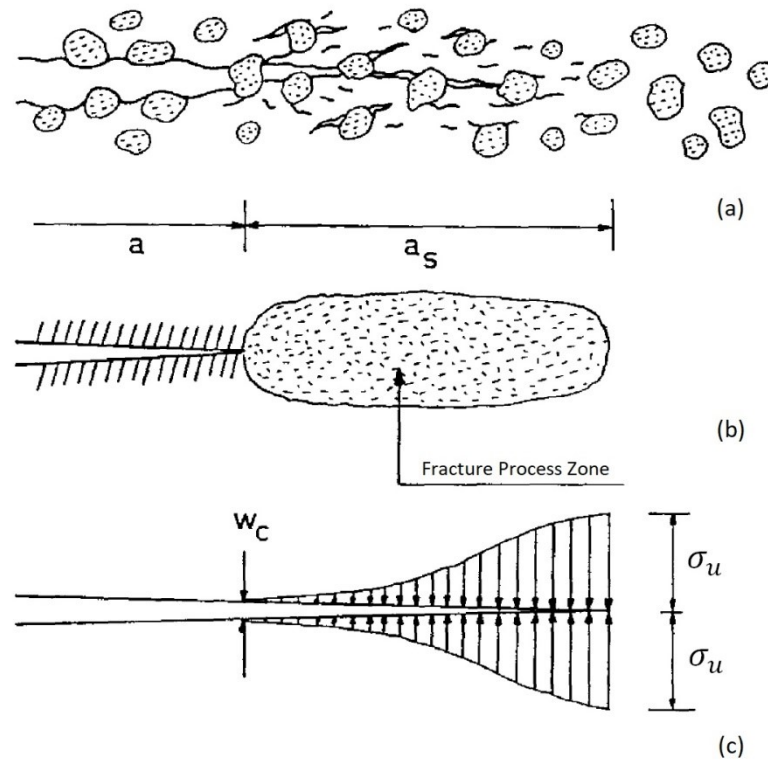


Figure 1.8: Fictitious Crack Model: (a) crack tip process zone, (b) damage zone in front of the real crack tip, (c) cohesive forces behind the fictitious crack tip

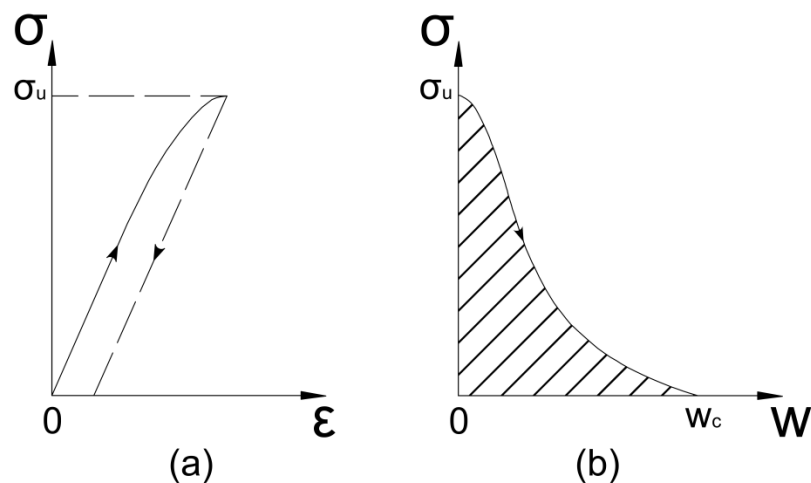


Figure 1.9: Double constitutive law: (a) stress-strain, (b) stress-crack opening displacement

While in materials with an elastic-hardening-softening behaviour like steel the energy is dissipated both on the fracture surfaces and in the whole volume of the solid, in materials with an elastic-softening behaviour like concrete the dissipation takes place only on the fracture faces. The strains, in materials with an elastic-softening behaviour, are not uniform in the body: they are localized in correspondence of the crack. Hence the softening branch in the  $\sigma - \epsilon$  diagram of brittle materials (Figure 1.10) depends on the characteristic dimension of the body.

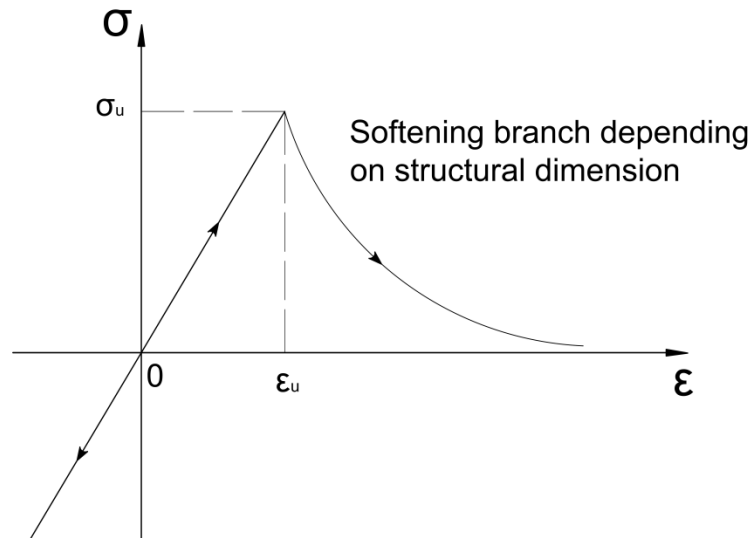


Figure 1.10: Elastic-softening behaviour of brittle materials for tensile stresses

A true material property is instead the cohesive law  $\sigma(w)$  (Figure 1.9b). The area under this curve is the fracture energy (Eq.(1.20)); consequently it is an intrinsic property of the material:

$$G_F = \int_0^{w_c} \sigma dw \quad (1.20)$$

Therefore in Hillerborg's model the real crack must be distinguished from the cohesive (or fictitious) crack. An extremity of this latter corresponds to the point in which the widening is equal to  $w_c$  and the bridging stresses are equal to zero, while the other one is the beginning of the process zone, where the cohesive stress is equal to the tensile strength (Figure 1.8c). The values of the cohesive stresses in the intermediate points of the fictitious crack can be deduced according to the  $\sigma - w$  curve (Figure 1.9b).

### 1.1.1.3 Scale effects and snap-back phenomenon

For sake of simplicity, a tensile test on a specimen with an initial length  $l_0$  is considered. If the material has an elastic-softening behaviour (e.g., concrete) the energy dissipated on the fracture surfaces, equal to  $G_F \cdot A_0$  (where  $A_0$  is the fracture area, corresponding for this kind of test to the initial area of the specimen cross section), corresponds to the energy dissipated in the whole volume  $l_0 \cdot A_0$ , because the dissipation in such materials is localized only in correspondence of the crack. If the test is performed on specimens with different length  $l_0$ , the curves  $F - \Delta l$  shown in Figure 1.11 will be obtained (Carpinteri, 1992). Since the area under each of these curves must be equal to the total dissipated energy, that is  $G_F \cdot A_0$ , a smaller elastic modulus and a softening branch (also called negative hardening branch) with an increasing negative slope will be obtained with the increase of the specimen length. For considerable specimen lengths, the slope of the softening branch can even become positive.

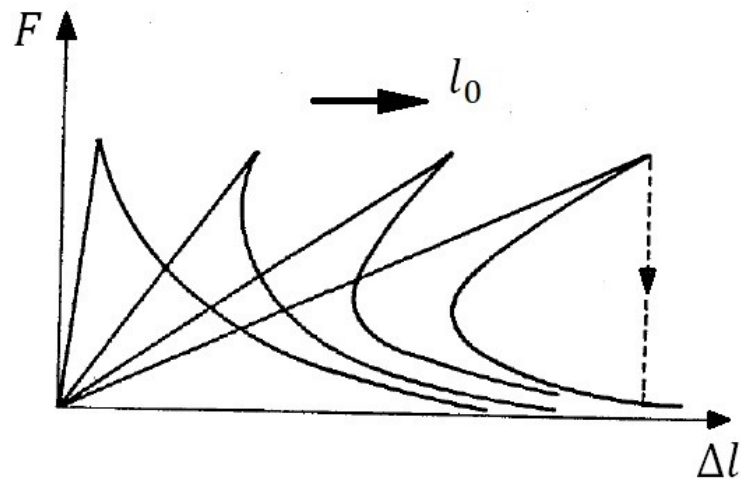


Figure 1.11: Scale effects on the diagram  $F - \Delta l$  in a tensile test on a brittle material

When the maximum load during the test is reached, the whole specimen is subjected to the maximum stress represented by point A in Figure 1.12. In a certain section (probably in the middle) a crack begins to propagate: from this moment on, the intact material away from the fracture is subjected to an elastic unloading, according to the  $\sigma - \varepsilon$  curve (point B in Figure 1.12a), while the stress in a point inside the fracture zone decreases according to  $\sigma - w$  curve (point B in Figure 1.12b) as a function of the widening  $w$ .

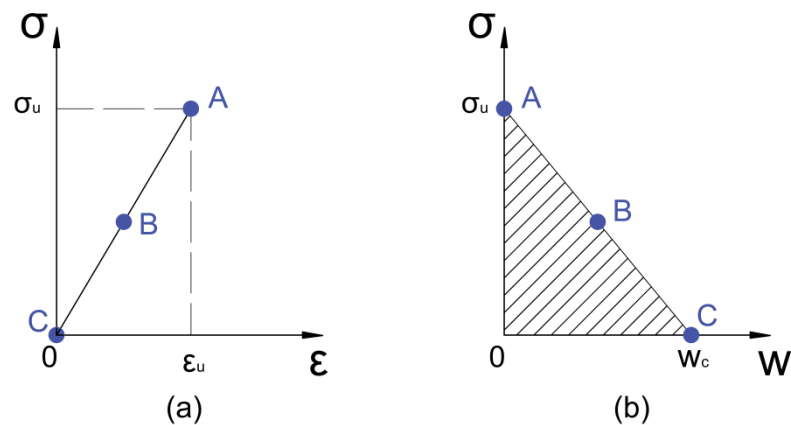


Figure 1.12: Different phases of a tensile test on a brittle material represented on the two constitutive laws, supposed linear

If the initial length  $l_0$  is large enough, the elastic shortening of the intact material due to the elastic unloading can prevail on the widening  $w$  of the crack: in these cases, a softening branch with a positive slope can be obtained. This represents a catastrophic phenomenon, because, even if the test is performed by controlling the displacement, a sudden load drop can happen. This loss of stability in controlled displacement condition is called *snap-back* instability, and it can experimentally be observed only if the test is performed by controlling the crack mouth opening

displacement  $w$ . The conditions that contribute to the occurrence of this phenomenon are: the low material toughness, the high tensile strength and large dimensional scales. As it has already been anticipated, while the tensile strength and fracture energy are considered as material properties in the cohesive model, the structure ductility depends on the scale.

A first scale effect, already discussed in section [1.1.1.1], concerns the crack length: if  $a > a_0$ , where  $a_0$  is a function of material properties (Eq. (1.7)), the unstable crack propagation precedes the plastic collapse. A second scale effect is related to the absolute dimensions of the cracked structure: if geometrically similar solids, made of the same material, characterized by a crack length proportional to the characteristic dimension of the solid, are tensed up to the failure, the collapse mechanism could be different, depending on the absolute dimension of the solid (Carpinteri, 1992).

In a three-point bend test (Figure 1.13), for example, the failure for brittle fracture happens when the stress  $\sigma$  satisfies the criterion in Eq. (1.14), in which  $K_{IC}$  can be expressed, for the TPB geometry, also in the form:

$$K_{IC} = \frac{F_{max} \cdot S}{B \cdot D^{3/2}} \cdot f\left(\frac{a}{D}\right) \quad (1.21)$$

where the shape function  $f$  can be evaluated using the following polynomial expression:

$$f\left(\frac{a}{D}\right) = 2.9 \cdot \left(\frac{a}{D}\right)^{\frac{1}{2}} - 4.6 \cdot \left(\frac{a}{D}\right)^{\frac{3}{2}} + 21.8 \cdot \left(\frac{a}{D}\right)^{\frac{5}{2}} - 37.6 \cdot \left(\frac{a}{D}\right)^{\frac{7}{2}} + 38.7 \cdot \left(\frac{a}{D}\right)^{\frac{9}{2}} \quad (1.22)$$

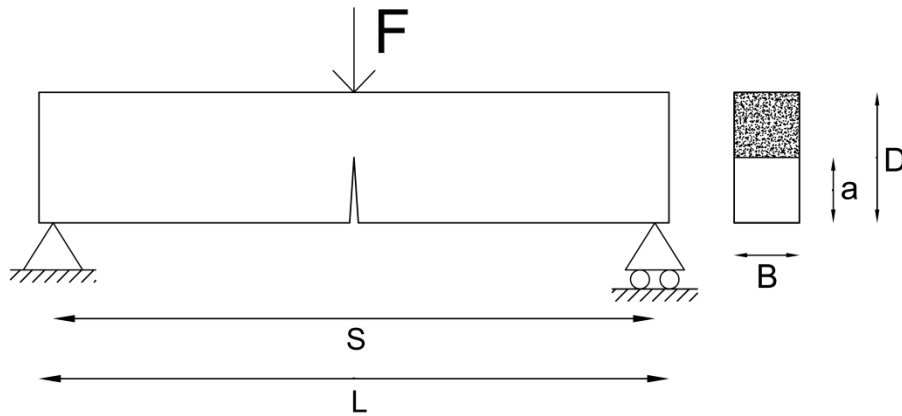


Figure 1.13: Three-point bending test geometry

Moreover the failure can be reached due to plastic collapse, in correspondence of a bending moment:

$$M_{max} = \frac{1}{4} \cdot F_{max} \cdot S = \sigma_u \cdot W_{pl}^{lig} = \sigma_u \cdot \frac{B \cdot (D - a)^2}{4} \quad (1.23)$$

corresponding to a load  $F_{max}$  that, in dimensionless form, can be expressed as a function of the relative depth of the fracture  $a/D$ :

$$\frac{F_{max} \cdot S}{\sigma_u \cdot B \cdot D^2} = \left(1 - \frac{a}{D}\right)^2 \quad (1.24)$$

Likewise, the load  $F_{max}$  corresponding to the failure for brittle fracture (Eq. (1.21)) can be rewritten in dimensionless form:

$$\frac{F_{max} \cdot S}{\sigma_u \cdot B \cdot D^2} = \frac{s}{f\left(\frac{a}{D}\right)} \quad (1.25)$$

where  $s$ , equal to:

$$s = \frac{K_{IC}}{\sigma_u \cdot D^{1/2}} \quad (1.26)$$

is called *brittleness number* (Carpinteri, 1989a); it represents the most concise way to describe the structure ductility, because it contains all the three necessary information: the material toughness, the tensile strength and the characteristic dimension of the specimen.

Eq.(1.25) shows how the dimensionless load corresponding to the unstable crack propagation can be expressed as a function of the ratio  $a/D$  and of the brittleness number  $s$ . Thus the two failure conditions (Eq.(1.24) and Eq.(1.25)) can be graphically represented as in Figure 1.14 (Carpinteri, 1989a).

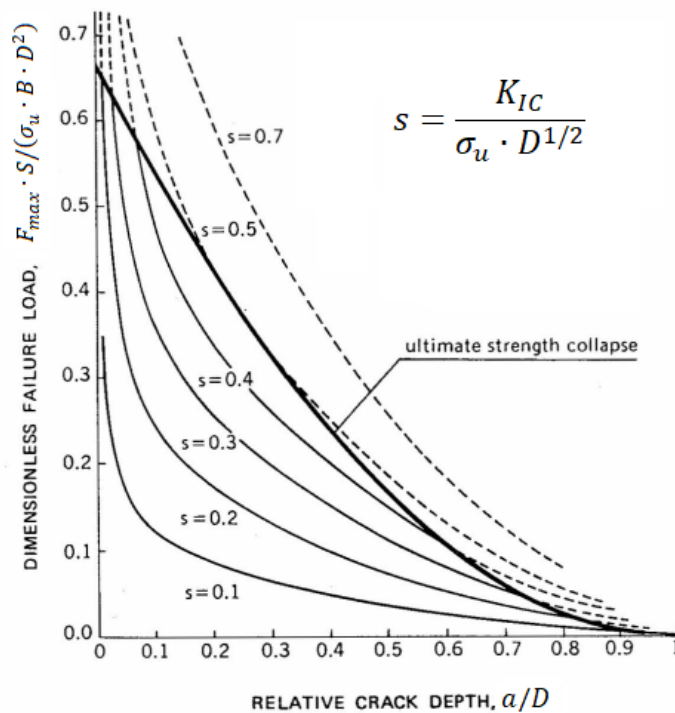


Figure 1.14: Dimensionless failure load in function of the relative crack depth for a TPB test, by varying the brittleness number

From Figure 1.14, it is evident how, for high values of the brittleness number, in particular higher than the limit value  $s_o \cong 0.75$ , the plastic collapse always precedes the unstable propagation of the fracture, while for smaller values of  $s$  this happens only for very small or very large values of the ratio  $a/D$ .

The ratio  $K_{IC}/\sigma_u$  is a measure of the material ductility. Concrete is characterized by a relative high value of this ratio: this is due to the softening behaviour (Figure 1.10).

Another parameter that can be used to describe the structure ductility is the *energy brittleness number* (Carpinteri, 1989a):

$$s_E = \frac{G_F}{\sigma_u \cdot D} \quad (1.27)$$

The correlation with the static brittleness number above mentioned (Eq.(1.26)) is:

$$s_E = \varepsilon_u \cdot s^2 \quad (1.28)$$

with  $\varepsilon_u = \sigma_u/E$ .

Two structures have the same behaviour at failure if two of the three dimensionless parameters  $s, s_E, \varepsilon_u$  are the same for both of them.

Continuing to consider a TPB test, Figure 1.15 (Carpinteri, Colombo, 1989) shows the effect of a difference in material toughness on  $F - \delta$  curves, obtained with a numerical simulation considering different values of the relative crack depth.

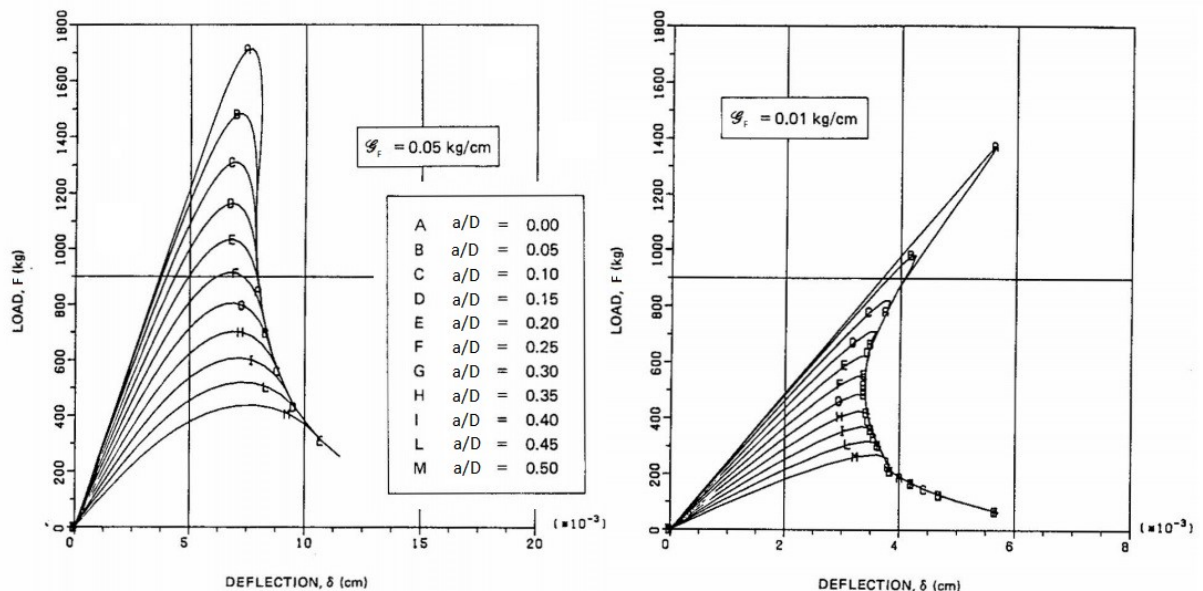


Figure 1.15: Influence of material toughness on  $F - \delta$  curves for different values of the relative crack depth

Whether the material is kept constant, scale effects can be observed in Figure 1.16 (Carpinteri, 1989d) on  $F - \delta$  curves, obtained with a numerical simulation, considering different values of the relative crack depth.

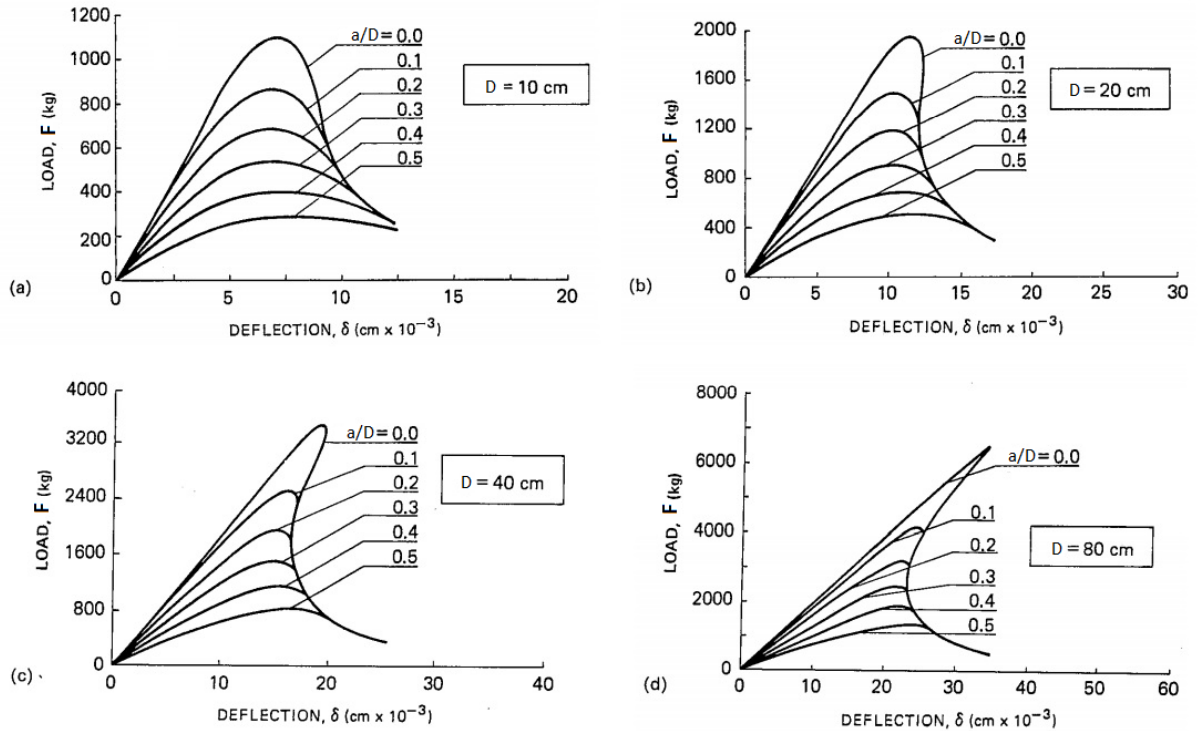


Figure 1.16: Influence of beam depth on  $F - \delta$  curves for different values of the relative crack depth

Therefore a brittle behaviour can be observed with a decrease of material toughness or with an increase of the characteristic dimension of the solid. These two aspects, together with the tensile strength, can be summarized in a single parameter, that is the brittleness number. Figure 1.17 (Carpinteri, 1989a) shows how, in a TPB test, the behaviour changes in function of  $s_E$  values, for a fixed  $a/D$  ratio.

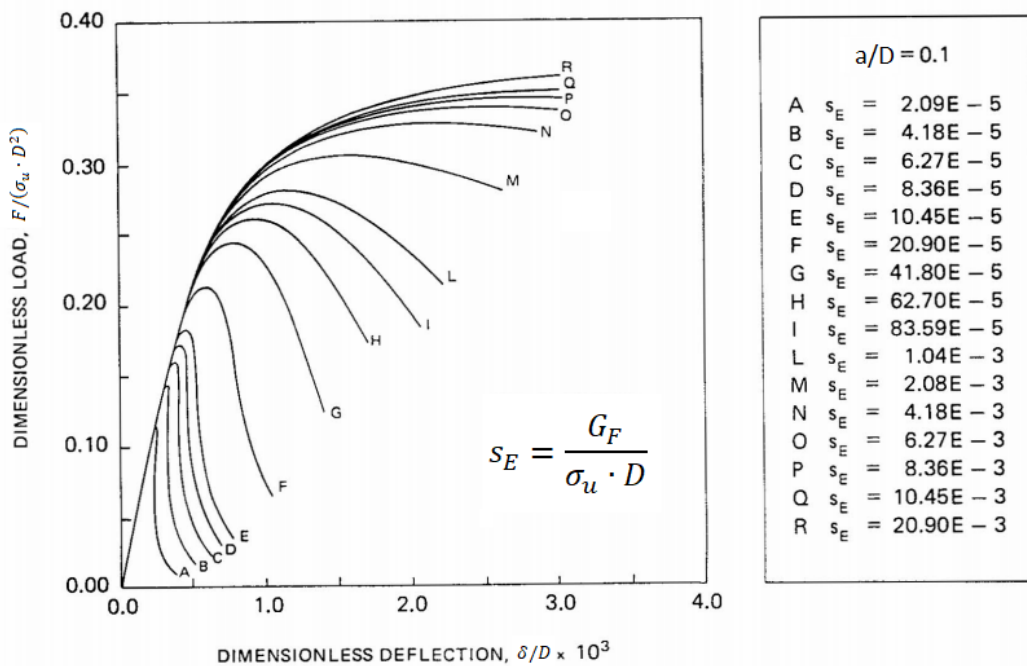


Figure 1.17: Dimensionless load-deflection diagrams by varying the energy brittleness number for a fixed value of relative crack depth

In particular, high values of  $s_E$  correspond to ductile behaviours; on the other hand, with low values of  $s_E$  a brittle behaviour is observed, characterized in the extreme cases by a snap-back instability.

At limit, for  $s_E \rightarrow 0$  it can be demonstrated how the cohesive crack model gives the same results obtainable through LEFM (Carpinteri, 1989a). Furthermore it is evident how the cohesive crack model is able to describe the brittle-ductile transition so far discussed.

For a three-point bending test, for example, two limit situations can be considered (Carpinteri, 1989b):

- $a = 0$  : absence of initial fracture; using the elastic theory, the mid-span deflection may be evaluated by:

$$\delta = \frac{1}{48} \cdot \frac{F \cdot S^3}{E \cdot I} = \frac{1}{48} \cdot \frac{F \cdot S^3}{E} \cdot \frac{12}{B \cdot D^3} = \frac{1}{4} \cdot \frac{F \cdot \lambda^3}{E \cdot B} \quad (1.29)$$

where  $\lambda = S/D$  represents the slenderness. In dimensionless form:

$$\tilde{\delta} = \frac{\delta \cdot S}{\varepsilon_u \cdot D^2} = \frac{1}{4} \cdot \frac{F \cdot \lambda^3}{E \cdot B} \cdot \frac{S}{\varepsilon_u \cdot D^2} = \frac{1}{4} \cdot \frac{F \cdot S \cdot \lambda^3}{\sigma_u \cdot B \cdot D^2} = \frac{1}{4} \cdot \tilde{P} \cdot \lambda^3 \quad (1.30)$$

where  $\tilde{P}$  is the dimensionless load:

$$\tilde{P} = \frac{F \cdot S}{\sigma_u \cdot B \cdot D^2} \quad (1.31)$$

By imposing the condition:

$$\sigma = \frac{M}{W_{el}} = \frac{F \cdot S/4}{B \cdot D^2/6} = \frac{3}{2} \cdot \frac{F \cdot S}{B \cdot D^2} < \sigma_u \quad (1.32)$$

it follows that:

$$\tilde{P} < \frac{2}{3} \quad (1.33)$$

Using Eq. (1.30) and the condition on  $\tilde{P}$  (Eq.(1.33)), the following condition is obtained:

$$\tilde{\delta} < \frac{1}{6} \cdot \lambda^3 = \delta_1 \quad (1.34)$$

- $a = D$  : limit situation before the final failure; two rigid parts are connected by an hinge in the upper beam edge, while cohesive stresses are acting, approximately with a linear distribution, on the fracture surfaces up to the point in which the widening is equal to  $w_c$ . The portion of the ligament in which these stresses are still present is identified by the coordinate  $x$  (Figure 1.18).

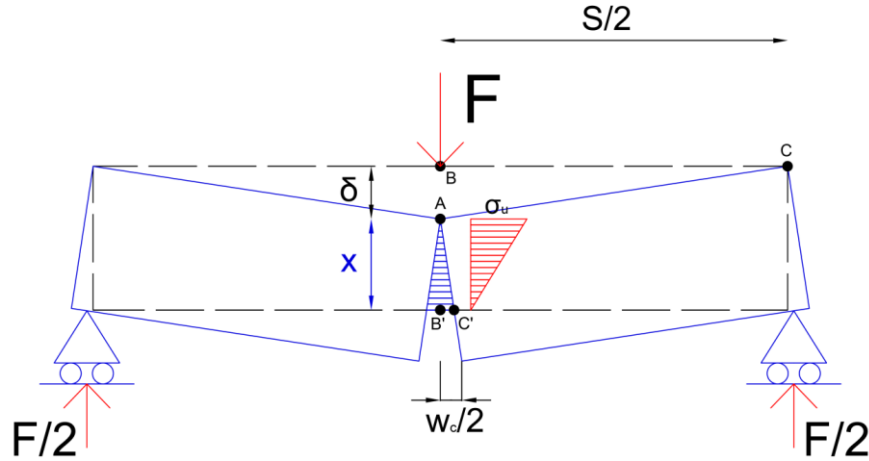


Figure 1.18: Limit situation before the final failure with cohesive forces

The geometrical similitude of the triangles ABC and AB'C' in Figure 1.18 allows to write:

$$\frac{\delta}{S/2} = \frac{w_c/2}{x} \quad (1.35)$$

The rotational equilibrium around the hinge in point A provides:

$$\frac{F}{2} \cdot \frac{S}{2} = \frac{\sigma_u \cdot x \cdot B}{2} \cdot \frac{x}{3} \quad (1.36)$$

Using Eq.(1.36), Eq.(1.31), Eq.(1.35), it is possible to write:

$$\tilde{P} = \frac{2}{3} \cdot \left(\frac{x}{D}\right)^2 = \frac{2}{3} \cdot \left(\frac{w_c \cdot S}{4 \cdot \delta \cdot D}\right)^2 = \frac{2}{3} \cdot \left(\frac{w_c \cdot S^2}{4 \cdot \varepsilon_u \cdot D^3 \cdot \tilde{\delta}}\right)^2 \quad (1.37)$$

Considering for sake of simplicity a linear cohesive law, and taking into account Eq.(1.27), Eq.(1.37) can be rewritten as:

$$\tilde{P} = \frac{2}{3} \cdot \left(\frac{2 \cdot s_E \cdot D \cdot S^2}{4 \cdot \varepsilon_u \cdot D^3 \cdot \tilde{\delta}}\right)^2 = \frac{1}{6} \cdot \left(\frac{s_E \cdot \lambda^2}{\varepsilon_u \cdot \tilde{\delta}}\right)^2 \quad (1.38)$$

By imposing the condition  $x \leq D$  and using Eq.(1.37), it follows that :

$$\tilde{P} = \frac{2}{3} \cdot \left(\frac{x}{D}\right)^2 \leq \frac{2}{3} \quad (1.39)$$

Eq.(1.38) and Eq.(1.39) imply another condition concerning  $\tilde{\delta}$  :

$$\tilde{\delta} \geq \frac{s_E \cdot \lambda^2}{\varepsilon_u \cdot 2} = \delta_2 \quad (1.40)$$

Two conditions on  $\tilde{\delta}$  have been found (Eq.(1.34), Eq.(1.40)). When the two domains are separated, the two  $\tilde{P} - \tilde{\delta}$  branches (linear and hyperbolic) are

presumably connected by a regular curve (Figure 1.19a), while if the two domains are partially overlapped (Figure 1.19b) the two branches are presumably connected by a curve with a negative (softening) or even positive slope (snap-back) (Carpinteri, 1989b).

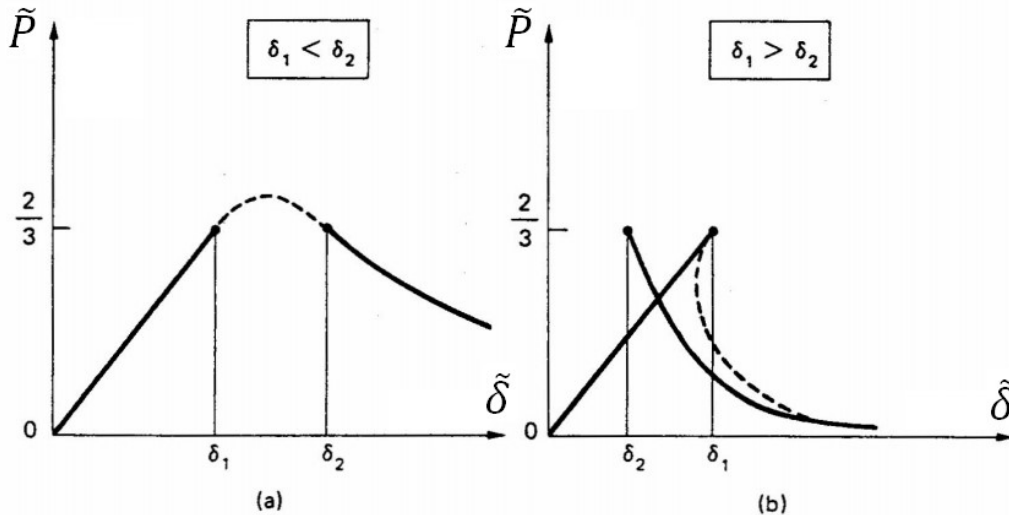


Figure 1.19: Dimensionless load-deflection curves: (a) ductile behaviour, (b) brittle behaviour

Thus, looking also at Figure 1.19, it is clear that, for a three-point bending geometry, an unstable behaviour with a possible snap-back phenomenon may occur when:

$$\delta_1 \geq \delta_2 \quad (1.41)$$

Substituting the values expressed in Eq.(1.34) and in Eq.(1.40), the brittleness condition for a three-point bending geometry (Eq.(1.41)) becomes:

$$\frac{s_E}{\varepsilon_u \cdot \lambda} = \tilde{B} \leq \frac{1}{3} \quad (1.42)$$

Carpinteri (1989e) found a similar brittleness condition also for the uniaxial tension geometry; in that case:

$$\frac{s_E}{\varepsilon_u \cdot \lambda} = \tilde{B} \leq \frac{1}{2} \quad (1.43)$$

Therefore, it is clear that the brittleness of a structure depends also on the loading conditions and on the external constraints: uniaxial tension, e.g., is more brittle than three point bending.

#### 1.1.1.4 Experimental determination of fracture energy of concrete according to RILEM Recommendation

RILEM TC 50-Fracture Mechanics of Concrete (1985) recommends a method to determine experimentally the fracture energy of plain concrete and mortar. This material property, that gives a measure of the material toughness, is defined as the absorbed energy per unit area of the fracture plane (the fracture area is the projected

area on a plane parallel to the crack direction). The method consists in three-point bending tests on notched beams, performed until the complete fracture of the specimen. The test must be stable, without sudden jumps in deformations or stresses: for this reason, the testing machine has to be stiff enough or furnished with a closed-loop servo control. Whether there are problems of stability, the test should be performed by controlling the crack mouth opening displacement. The size of the beam depends on the maximum size  $D_{max}$  of the aggregate, according to Table 1 (the symbols are referred to Figure 1.13).

$D_{max}$ [mm]	$D$ [mm]	$B$ [mm]	$L$ [mm]	$S$ [mm]
1 – 16	$100 \pm 5$	$100 \pm 5$	$840 \pm 10$	$800 \pm 5$
16 – 32	$200 \pm 5$	$100 \pm 5$	$1190 \pm 10$	$1130 \pm 5$
32 – 48	$300 \pm 5$	$150 \pm 5$	$1450 \pm 10$	$1385 \pm 5$
48 – 64	$400 \pm 5$	$200 \pm 5$	$1640 \pm 10$	$1600 \pm 5$

Table 1: Sizes of specimens recommended by RILEM TC 50-FMC

The beam with a depth of 100 mm is considered the standard test beam, also because it is easy to handle. Nevertheless, if the maximum aggregate size is bigger than 16 mm, other beam sizes are recommended. In order to limit the stress due to the weight of these bigger specimens, it is better to increase the width, the depth and the notch depth with the same factor  $k$ , while the span only with a factor  $\sqrt{k}$ . The presence of the notch, with a depth equal to half the beam depth  $\pm 5$  mm, ensures that the fracture takes place in a well-defined plane, so that the energy absorption in other process, different from tensile fracture, is negligible (Hillerborg, 1983). The compressive strength of the material must be at least five times the tensile one, in order to avoid energy absorption in the compressed zone of the ligament. The result of the tests, performed with a constant rate of deformation, is the curve representing the load as a function of the vertical displacement of the mid-span section (Figure 1.20). The area  $W_0$  under this diagram gives the energy supplied by the machine.

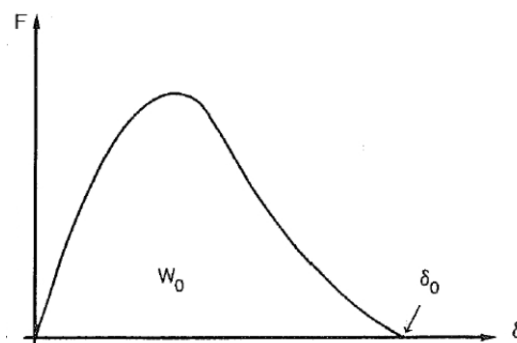


Figure 1.20: Typical load-deflection curve obtainable with a TPB test on a concrete specimen

However the load imposed by the testing machine acts together with the beam weight and with the weight of the loading device which is not attached to the machine. These additional forces also supply energy when the beam deflects. Hence, in order to obtain the total absorbed energy, it is necessary to correct the  $F - \delta$  curve experimentally obtained as shown in Figure 1.21.

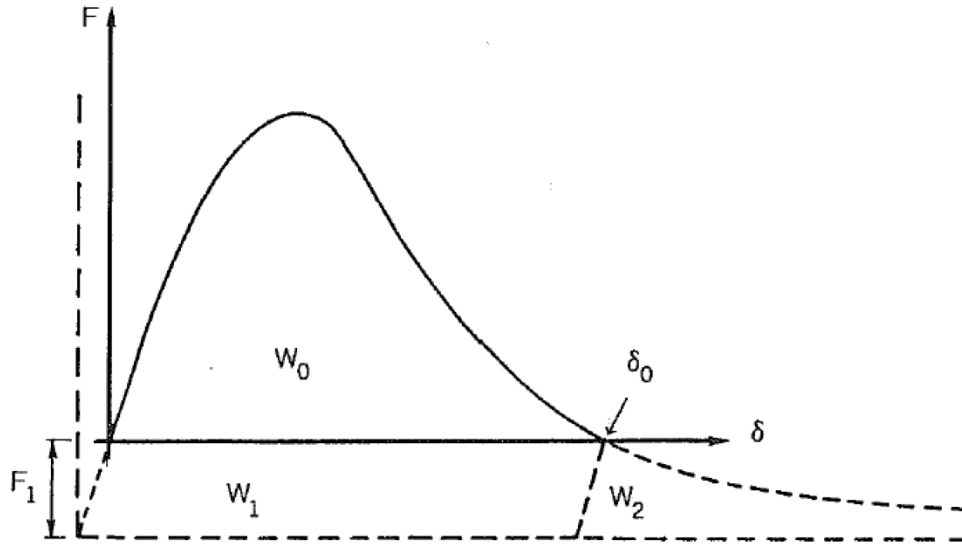


Figure 1.21: Load-deflection curve modified in order to consider also the beam weight and the weight of the loading arrangement

In Figure 1.21, the recorded curve is represented with a continuous line, while the dashed lines represent the remaining part necessary to obtain the complete curve. In particular, the horizontal axis is translated downward of a quantity  $F_1$ , which represents the concentrated load, applied in the center of the beam, that would produce in the mid-span section the same bending moment due to self-weight and weight of loading arrangement. Thus the total absorbed energy is:

$$W = W_0 + W_1 + W_2 \quad (1.44)$$

The areas  $W_1$  and  $W_2$  are very similar, and they can be considered equal to  $F_1 \cdot \delta_0$  ( $\delta_0$  is the deformation reached at the end of the test, when the load is zero and the beam is completely broken).

Finally the fracture energy is evaluated as:

$$G_F = \frac{(W_0 + m \cdot g \cdot \delta_0)}{A_{lig}} \quad (1.45)$$

in which  $m = m_1 + 2 \cdot m_2$ , where  $m_1$  is the weight of the beam between the supports, calculated as the beam weight multiplied by  $S/L$ , while  $m_2$  is the weight of the part of the loading arrangement which is not attached to the machine, but follows the beam until failure;  $g$  is the acceleration of gravity ( $9,81 \text{ m/s}^2$ ), whereas  $A_{lig}$  is the ligament area, obtained with an ideal projection of the fracture area on a plane perpendicular to the beam axis.

Although the fracture energy is considered a material property in the cohesive crack model, Hillerborg (1983,1984) highlighted the influence of the beam depth on the fracture energy values through the results of several tests performed in different laboratories in all the world. In particular he noticed that an increase in the beam depth with a factor 4 gives an increase in  $G_F$  of about the 20%.

Along with the fracture energy, it is possible to determine, using the results of these tests, other two material properties (Hillerborg, 1984):

- from the initial slope of the load-deformation diagram, an approximate value of the modulus of elasticity might be obtained;
- the bending strength corresponding to the maximum load  $F_{max}$  reached in the test:

$$\sigma_u = \frac{M_{tot}}{W_{el}^{lig}} = \frac{\left(F_{max} + \frac{m \cdot g}{2}\right) \cdot \frac{S}{4}}{\frac{B \cdot (D - a)^2}{6}} \quad (1.46)$$

in which  $m \cdot g/2$  is the concentrated load that should be applied in the center of the beam in order to obtain the same bending moment in the mid-span section due to the distributed load representing the weight of the specimen.

The aim of this work will be the experimental determination and the description of the scale effects on fracture energy and bending strength, evaluated by means of the  $G_F - test$  on plain concrete specimens with the different sizes recommended by RILEM TC 50-FMC (Table 1).

### 1.1.2 Review of scale effect models

In the classical failure theories, the tensile strength is a material constant, independent of the structural size and geometry. It is one of the three parameters which characterize the cohesive law used in the fictitious crack model described in section [1.1.1.2]. This model postulates that the tensile strength, the fracture energy, the critical opening displacement and the shape of the softening curve are constant properties for a given type of concrete. Actually these parameters, fundamental to describing the fracture behaviour of concrete, are found to be significantly scale-dependent. In fact, numerous experiments have shown that, when geometrically similar concrete specimens are tested, an increase of specimen size leads to decreasing of strength and increasing of fracture energy and toughness.

Consequently the concept of quasi-brittleness becomes relative. Quasi-brittle materials, such as concrete, are materials incapable of purely plastic deformations but characterized by a fracture process zone with a not negligible dimension if compared to the structural size. However, on a large enough scale they become perfectly brittle, while on a small enough scale they behave as elastic bodies with a perfect plastic crack, following the theory of plasticity. Vice versa, brittle materials,

which are usually characterized by a crack growth governed by LEFM, become quasi-brittle on a small enough scale.

Theoretically, for the direct measurement of size-independent fracture properties of concrete-like materials, very large specimens should be tested, but this is well beyond the capacity of a common laboratory. Because there is a great gap between the scales of laboratory tests and of large structures such as dams, bridges, etc., size effect models are necessary for the assessment of fracture parameters based on the results of tests performed on normal laboratory-size specimens.

For these reasons, the phenomenon has been studied by many researchers, and different theories have been proposed to explain the sources of scale effects and to provide models in order to express fracture energy and strength in function of a characteristic dimension of the structure. The controversial history of these models is briefly outlined in the next paragraph [1.1.2.1]. According to the final report of RILEM TC QFS (Bazant et al., 2004), three basic theories of scaling can be identified:

- the Weibull statistical theory (Weibull, 1939);
- the theory of stress redistributions and stored energy release caused by large stable growth of cracking zones or fractures (Bazant, 1984);
- the theory of crack fractality (Carpinteri, 1994a, 1994b).

However, another model, based on the concept of local fracture energy (Hu, Wittmann, 1992), will be discussed: the boundary effect model (Duan, Hu, Wittmann, 2002).

Finally, in section [1.1.2.2], the attention will be focused on the fractal model and the renormalization procedure, that will be used in the second part of the present thesis to interpret the experimental results.

#### *1.1.2.1 Historical development of the principal scale effect models*

The effect of structure size on material strength is an old problem. Already in the 1500s, Leonardo da Vinci observed that: “Among cords of equal thickness the longest is the least strong”; furthermore he wrote that a cord “is so much stronger [...] as it is shorter”. Practically he supposed an inverse proportionality of tensile strength to the length of the chord. This exaggerated hypothesis on size effect was disallowed, about a hundred years later, by Galileo Galilei . He stated that if a long chord is cut in different points, the remaining parts are not stronger; nevertheless he also discussed scale effects, referring to the different shape of animal bones in large and small animals: the greatness of bones is the weakness of big animals.

The problem was treated with carefulness and extensive experiments by Mariotte (1686). Introducing the concept of the “inequality of matter”, he proposed for the first time the basic idea of the statistical size effect: in a structure, the material contains weaker points with a resistance lower than the nominal one; obviously, the probability of encountering these defects increases with the structural size.

After Mariotte's work, scale effects were studied again by Griffith (1921). He experimentally observed how the resistance of glass fibers substantially increases when their diameter is reduced. He explained this phenomenon by saying that: "[...] the weakness of isotropic solids [...] is due to the presence of discontinuities or flaws [...]. The effective strength of technical materials could be increased 10 or 20 times at least if these flaws could be eliminated". With reference to Eq. (1.7), this statement can be clarify considering, e.g., high strength concretes: with a reduction of the porosity and consequently of the half-length of equivalent micro defect pre-existing in the material ( $a_0$ ), an important increase of the strength  $\sigma_p$  can be obtained. Thus, Griffith gave a physical explanation to Mariotte's statistical idea.

Until about 1980, size effects were considered as a purely statistical problem. The basic framework of statistical size effect theory was completed by Weibull (1939). He proposed a new probability distribution (that will take his name) to describe the extremely small values of material strength. It consists in a power law with a threshold. Afterwards, this distribution will be justified theoretically, using a probabilistic model for the placement of microscopic defects in the material. A basic concept for the statistical approach is the weakest link model, introduced by Peirce (1926) for discrete systems such as chains, and then extended to continuous systems. In the discrete model, the survival probability of a chain, subjected to two tensile forces at its extremities, is calculated as the joint probability of survival of all the  $N$  elements that form the chain; at the end, the failure probability  $P_f$  of the whole chain can be obtained using the following power law:

$$P_f = 1 - e^{-N \cdot P(\sigma)} \quad (1.47)$$

where  $P(\sigma)$  is the probability of failure of one element for the given stress level  $\sigma$ . In the continuous model for structures subjected to uniaxial stress, Eq.(1.47) can be used substituting  $N$  with the ratio  $V/V_R$ , in which  $V$  represents the volume of the continuous body, while  $V_R$  is a representative volume of the material. Therefore, in this case the probability of failure  $P(\sigma)$  is referred to reference volume  $V_R$ . Because  $V_R$  and consequently  $P(\sigma)$  are difficult to determine, Eq.(1.47) is substituted by:

$$P_f(\sigma, V) = 1 - e^{-c(\sigma) \cdot V} \quad (1.48)$$

$c(\sigma)$  is called concentration function; Weibull proposed his statistical probability distribution to express this function:

$$c(\sigma) = \frac{1}{V_0} \cdot \left\langle \frac{\sigma - \sigma_u}{s_0} \right\rangle^m \quad (1.49)$$

The three parameters that appears in Weibull distribution are:

- the shape parameter  $m$ : experimental evidences show that  $m = 12$  is a good value for concrete;
- the scale parameter  $s_0$ ;

- the strength threshold  $\sigma_u$ : it is usually assumed equal to zero, because its determination is very difficult.

$V_0$  is a reference volume, that can be considered equal to the volume of specimens used to experimentally determine Weibull's parameters.

In general, for structures subjected to non-uniform multidimensional stress, Weibull statistical size effect on the mean strength can be expressed how:

$$\sigma_N \propto D^{-n_d/m} \quad (1.50)$$

where  $n_d = 1, 2, 3$  respectively for uni-, two- and three-dimensional similarity of specimen;  $D$  is the characteristic size.

However, this scaling law can be applied only on structures with a brittle behaviour, i.e. structures that fail as soon as macroscopic cracking occurs, without the development of important plastic zones. For quasi-brittle materials, instead, this theory presents several limitations (Bazant et al., 2004):

- a) the presence of a power law implies the absence of any characteristic length; obviously it is not the case of materials, such as concrete, that contains important heterogeneities and that exhibit a large fracture process zone before the final collapse: remembering the expression provided by Irwin (Eq.(1.16)) for the extension of this region at the onset of crack propagation, the following definition of the characteristic length (or material length) can be adopted:

$$l_0 = \frac{E \cdot G_F}{\sigma_P^2} \quad (1.51)$$

- b) quasi-brittle materials, e.g., concrete, collapse only after a large stable macroscopic crack growth and the development of an important fracture process zone before reaching the maximum load; consequently, the stress distribution in correspondence of the final failure is very different from the elastic stress distribution considered in statistical size effect theory, because important stress redistributions occur;
- c) the classical Weibull theory considers every structure as an equivalent uniaxially stressed bar, thus it cannot describe the stress field realistically;
- d) the model gives very large differences, in terms of size effects, between two- and three-dimensional geometric similarities, that are not realistic;
- e) size effects obtained with Weibull model are smaller than size effects experimentally observed on quasi-brittle specimens;
- f) the classical Weibull theory, based on the weakest link model, does not consider the spatial correlation of material failure probabilities at various points.

Hence, the statistical size effect theory appears inapplicable for concrete, unless large enough structures are considered, characterized by a brittle behaviour.

Since the 1970s, the idea of deterministic size effect, due to the stress redistribution before the failure in quasi-brittle materials, began to be considered. In that period it was understood that LEFM cannot be used for materials like concrete that exhibit a large fracture process zone before the unstable crack propagation. Leicester (1969) performed several tests on similar notched beams of different sizes; he tried to apply a power law to fit the results in terms of nominal strength:

$$\sigma_N \propto D^{-n} \quad (1.52)$$

He experimentally observed that the optimum value of the size coefficient  $n$  was less than  $1/2$ , that is the value expected from LEFM. However Eq.(1.52) was not yet the right solution, also because it is a power law and so denies the presence of a characteristic length in concrete. Other three-point bend tests were performed by Walsh (1972). He also considered notched geometrically similar plain concrete specimens of different sizes, and observed, on a doubly logarithmic diagram with nominal strength versus size, that the scaling law should represent the transition between two extreme cases: plasticity and LEFM. The plastic limit analysis should be applied to small enough scales, that exhibit a ductile behaviour; according to this theory, the strength is independent from the structure size. On the other hand, for large enough scales a brittle behaviour can be considered, and LEFM can be applied; according to this theory, the nominal strength declines in proportion to  $D^{-1/2}$ . Another important contribution was represented by Hillerborg's fictitious crack model (Hillerborg, Mod er and Petersson, 1976), in which the deterministic nature of size effects was further emphasized.

The combination between the two above mentioned extreme cases (plasticity and Linear Elastic Fracture Mechanics) become the key to study the deterministic size effect of quasi-brittle materials. For small enough scales, a strength criteria can be used, and consequently there are no scale effects (horizontal straight line in Figure 1.22); on the contrary, for large enough scales, characterized by a perfectly brittle behaviour, LEFM can be applied (inclined straight line in Figure 1.22 of slope  $-1/2$ ). Although these two theories considered separately do not contemplate any characteristic length (they are power laws), their combination does: this material length is in fact represented by the intersection between these two power laws, and it is denoted as  $D_0$ . The first very famous attempt to bridge these two extreme behaviours for the intermediate scales was proposed by Bazant (1984), with the so called Size Effect Law (SEL):

$$\sigma_N = \frac{B \cdot \sigma_0}{\sqrt{1 + \frac{D}{D_0}}} \quad (1.53)$$

in which:

- $B$  is a dimensionless constant;
- $D_0$  is the material length, representing the transitional size;

- $\sigma_0$  is a material constant, representing the tensile strength for small enough scales.

Both  $B$  and  $D_0$  depend on fracture properties of the material and on the geometry of the structure, but they are independent from the structural size. These two parameters are usually experimentally determined. The function represented by Eq.(1.53) has two asymptotes:

- for  $D \ll D_0$  size effect tends to disappear:  $\sigma_N \rightarrow B \cdot \sigma_0 = \text{constant}$  (strength criteria represented by horizontal asymptote in Figure 1.22);
- for  $D \gg D_0$  the function tends to the power law expected from LEFM (inclined asymptote in Figure 1.22):

$$\sigma_N \rightarrow B \cdot \sigma_0 \cdot \left(\frac{D}{D_0}\right)^{-\frac{1}{2}} \quad \Rightarrow \quad \text{Log } \sigma_N = -\frac{1}{2} \cdot \text{Log } D + \text{constant}$$

Thus, Size Effect Law can be represented as in Figure 1.22:

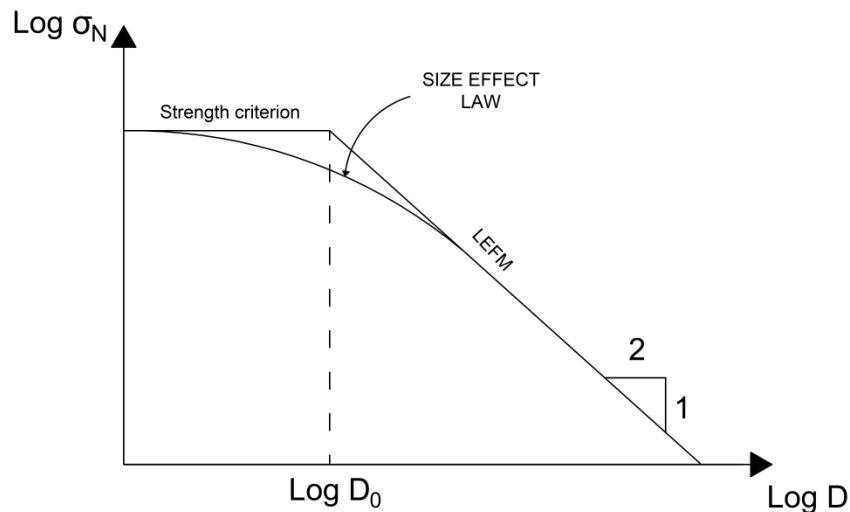


Figure 1.22: Size Effect Law (Bazant, 1984)

If  $D < D_0$  structure behaviour is closer to plasticity and so it is predominantly ductile, whereas if  $D > D_0$  the structure presents a predominantly brittle behaviour, closer to Linear Elastic Fracture Mechanics. For this reason, the dimensionless number:

$$\beta = \frac{D}{D_0} \quad (1.54)$$

can be considered as a brittleness number (Bazant, 1984), independent of structure shape. “For  $\beta \rightarrow \infty$  the structure is perfectly brittle (i.e. follows LEFM), in which case the size effect is the strongest possible, while for  $\beta \rightarrow 0$  the structure is non-brittle (or ductile, plastic), in which case there is no size effect. Regardless of geometry, quasibrittle structures are those for which  $0.1 \leq \beta \leq 10$ , in which case the size effect represents a smooth transition (or interpolation) that bridges the power law size effects for the two asymptotic cases” (Bazant et al., 2004). Bazant’s size effect law

(Eq.(1.53)) can be derived easily writing an energy balance condition (Bazant, 1984) that involves the energy available (function of  $\sigma_N$ ) and the energy required for crack propagation (function of the fracture energy,  $G_F$ , considered in this case as a material property). The hypothesis used by Bazant in this demonstration imply important limitations of his size effect law: it can be considered valid only within a limited size range. Furthermore, Bazant supposed that, in correspondence of the maximum load, there is always a crack with a length proportional to specimen size. In this way, he could propose similar considerations to those already reported in section [1.1.1.1]: considering the half-length  $a_0$  of equivalent micro defect pre-existing in the material (Eq.(1.7)), according to this hypothesis, small structures with  $a < a_0$  will fail for plastic collapse, while large structures with  $a > a_0$  will fail for unstable crack propagation. Nevertheless, such a hypothesis could be considered true only if pre-existing cracks are present; otherwise, what really happens is exactly the opposite. In section [1.1.1.3], Figure 1.16 shows the numerical results obtained by the application of the cohesive crack model; in particular, considering a large size specimen without a pre-existing notch ( $a/D = 0$ ), a very brittle behaviour was observed (snap-back instability), since the failure, in correspondence of the maximum load, occurs without a previous development of macro cracks. Actually, in fact, in unnotched specimens the size  $a$  of the characteristic flaw is independent of the specimen size. Consequently, SEL can be used only with pre-notched specimens, under the condition that the notch depth must be proportional to the structure size.

A completely different approach is represented by the fractal explanation of size effects proposed by Carpinteri (1994a). In this theory, the quasi-brittle and disordered materials such as concrete are considered as fractal object with a self-similarity microstructure, in order to define scale-invariant material constants, with non-integer physical dimensions depending on the fractal nature of the damaged material microstructure. In fact, if strength and toughness of disordered materials are measured with reference to the classical Euclidean geometrical entities (areas and volumes with integer dimensions of 2 and 3, respectively), it is impossible to obtain constant material properties. It is necessary to consider the actual dimension of material ligament at peak stress and the actual dimension of fracture surface at failure in order to define the “universal” scale-independent values of these two parameters. This procedure, from a mathematical point of view, may be framed in the so-called Renormalization Group Theory. In particular, the energy dissipation during the crack propagation is supposed to occur in an invasive fractal domain, with an intermediate dimension between 2 (surface) and 3 (volume); on the other hand, tensile strength is defined on a lacunar fractal domain, with a dimension lower than 2. The fractal domains present in nature are characterized by a random self-similarity: it means that their aspect seems to be statistically the same under the different scales of observation. However, fractality tends to vanish with the increase of the observation scale: there is an order-disorder transition (Mandelbrot, 1982) from a fractal disordered regime at the microscopic scales up to an homogeneous Euclidean regime at the largest scales, in which the heterogeneity of the material can be

neglected. In other words, the effect of microstructural disorder decreases in large structures (large relatively to the microstructural characteristic size of the material). At limit, when the structural size tends to infinit, scale effects should be null, and thus it is possible to determine the true material properties. Carpinteri, Chiaia, Ferro (1995) supposed a continuous topological transition between these two asymptotic regimes (fractal and homogeneous): in order to describe the entire range of the scaling, not only one, but infinite fractal exponents are necessary. For this reason, this kind of scaling laws are called Multifractal Scaling Laws (MFSL). Actually, the transition from a disordered to an ordered regime can be observed only if scale variations over several orders of magnitude are considered. In laboratory tests, however, only narrow size range can be investigated (it usually does not exceed one order of magnitude): therefore it is better in these cases to use a monofractal scaling law (see Section [1.1.2.2]), characterized by a single fractal exponent, obtained considering the tangent to the MFSL in correspondence of the scale range of interest. In other words, the monofractal law can be seen as an approximation of the multifractal law in a limited scale range. Thus, mono-fractality will be considered in the second part of the present work, where the results concerning three-point bending tests on different size specimens in a scale range of 1:4 will be analysed. Two Multifractal Scaling Laws have been proposed by Carpinteri, Chiaia, Ferro (1995) for fracture energy and tensile strength of quasi-brittle and disordered materials. They are represented in Figure 1.23 with linear diagrams, and in Figure 1.24 with bilogarithmic diagrams;  $b$  represents the characteristic dimension of the specimen.

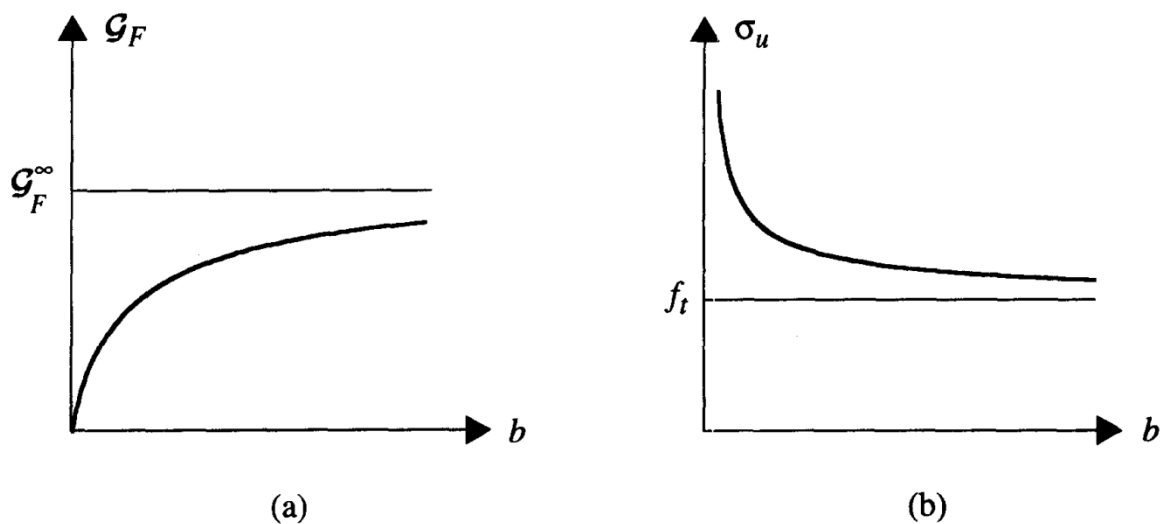


Figure 1.23: Multifractal Scaling Laws for (a) fracture energy and (b) tensile strength in linear diagrams

The laws represented in Figure 1.23 have analytical expressions in the form:

$$G_F = \left( A + \frac{B}{b} \right)^{-1/2} \quad (1.55)$$

$$\sigma_u = \left( A + \frac{B}{b} \right)^{1/2} \quad (1.56)$$

In the bilogarithmic form, Eq.(1.55) and Eq.(1.56) become respectively:

$$\text{Log } G_F = -\frac{1}{2} \cdot \text{Log} \left( A + \frac{B}{10^{\text{Log } b}} \right) \quad (1.57)$$

$$\text{Log } \sigma_u = \frac{1}{2} \cdot \text{Log} \left( A + \frac{B}{10^{\text{Log } b}} \right) \quad (1.58)$$

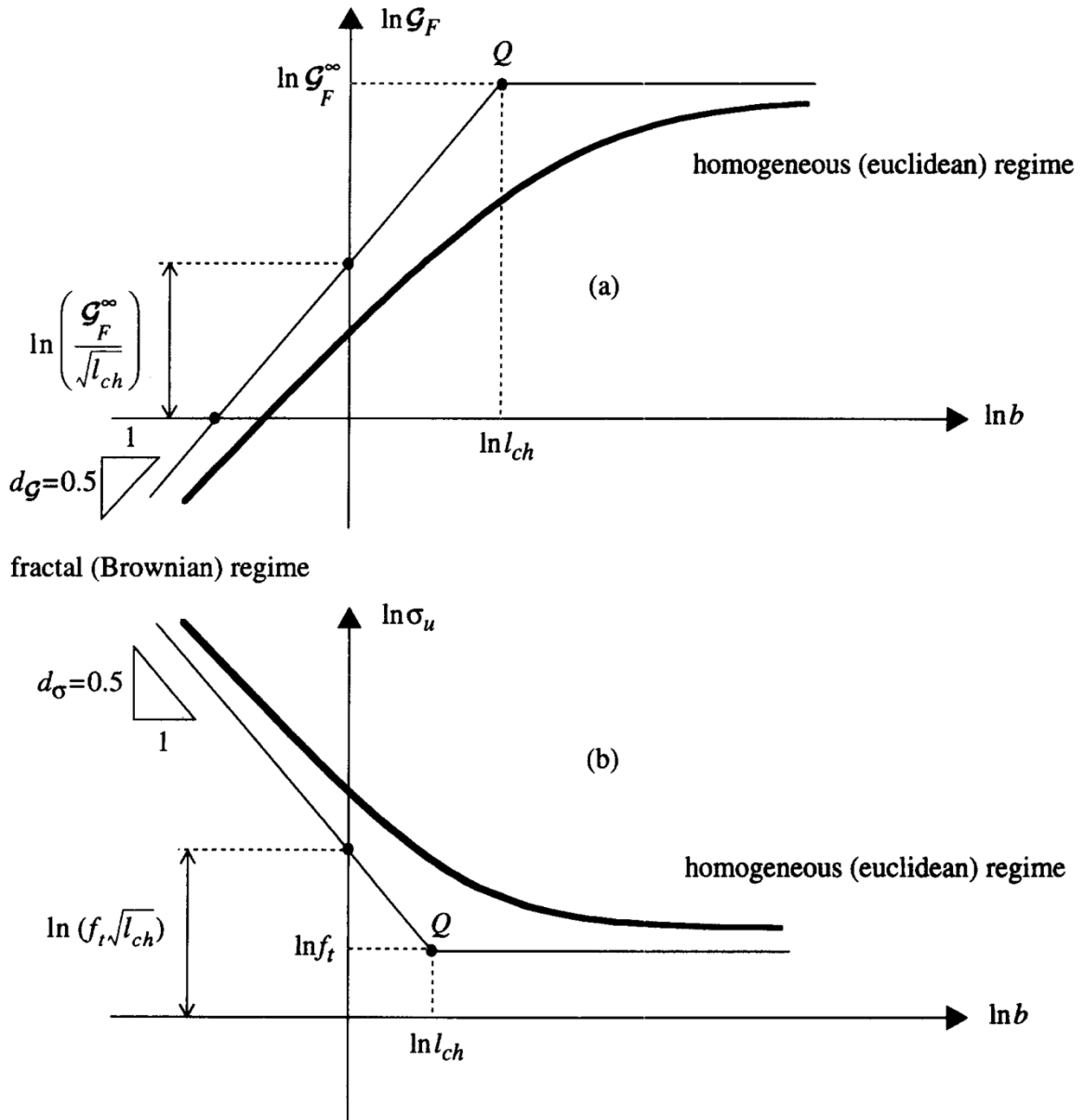


Figure 1.24: Multifractal Scaling Laws for (a) fracture energy and (b) tensile strength in bilogarithmic diagrams

Considering the MFSL for tensile strength (Eq.(1.56)):

- $\lim_{b \rightarrow \infty} \sigma_u = \sqrt{A} = \sigma_u^\infty = f_t$  : it represents the real material property (horizontal asymptote in Figure 1.23b), because it is referred to very large sizes, in which the fractality has not any effect;
- $\lim_{b \rightarrow 0} \sigma_u = +\infty$  (vertical asymptote in Figure 1.23b).

The trend shown in Figure 1.23b is thus the same of that represented in Figure 1.3 with Griffith's hyperbola. In the bilogarithmic form (Eq.(1.58)), obviously, there is again the horizontal asymptote for macro scales, while for micro scales the vertical asymptote observed in Figure 1.23b becomes an inclined asymptote with a negative slope of  $1/2$ : it represents the highest possible disorder, called Brownian disorder. In Figure 1.24b point Q, representing the intersection of the two asymptotes, corresponds to the value  $\text{Log } B/A$ . From a dimensional analysis, the ratio  $B/A$  results to be a length: it represents a characteristic length  $l_{ch}$  of the material, related to its heterogeneity and to the maximum aggregate size, and it separates the fractal regime for small scales from the homogeneous asymptotic regime for large scales. Hence, Eq.(1.56) can be rewritten in the following way:

$$\sigma_u = \sqrt{A} \cdot \left(1 + \frac{B/A}{b}\right)^{\frac{1}{2}} = \sigma_u^\infty \cdot \left(1 + \frac{l_{ch}}{b}\right)^{\frac{1}{2}} \quad (1.59)$$

Similar considerations can be done for fracture energy. With respect to Eq.(1.55):

- $\lim_{b \rightarrow \infty} G_F = 1/\sqrt{A} = G_F^\infty$ : it is the real constant of the material (horizontal asymptote in Figure 1.23a), since it is referred to macro scales;
- $\lim_{b \rightarrow 0} G_F = 0$

Eq. (1.55) becomes so:

$$G_F = \frac{1}{\sqrt{A}} \cdot \left(1 + \frac{B/A}{b}\right)^{-\frac{1}{2}} = G_F^\infty \cdot \left(1 + \frac{l_{ch}}{b}\right)^{-\frac{1}{2}} \quad (1.60)$$

Representing this law in a bilogarithmic diagram (Figure 1.24a), also in this case two asymptotes are present: the horizontal one referred to the homogeneous regime, and the inclined one, for fractal regime, characterized by a positive slope of  $1/2$ . The two MFSL represented in Figure 1.24 are thus very similar; the only difference is the sign of the Brownian exponent:  $+1/2$  for the invasive domain related to fracture energy,  $-1/2$  for the lacunar domain related to tensile strength. The two parameters A and B in Eq.(1.55) and (1.56) can be determined using experimental results, through best fitting procedures.

Contrary to Bazant's Size Effect Law, the MFSL permits a good interpolation of experimental results also when large notches in the specimens are absent. Bazant manifested some skepticism about the fractal theory, especially on the slope of the MFSL asymptote at the smaller scale, and on the concavity of the law represented in Figure 1.24b (Bazant et al., 2004), since it is opposite of that characterizing his SEL (Figure 1.22). However, it was observed how the MFSL consents interpolation of

experimental results better than SEL. Besides the limitations above mentioned, a further anomaly is present in Bazant's Size Effect Law: in the limit of infinite structural size, LEFM seems to govern completely the strength behaviour; consequently, for very large structures the tensile strength should be equal to zero. This result is obviously absurd. After several corrections of SEL, Bazant introduced the so-called Universal Size Effect Law (USEL), suitable not only for notched specimens, but also to describe crack initiation. Nevertheless, in this case the same upward concavity of MFSL is obtained (Bazant, 1997).

Recently, another noteworthy scale effect theory has been proposed, based on the concept of local fracture energy (Hu, Wittman, 1992). The source of scale effects, in this case, is represented by the interaction between the crack, the Fracture Process Zone (FPZ) and the boundary of specimen. In Section [1.1.1.2] it was underlined how in concrete specimens, LEFM can be applied only if FPZ is enough small respect to specimen size, and away from the front and back surfaces. In fact, when the fracture is approaching to the back surface during its propagation, the FPZ is not small in comparison with the remaining part of the uncracked ligament, and thus LEFM fails. In other words, LEFM is suitable with large enough specimens, in which FPZ should be far away from any boundaries. On the contrary, if crack-tip FPZ is not small in comparison with its distance to boundaries, scale effects will occur. Therefore, an inner region, away from the boundaries, in which LEFM can be applied, may be distinguished from a boundary/outer region. A local fracture energy model is thus proposed; it assumed that: "[...] different fracture energy dissipations occurred at different positions along the crack path" (Duan, Hu, Wittmann, 2002). A bilinear function was proposed to describe approximately the energy distributions along the ligament of a pre-notched specimen. This law, called  $g_f(x)$ , is represented in Figure 1.25 as a function of ligament coordinate  $x$ ; the analytical expression is the following:

$$g_f(x) = \begin{cases} G_F & \text{for } x < D - a - a_l^* \\ G_F \cdot \frac{(D - a - x)}{a_l^*} & \text{for } x \geq D - a - a_l^* \end{cases} \quad (1.61)$$

in which:

- $(D - a)$  is the ligament size (see Figure 1.13 for TPB test);
- $G_F$  in this case represents the size-independent material property; it can be measured only in the inner region away from the boundaries, where LEFM applies;
- $a_l^*$  is called transition ligament length, and corresponds to the intersection of the two straight lines that approximate  $g_f$ ; it represents the passage from inner to outer region.

Summing up, in the inner region the local fracture energy is constant and equal to  $G_F$ , that is the size-independent fracture energy of the material; in the outer region,  $g_f$  is location dependent, and falls to zero in correspondence of the specimen back face.

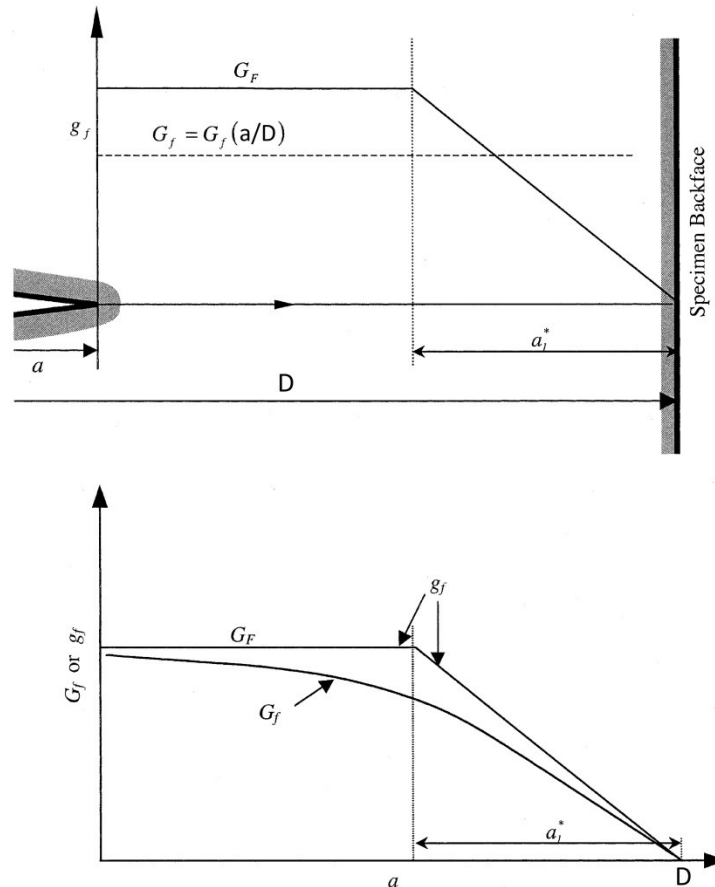


Figure 1.25: Distribution of fracture energy along the ligament (local fracture energy model)

In this model, the RILEM defined fracture energy (Eq.(1.45)) described in Section [1.1.1.4] represents an average value, that includes the energy dissipations in both the inner and the outer regions (in Figure 1.25 it is indicated with  $G_f$ ); for this reason it represents a size-dependent parameter. Only if the inner region is significantly bigger than the outer region, it becomes size/ligament independent: this happens in large enough specimens. In fact: “[...]  $G_f$  approaches to  $G_F$  asymptotically with increasing specimen size as the maximum outer/boundary region has already been established and only the inner region is being increased” (Duan, Hu, Wittmann, 2002). The usefulness of the method consists in the determination of the size-independent fracture energy  $G_F$  by means of the size-dependent  $G_f$  measurements. However, it is necessary to know the transitional ligament length, since the available equation is only one (Eq.(1.61)), but the unknowns are two ( $G_F$  and  $a_l^*$ ). A first way to solve the problem consists in performing several tests for the determination of  $G_f$  on fixed size specimens, but with different notch length: thus an over-determinate system of equations can be obtained and solved by a least square method in order to determine the best estimates of  $G_F$  and  $a_l^*$ . A second possibility was proposed by Muralidhara et al. (2010). It consists in a hybrid method, since it is based on the localization of Acoustic Emission events along the ligament length. Experimental evidences show in fact that AE activities decrease towards the specimen back

boundary. If an histogram with the number of AE events in the different portions of ligament lengths is outlined, it is possible to determine using AE technique the value of the transition ligament length  $a_l^*$ ; at that point Eq.(1.61) contains a unique unknowns, i.e. the true size-independent value of material fracture energy.

Muralidhara, Prasad, Singh (2013) proposed a further method to determine the size independent fracture energy of material. It is called fracture energy release rate. It is based on the assumption that the fracture energy is proportional to the size of the FPZ, and in turn this latter is proportional to the specimen size. However the rate of increase of FPZ size decreases with the increasing of specimen size. Consequently the rate of increase of fracture energy decreases with the increase in un-cracked ligament length. The ratio between the fracture energy and the un-cracked ligament length practically becomes a constant in correspondence of large un-cracked ligament lengths. This constant should represent the real material property  $G_F$ .

#### 1.1.2.2 Fractal model for scale effects on tensile strength and fracture energy

In the previous paragraph, the principal scaling laws for tensile strength and fracture energy have been mentioned and briefly described. Among them, the fractal theory (Carpinteri, 1994a, and Carpinteri, Chiaia, Ferro, 1995) is of course one of the most interesting and experimentally validated. Multifractal Scaling Laws have been discussed and, furthermore, the difficulties in their practical application have been underlined. In fact, considering the capacities of a common laboratory, the maximum size range that can be examined usually does not exceed one order of magnitude, and this is not enough in order to use these laws. For this reason, in this section the attention will be focused on the so-called mono-fractal model. It can be seen as an approximation of the corresponding MFSL, obtainable considering a tangent in the narrow size range experimentally investigated. The mono-fractal scaling laws for fracture energy and tensile strength can be obtained by means of a renormalization procedure: rather than variations in specimen size, a sequence of scales of observation will be taken into account in the following demonstrations (Carpinteri, 1994b).

In order to obtain the renormalized fracture energy, it is necessary to start from the total energy dissipated by fracture, denoted with  $W$ . It is an invariant with respect to the scale of observation. The common way to evaluate this energy is multiplying the fracture energy (corresponding to the macroscopic scale of observation, i.e. the fracture energy experimentally measured, called  $G_F$  in the previous paragraphs, here denoted with  $G_0$ ) by the ligament area (the conventional area  $A$ , denoted with  $A_0$ ). Considering a second more detailed scale of observation, it is possible to take into account the roughness and the self-similar tortuosity characterizing the fracture surface, i.e. the domain in which the energy dissipation occurs. This implies that the area measured in this scale of observation, denoted with  $A_1$ , is bigger than  $A_0$ . Consequently, for the invariance of the total dissipated energy  $W$ ,  $G_1$  will be smaller than  $G_0$ . At limit, considering the asymptotical microscopic scale of observation,  $G_\infty$

will be zero, while  $A_\infty$  will represent an infinite area. This result would be meaningless. Actually,  $A_\infty$  should represent the measure of an invasive fractal domain: it is different from an area, because it has a non-integer physical dimension, bigger than 2 of an additive factor  $d_G$ . Hence,  $A_\infty$  must be substituted by  $A^*$ , that will be a length elevated to an exponent  $2 + d_G > 2$ . As a consequence,  $G_\infty$  must be substituted by  $G_F^*$ , that represents the renormalized size-independent fracture energy, characterized by non-integer physical dimension. Writing the invariance of the total dissipated energy:

$$W = G_0 \cdot A_0 = G_1 \cdot A_1 = \dots = G_n \cdot A_n = \dots = G_\infty \cdot A_\infty \quad (1.62)$$

and applying the above described substitutions, it is possible to write:

$$G_F = G_F^* \cdot \left(\frac{A^*}{A}\right) \cong G_F^* \cdot \left(\frac{D^{2+d_G}}{D^2}\right) \cong G_F^* \cdot D^{d_G} \quad (1.63)$$

in which  $D$  represents a characteristic dimension of the specimen (for TPB tests it is the beam depth: see Figure 1.13). Eq.(1.63) represents the power law that expresses the RILEM fracture energy as a function of the specimen size and of the true material property  $G_F^*$ . In logarithmic form, Eq.(1.63) becomes:

$$\ln G_F = \ln G_F^* + d_G \cdot \ln D \quad (1.64)$$

In a bilogarithmic diagram, Eq.(1.64) is represented by a straight line with a positive slope equal to the fractal exponent  $d_G$  (Figure 1.26a).

Through exactly analogous considerations it is possible to obtain also the renormalized tensile strength. In this case the invariant of the problem is represented by the maximum total force  $F$  that a specimen is able to transmit (for sake of simplicity, a tensile test can be thought). In a macroscopic scale of observation, the total force  $F$  can be expressed by the product of the cross-sectional area  $A_0 = A$  by the tensile strength  $\sigma_0 = \sigma_u$ . With a second more detailed scale of observation, it is possible to note the real nature of material ligament, characterized by self-similar weakening due to cracks, pores, defects, aggregates, voids, inclusions, etc. For this reason the area  $A_1$  measured in this case will be smaller than  $A_0$ . Consequently, for the invariance of the total force  $F$  transmitted by the specimen,  $\sigma_1$  will be bigger than  $\sigma_0$ . At limit, considering the asymptotical microscopic scale of observation,  $\sigma_\infty$  will be infinite, while  $A_\infty$  will represent an area equal to zero. Again, this latter result would be absurd. Actually,  $A_\infty$  should be the measure of the lacunar fractal domain representing the damaged ligament. It will be denoted as  $A^*$ , because it is not an area: it has a non-integer dimension smaller than 2 of a factor  $d_\sigma$ . As a consequence,  $\sigma_\infty$  must be substituted by  $\sigma_u^*$ , that represents the renormalized size-independent tensile strength, characterized by non-integer physical dimension. Writing the invariance of the total applied force:

$$F = \sigma_0 \cdot A_0 = \sigma_1 \cdot A_1 = \dots = \sigma_n \cdot A_n = \dots = \sigma_\infty \cdot A_\infty \quad (1.65)$$

and applying the above described substitutions, it is possible to write:

$$\sigma_u = \sigma_u^* \cdot \left(\frac{A^*}{A}\right) \cong \sigma_u^* \cdot \left(\frac{D^{2-d_\sigma}}{D^2}\right) \cong \sigma_u^* \cdot D^{-d_\sigma} \quad (1.66)$$

Eq.(1.66) represents the power law that expresses the size-dependent tensile strength as a function of the specimen size and of the true material property  $\sigma_u^*$ . In logarithmic form, Eq.(1.66) becomes:

$$\ln \sigma_u = \ln \sigma_u^* - d_\sigma \cdot \ln D \quad (1.67)$$

In a bilogarithmic diagram, Eq.(1.67) is represented by a straight line with a negative slope equal to the fractal exponent  $d_\sigma$  (Figure 1.26b).

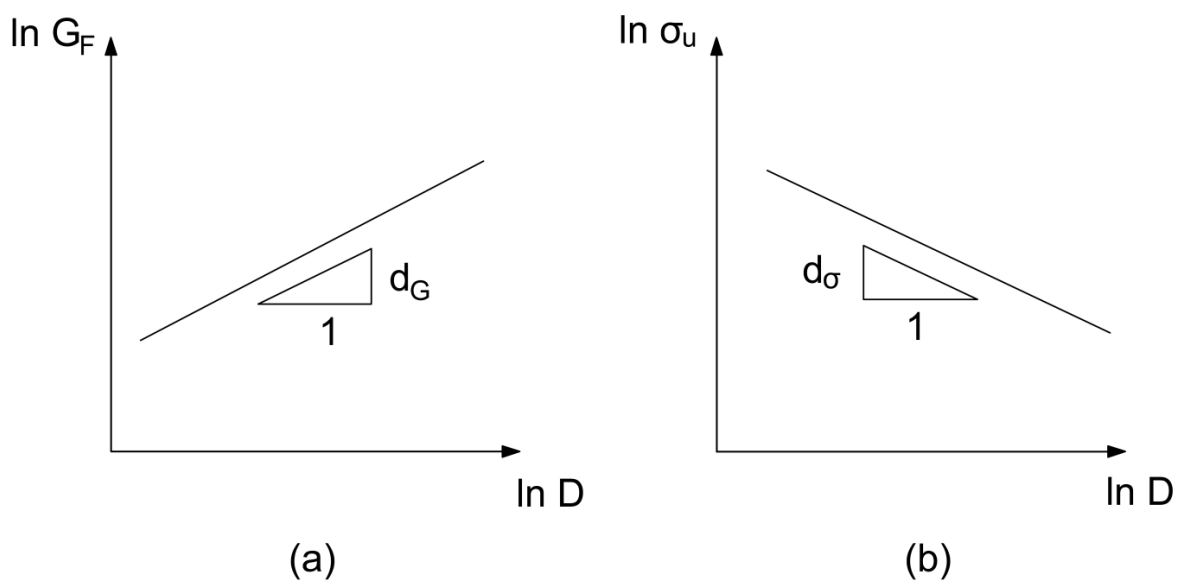


Figure 1.26: Mono-fractal scaling laws for (a) fracture energy and (b) tensile strength

These two scaling laws were used by Carpinteri and Ferro (1994) to interpret the results of uniaxial tensile tests on dog bone shaped concrete specimens of four different sizes (Figure 1.27), with a scale range 1:8 (actually for the bigger size only the tensile strength value is available, because in that test a snap-back instability occurred). These results are represented in Figure 1.28.

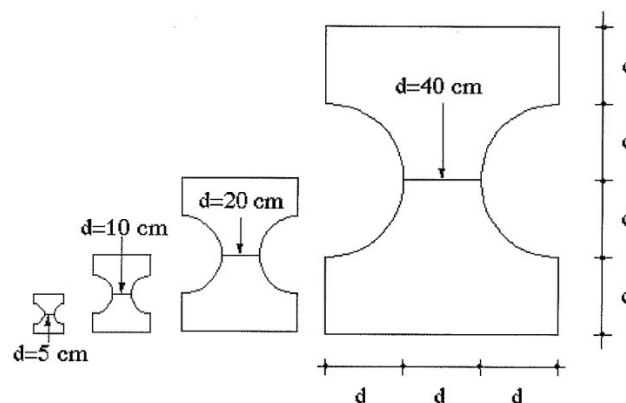


Figure 1.27: Geometry of the specimens used in tensile tests performed by Carpinteri, Ferro (1994)

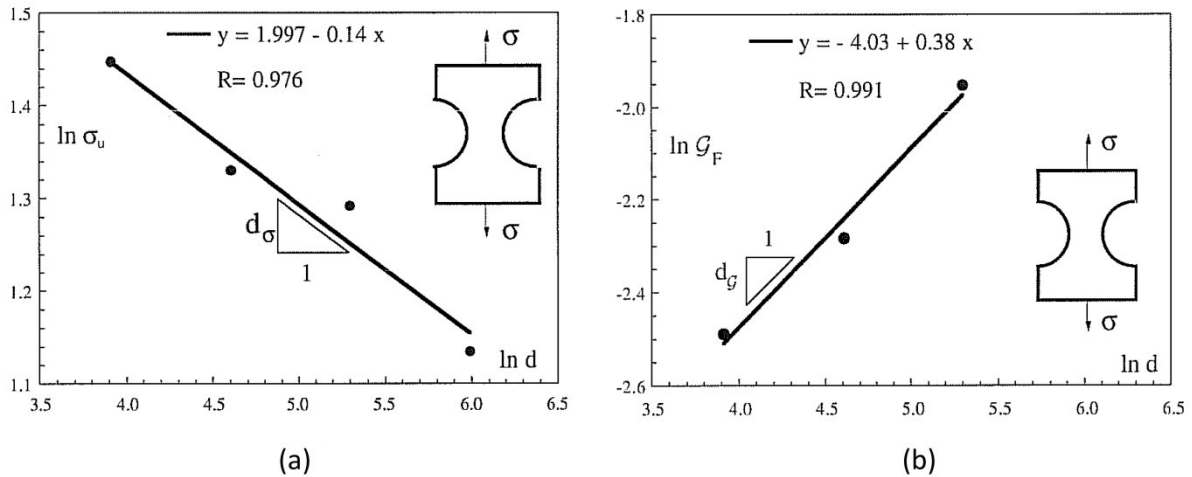


Figure 1.28: Size effect, observed in tensile tests performed by Carpinteri, Ferro (1994), (a) on tensile strength and (b) on fracture energy

Observing Figure 1.28 and using Eq.(1.64) and Eq.(1.67), the application of the mono-fractal scaling laws to fitting the experimental results obtained by Carpinteri and Ferro (1994) provided:

- tensile strength:  $d_\sigma = 0.14$   $\sigma_u^* = 7,39 \frac{N}{mm^{1.86}}$
- fracture energy:  $d_G = 0.38$   $G_F^* = 0.0179 \frac{N}{mm^{1.38}}$

Experimental results show that the dimensional decrement  $d_\sigma$  for the tensile strength and the dimensional increment  $d_G$  for the fracture energy both assume always values between the two limits 0 and  $1/2$ :

- $d_\sigma \cong d_G \cong 0$  means the absence of fractality and consequently of size effects: this happens for macro scales (homogeneous Euclidean regime, Figure 1.24);
- $d_\sigma \cong d_G \cong 1/2$  indicates the maximum possible disorder: this happens for micro scales (fractal Brownian regime, Figure 1.24), and it corresponds to the maximum size effect (LEFM field). It is interesting to note how in this case both  $\sigma_u^*$  and  $G_F^*$  assume the same physical dimension of a stress intensity factor.

In particular, the maximum value  $1/2$  can be explained as follows:

- $d_G = 1/2$  implies that the energy dissipation occurs in a fractal space of dimension 2.5: this represents a Brownian surface, that is the maximum degree of disorder verifiable in a fracture process. In fact  $d_G > 1/2$  would mean, from a geometrical point of view, to have a fracture surface with sharp tortuosity, incompatible with the kinematic of crack opening and closing;
- $d_\sigma = 1/2$  is instead a maximum limit related to the fracture mechanics and to the stress singularity described in Section [1.1.1.1].

For these reasons, apart from the limit situations, the following condition will be valid:

$$d_\sigma + d_G < 1 \quad (1.68)$$

At this point, a generalization of the energy brittleness number (Eq.(1.27)) can be given by Dimensional Analysis (Carpinteri, 1994a):

$$S_E^* = \frac{G_F^*}{\sigma_u^* \cdot D^{(1-d_\sigma-d_G)}} \quad (1.69)$$

If the reversal of physical roles of toughness and strength is supposed to be absurd, the exponent of the characteristic dimension  $D$  in Eq.(1.69) must be positive, i.e. Eq.(1.68) must be respected.

Another important contribution in the present theory came from Cornetti's work (1998). He introduced the concept of fractal strain, so that the fractal scaling law could be extended also on kinematical quantities such as the crack opening displacement. It was experimentally observed, in fact, an increasing tail of the cohesive law (Figure 1.9b) and consequently an increase of the critical displacement  $w_c$  with the increase of specimen size. In other words, the classical cohesive law is not a size-independent material property. The scaling laws on two of the three parameters that describe the cohesive law have been discussed up to this point. With the further introduction of a fractal kinematical quantity, the so-called fractal critical strain  $\varepsilon_c^*$ , it is possible to define a scale-invariant cohesive law, function of the true material properties. The model that was thus obtained is called *fractal (scale-independent) cohesive crack model* (Carpinteri, Chiaia, Cornetti, 2002). In order to define the fractal critical strain, it is necessary to observe how the damage is often not localized onto a single section, but it is spread over a finite band. Experimental evidences provided by Kleiser and Bocek (1986) on metals subjected to tension have allowed to advance the following hypothesis: “[...] damage into heterogeneous media presents fractal patterns [...]. Every damage band, when observed at a sufficiently high resolution, is made out of several smaller bands, which, in turn, appear to be constituted by smaller and smaller bands, and so on” (Carpinteri, Chiaia, Cornetti, 2002). Therefore, considering for example a simple bar subjected to tension, a fractal strain localization can be assumed. Cornetti (1998) proposed the concept of fractal strain acting upon lacunar domains: using again a renormalization procedure, it is possible to define a renormalized critical strain, that will represent the true material property. In fact, the critical displacement  $w_c$  can be expressed, for what concerns the macro scales, how the product of the nominal strain at rupture  $\varepsilon_c$ , times the nominal width  $d$  of the damaged band. However, considering the fractal strain localization,  $w_c$  can be also defined as the fractal measure of the lacunar set constituted by the slip lines in which strain occur ( $d^{1-d_\varepsilon}$ ), times the fractal critical strain  $\varepsilon_c^*$ . Thus, for the invariance of the critical displacement  $w_c$ , it is possible to write:

$$w_c = \varepsilon_c \cdot d = \varepsilon_c^* \cdot d^{1-d_\varepsilon} \quad (1.70)$$

A power law also for the size-dependent critical strain can be thus derived:

$$\varepsilon_c = \varepsilon_c^* \cdot d^{-d_\varepsilon} \quad (1.71)$$

Eq.(1.71) provides the critical strain as a function of the characteristic size  $d$  and the true material property  $\varepsilon_c^*$ , that is not a dimensionless quantity, but it presents an anomalous non-integer physical dimension. Furthermore, Eq.(1.70) shows the power law for the critical displacement, that in logarithmic form becomes:

$$\ln w_c = \ln \varepsilon_c^* + (1 - d_\varepsilon) \cdot \ln d \quad (1.72)$$

In the same way, Eq.(1.71) can be written in logarithmic form as follows:

$$\ln \varepsilon_c = \ln \varepsilon_c^* - d_\varepsilon \cdot \ln d \quad (1.73)$$

The fractal exponent  $d_\varepsilon$  describes the degree of disorder that characterizes the kinematic of damage (Carpinteri, Chiaia, Cornetti, 2002):

- $d_\varepsilon = 0$  represents a ductile behaviour, a diffused damage: this limit value occurs with the micro scales, in which the failure is governed by the conventional critical strain  $\varepsilon_c$ , that is independent of the band size  $d$ ;
- $d_\varepsilon = 1$  represents, on the other hand, a brittle behaviour, with a localization of the damage in correspondence of a single cross-section: this limit value occurs with the macro scales, in which the failure is governed by the critical displacement  $w_c$ , that results in this case a size-independent parameter as in Hillerborg's fictitious crack model.

For the mesoscales, it will be:

$$0 \leq d_\varepsilon \leq 1 \quad (1.74)$$

If  $1 - d_\varepsilon$  is the fractal dimension of the lacunar projection of the damaged sections, and  $2 - d_\sigma$  is the fractal dimension of the lacunar fracture cross section, the energy will be dissipated over the cartesian product of these two fractal domains, that will be the invasive fractal domain of dimension  $2 + d_G$ . A rigorous theorem of mathematical analysis ensures that the fractal dimension of the cartesian product between two fractal domains is equal to the sum of their fractal dimensions. Thus:

$$(2 - d_\sigma) + (1 - d_\varepsilon) = 2 + d_G \quad (1.75)$$

Eq.(1.75) implies that:

$$d_\sigma + d_G + d_\varepsilon = 1 \quad (1.76)$$

Eq.(1.76) provides a very convincing answer to the skepticism of Bazant related to the slope 1/2 of the inclined asymptote in MFSL for tensile strength (Figure 1.24b). In fact, for the micro scales (fractal regime), it has been said that  $d_\varepsilon \cong 0$ , while  $d_G = 1/2$  for kinematic reasons of crack opening and closing: consequently Eq.(1.76) ensures for the fractal regime a value  $d_\sigma = 1/2$ .

At this point, Eq.(1.66) and Eq.(1.70) can be put in a general form, relative to a generic load level:

$$\sigma = \sigma^* \cdot D^{-d_\sigma} \quad (1.77)$$

$$w = \varepsilon^* \cdot D^{1-d_\varepsilon} \quad (1.78)$$

Introducing Eq.(1.77) and Eq.(1.78) in Eq.(1.20), it is possible to obtain the fractal cohesive law, that represents the true material property:

$$G_F = \int_0^{w_c} \sigma \cdot dw = \int_0^{\varepsilon_c^*} \sigma^* \cdot D^{-d_\sigma} \cdot D^{1-d_\varepsilon} \cdot d\varepsilon^* = D^{1-d_\sigma-d_\varepsilon} \cdot \int_0^{\varepsilon_c^*} \sigma^* \cdot d\varepsilon^* \quad (1.79)$$

Remembering the power law that describes the scale effects on fracture energy (Eq.(1.63)), it is clear that Eq.(1.76) is respected ( $1 - d_\sigma - d_\varepsilon = d_G$ ), while the renormalized fracture energy results to be equal to the area under the diagram  $\sigma^* - \varepsilon^*$  that represents the fractal cohesive law (Figure 1.29b).

$$G_F^* = \int_0^{\varepsilon_c^*} \sigma^* \cdot d\varepsilon^* \quad (1.80)$$

During the softening branch, after the peak load,  $\sigma^*$  decreases from the maximum value  $\sigma_u^*$  up to zero, when  $\varepsilon^* = \varepsilon_c^*$ ; in the meanwhile, the non-damaged parts of the tensed bar are subjected to an elastic unloading, according to the pre-peak diagram  $\sigma - \varepsilon$  (Figure 1.29a).

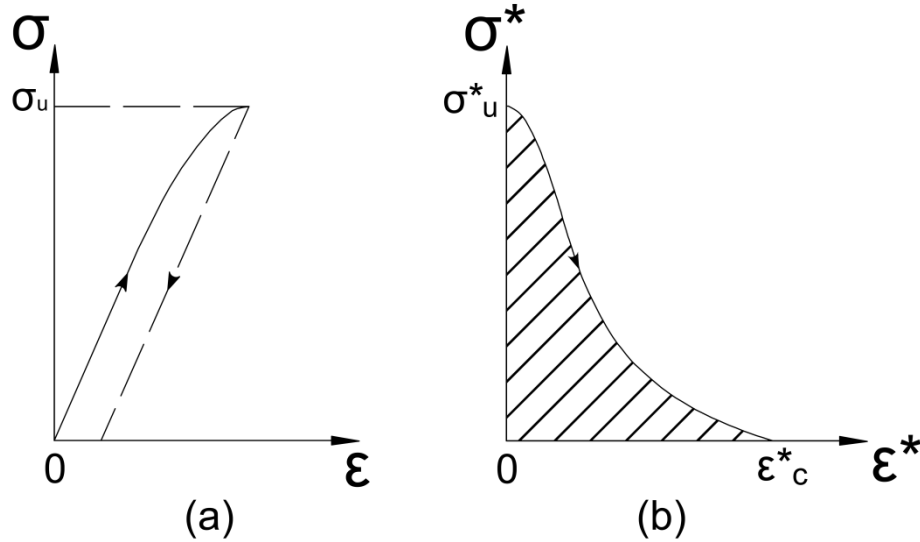


Figure 1.29: Double constitutive law: (a) stress-strain, (b) fractal (scale-independent) cohesive law

Considering again the experimental results obtained by Carpinteri and Ferro (1994) with uniaxial tensile tests on dog bone shaped concrete specimens of different sizes, Figure 1.30 shows the  $\sigma - \varepsilon$  and the  $\sigma - w$  diagrams (Carpinteri, Chiaia, Cornetti, 2002). In this latter,  $w$  represents the displacement localized in the damaged band, calculated by subtracting from the total one the displacement due to elastic and inelastic pre-peak deformation.

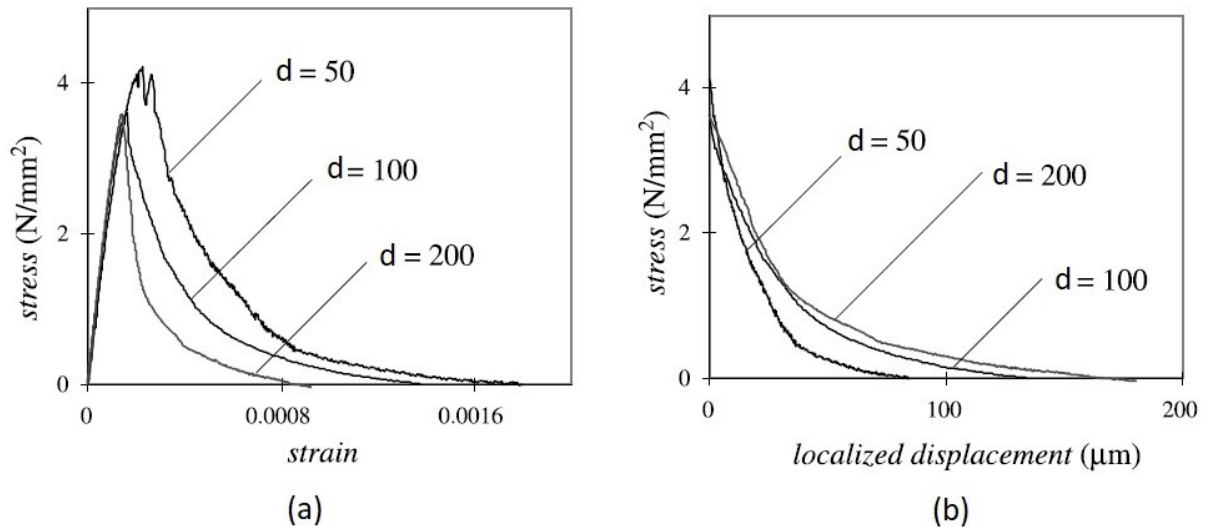


Figure 1.30: (a) Stress vs. strain and (b) cohesive law related to uniaxial tensile tests performed by Carpinteri and Ferro (1994)

Figure 1.30 shows that, with the increase of specimen size, the tensile strength  $\sigma_u$  decreases, while the critical displacement  $w_c$  increases. Furthermore, it can be seen how the area under the cohesive laws in Figure 1.30b depends by specimen size. On the contrary, using Eq.(1.77) and Eq.(1.78) it is possible to obtain the true material property, i.e. the fractal cohesive law (Figure 1.31). The value of the fractal exponent  $d_\varepsilon$  is obtained from Eq.(1.76):  $d_\varepsilon = 1 - d_\sigma - d_G = 1 - 0.14 - 0.38 = 0.48$ .

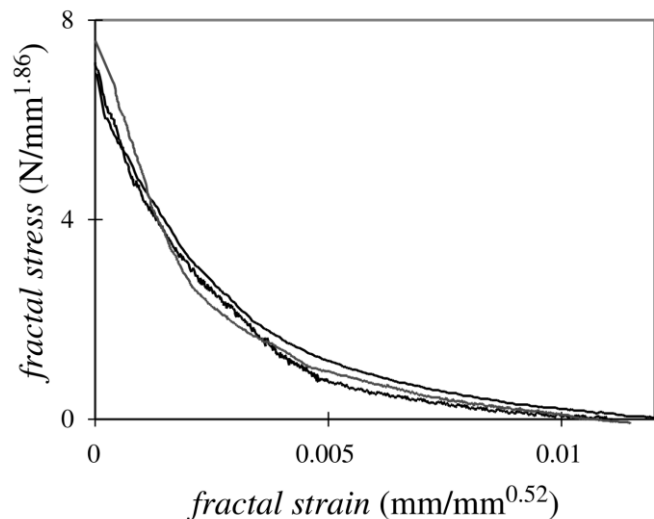


Figure 1.31: Fractal cohesive law related to uniaxial tensile tests performed by Carpinteri and Ferro (1994)

As expected, the three size-dependent cohesive laws represented in Figure 1.30b collapse onto a unique curve, that represents the fractal (scale independent) cohesive law (Figure 1.31).

This theory, described up to this point for tensile tests, was applied also in the case of uniaxial compression tests on concrete specimens of different sizes (Carpinteri, Corrado, 2009). Scale effects, in fact, influence also the compression strength and the post-peak softening branch of the  $\sigma - \varepsilon$  diagram. Experimental evidences show

that a strong localization of deformations takes place, also in compressed specimens, during the softening regime. Therefore, the energy dissipation occurs on an internal surface rather than in the volume. Hence, a close analogy exists between the tensile and the compression tests. However, whilst in tension the localized displacement corresponds to a crack opening, in compression it consists in a material interpenetration. Consequently the cohesive crack model is not applicable. Nevertheless, a new model, analogous to the cohesive crack model, can be used for concrete crushing: it is called Overlapping Crack Model (Carpinteri et al., 2007). This is characterized by a double constitutive law: a stress-strain relationship until the compression strength  $\sigma_c$  (Figure 1.32a), and a post-peak stress-displacement (overlapping) law describing the concrete crushing (Figure 1.32b). Similarly to the cohesive law (Figure 1.9b), the three parameters that describe an overlapping law are: the compression strength  $\sigma_c$ , the critical value of displacement  $w_{cr}^c$  (in this case this represents an interpenetration) and the crushing energy  $G_c$  (the analogous of fracture energy for compression). This latter is equal to the area under the overlapping law (Figure 1.32b).

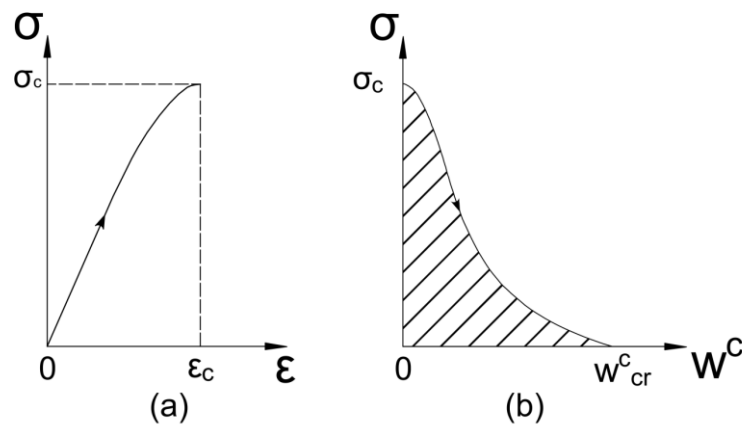


Figure 1.32: Overlapping Crack Model: (a) pre-peak stress vs. strain diagram, (b) overlapping law

In the Overlapping Crack Model, these three parameters, and consequently the overlapping law (Figure 1.32b), are considered material properties. Actually they are scale dependent, because of the strain localization in the specimen at failure. Experimental results demonstrate that compression strength decreases with the increase of specimen size. Therefore, the fractal theory was extended also to the compression problem, supposing that the energy dissipation occurs in a fractal domain of dimension between 2 (surface) and 3 (volume). In this case, however, Carpinteri and Corrado (2007) did not consider the scale effects on compression strength, because this mechanical parameter did not present a clear trend in the experimental results obtained. Consequently, Eq.(1.76) becomes, for the compression problem:

$$d_G + d_\varepsilon = 1 \quad (1.81)$$

Measuring the area under the stress-displacement curves experimentally obtained, Carpinteri and Corrado (2007) determined the values of crushing energy

corresponding to the different specimen sizes. Performing a best-fitting procedure on these results, reported in a bilogarithmic diagram, using a linear regression, it was possible to obtain, by means of a law analogous to Eq.(1.64), the fractal exponent  $d_G$  and the renormalized crushing energy  $G_C^*$ , i.e. the true material constant. They resulted:

- $d_G = 0.27$
- $G_C^* = 5.47 \frac{N}{mm^{1.27}}$

Knowing the value of  $d_G$ , the other fractal exponent  $d_\varepsilon$  can be obtained using Eq.(1.81):

- $d_\varepsilon = 1 - d_G = 0.73$

At that point the fractal overlapping laws for the different specimen sizes and slenderness can be derived. They are represented in Figure 1.33.

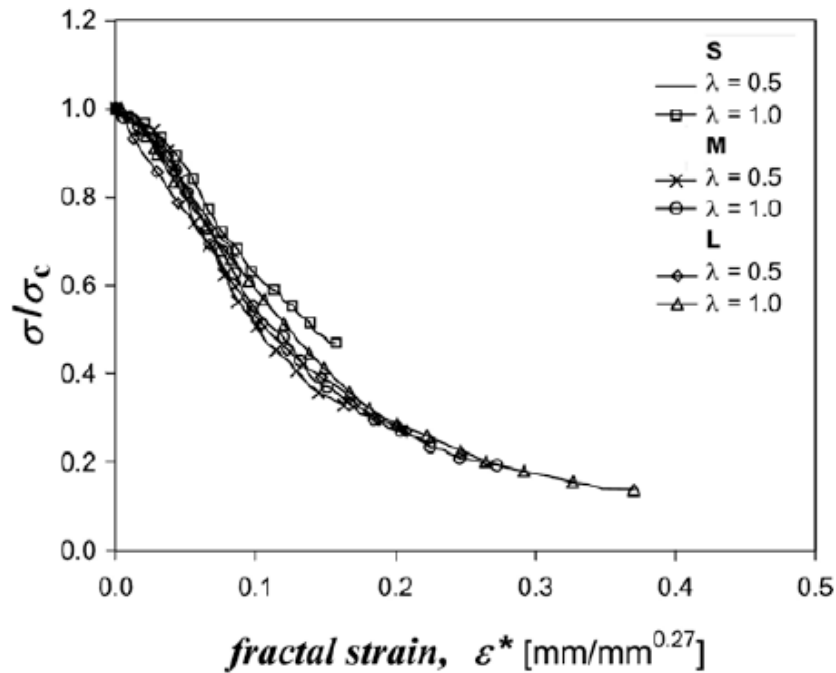


Figure 1.33: Fractal Overlapping Laws obtained by Carpinteri, Corrado (2007)

As expected, a good superposition of the fractal overlapping laws is obtained, because this law is the true scale independent material property.

The method described in this paragraph, so far applied for uniaxial tensile and compression tests, will be extended, in the second part of the present thesis, to the bending problem. The mono-fractal scaling laws will be applied on the results of TPB tests, performed on plain concrete specimens of different sizes; then, considering also in that case the kinematic aspect, a fractal cohesive law for the bending problem will be determined, as a function of three renormalized material properties.

## 1.2 The Acoustic Emission Technique

In order to perform damage monitoring during the TPB tests carried out for the scope of the present thesis, Acoustic Emission Technique was applied. In this section, a brief review of the main concepts of this kind of analysis is presented. Particular attention will be reserved only to the parameters of interest for the scope of the present work.

### 1.2.1 General aspects

Acoustic emission (AE) technique is a non-destructive and non-invasive method for the evaluation of the physical condition of a structure during its loading. It allows to:

- obtain information about the actual situation of the structure;
- estimate the energy emitted during crack propagation;
- estimate the mode of fracture propagation;
- estimate the speed of the damage advancement;
- identify the position of the damage in the structure.

This monitoring method is similar to the one used in earthquake control. Rather than the seismic waves, in this case the transducers, attached on the surface of the structural element, have to capture the transient elastic waves generated by cracking (Figure 1.34).

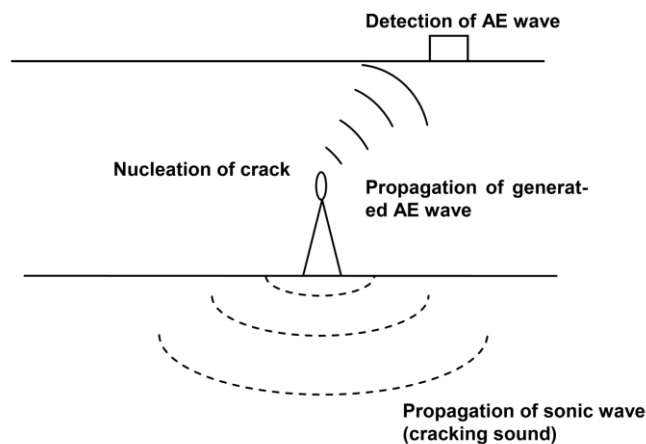
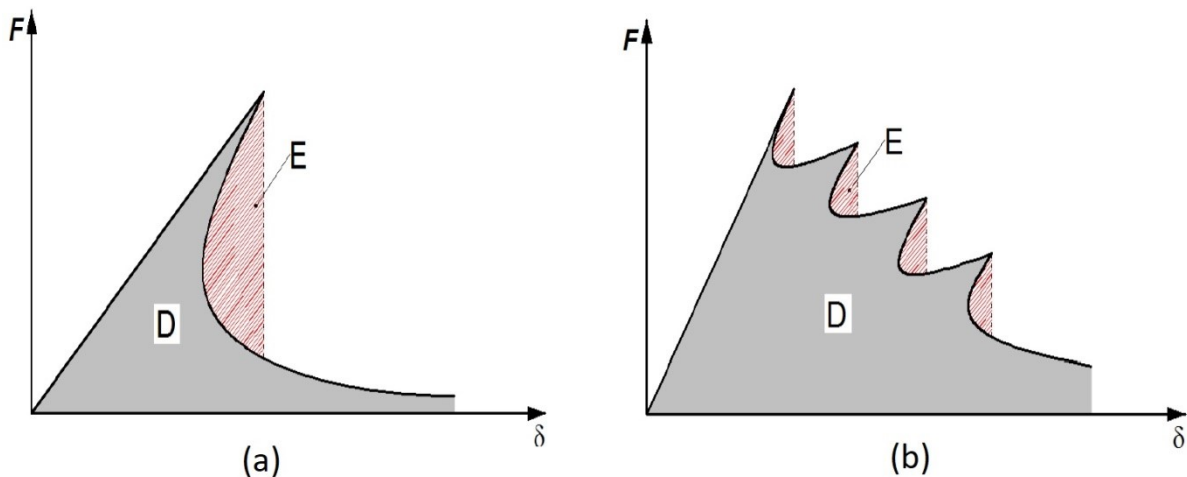


Figure 1.34: Detection of AE waves (Grosse, Ohtsu, 2008)

Fracture in a material, in fact, is accompanied by an energy release that generates the propagation of these waves within the bulk of the element; when they reach the surface, they can be received by the sensors. In AE monitoring, piezoelectric sensors are generally used. They are able to convert the dynamic motions captured on the surface of the material into electric signals. AE technique can be applied on various kinds of materials. However, AE waves, before being captured by the sensors, will be subjected to an attenuation that depends on the heterogeneity of the monitored material. These heterogeneities could represent in fact diffraction elements or

reflective surfaces for these waves. In typical metallic alloys, for instance, the attenuation is low; in that case, therefore, the frequencies of AE signals will be higher respect to the case of disordered materials such as concrete. Anyway, AE signals are in the ultrasonic field; their wavelength is of the order of magnitude of the flaw that generates the elastic wave. Thus, high frequency waves are generated from small discontinuities (that usually occur at the beginning of the damage process), whereas low frequency ones are produced by large cracks.

From an energetic point of view, it is necessary to distinguish the dissipated energy on the fracture surface from the emitted one, released in the form of AE waves. For quasi-brittle materials such as concrete, the following energy balance subsists (Carpinteri et al., 2016): the total released energy (i.e. the total elastic energy stored in the body) is equal to the sum of the energy dissipated by material damage (area D in Figure 1.35a) and the energy emitted through propagation of elastic waves (area E in Figure 1.35a). As a matter of fact, the dissipated energy on the fracture surface (area  $W_0$  under the load-displacement curve: see also Figure 1.20) is generally smaller than the total elastic energy supplied to the specimen by the testing machine: the remaining part of energy that is not absorbed by material, is emitted in various forms, mainly by AE waves. Important AE activity occurs in correspondence of snap-back instabilities. Nevertheless a global snap-back (Figure 1.35a) can happen only in very brittle structures. Generally a globally stable response (softening branch) is observed, in which, however, local snap-back instabilities can be present (Figure 1.35b): in these cases, the acoustic emission is related to these local phenomena. The local snap-back instabilities are caused by material heterogeneities or, eventually, by the presence of fibers or reinforcement steel bars, that produce a discontinuous damage propagation.



**Figure 1.35: Simplified load-displacement curves obtainable with a quasi-brittle material: distinction between Dissipated and Emitted energy in case of (a) global or (b) local snap-back instability**

After the acquisition of signals, it is convenient to perform a frequency analysis in order to eliminate the unwanted components, due to the environmental noises, characterized by frequencies lower than 50 kHz: it can be done by means of the FFT

algorithm (Fast Fourier Transform). A typical AE signal is represented in Figure 1.36 (Grosse, Ohtsu, 2008). The conventional parameters used to describe an AE signal are pointed out in the figure. Grosse, Ohtsu (2008) and the Recommendation of RILEM TC 212-ACD (2010) give the definitions of the principal technical terms used in AE analysis (Figure 1.36):

- *AE signal*: “the electrical signal detected at a sensor, which is converted through the detection of AE wave (elastic wave)”;
- *Hit*: a waveform that, exceeding the threshold, is recorded and stored in memory; the threshold represents a “pre-set voltage level, which has to be exceeded before one AE signal is detected and processed”: it depends on the monitored material (for concrete it is usually 30-50 dB);
- *AE ring-down counts*: “the number of times within the duration, where one signal (waveform) exceeds a pre-set threshold”;
- *Event*: “a group of AE hits received from a single source by two or more channels”;

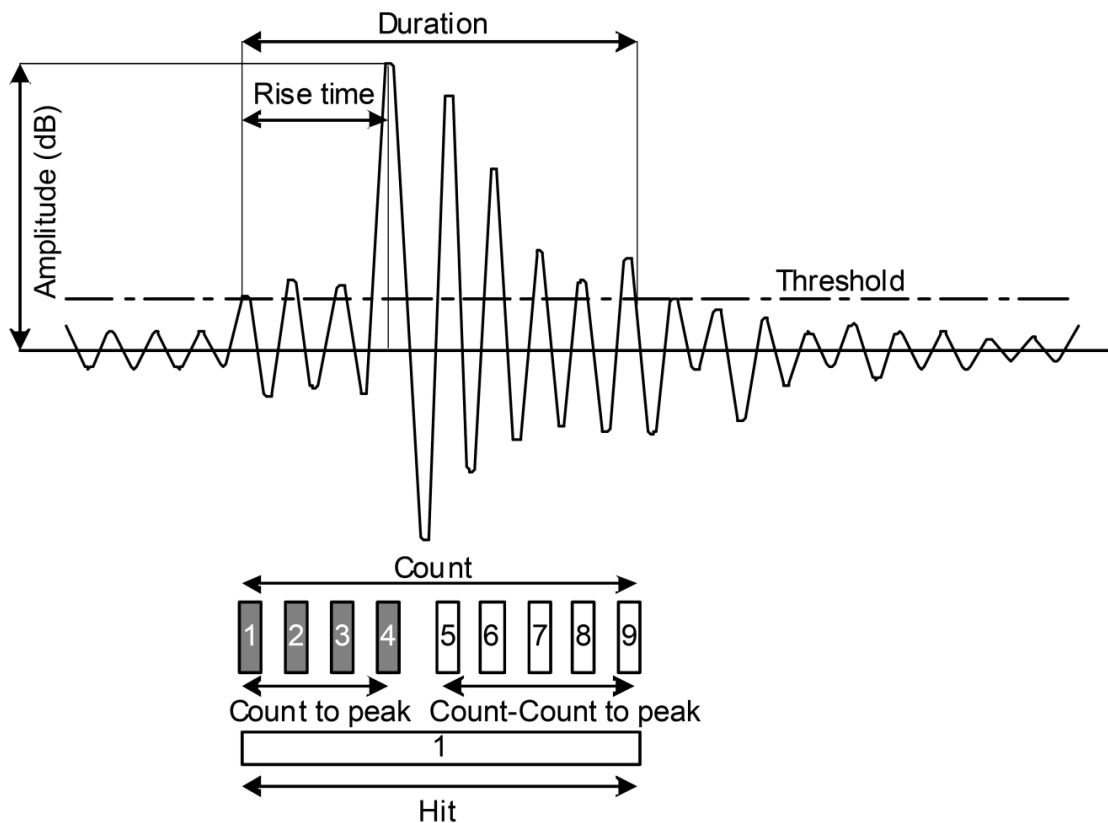


Figure 1.36: AE waveform parameters

- *Duration* ( $d$ ): time interval between the first and the last threshold crossing by the waveform;
- *Amplitude* ( $A$ ): the peak voltage of the signal waveform; it depends on the magnitude of source event. It is usually expressed in Decibel:

$$A[dB] = 20 \cdot \log_{10} \left( \frac{V}{V_0} \right) \quad (1.82)$$

where  $V_0$  is the maximum amplitude in Volt of the background noise;

- *Rise Time (RT)*: time interval between the beginning of the signal and the time of the peak amplitude;
- *Energy (E)*: it is generally defined as “a measured area under the rectified signal envelope”; an approximate way to evaluate this area is:

$$E = \frac{1}{2} \cdot A \cdot d \quad (1.83)$$

Thus the energy is generally expressed in [ $ms \cdot V$ ];

- *Average Frequency (AF)*: referring to one hit,  $AF$  is equal to the count divided by the duration.

A typical AE measuring system consists of the following devices (RILEM TC 212-ACD, 2010):

- *Sensors*: piezoelectric sensors are generally used to detect AE waves; two kinds of AE sensors can be distinguished:
  - *Resonance-type sensors*: they are the most sensitive around the resonant frequency;
  - *Broad-band sensors*: they are less sensitive than the resonance ones, and so the energy of the signals captured by this kind of sensors is smaller; however, they are able to capture signals characterized by frequencies within a large bandwidth.
- *Amplifiers*: AE signals captured by the sensors are amplified by a pre-amplifier and then by a main amplifier before being processed; in concrete, for instance, the gain due to amplification can reach 40-60 dB.
- *Filters*: it is necessary to choose a frequency range of interest, in order to eliminate the noises, i.e. components within the captured signal related to causes other than AE phenomena.

### 1.2.2 Parametric AE Analysis: Crack classification

In concrete, AE technique can be used also in order to classify the active cracks.

In fracture mechanics, the following fundamental modes of crack loading are distinguished:

- *Mode I cracks: opening mode* (Figure 1.37a)  
It happens when the crack is symmetrically loaded by tensile normal stresses. These stresses tend to increase the distance between the fracture surfaces in the direction perpendicular to the plane of the crack;
- *Mode II cracks: sliding mode* (Figure 1.37b)  
It happens when the crack is anti-symmetrically loaded by in-plane shear stresses, that cause a displacement of crack surfaces in the plane of the crack, perpendicularly to the leading edge;

- Mode III cracks: *tearing mode* (Figure 1.37c)  
It happens when the crack is subjected to a three-dimensional stress field; this mode is in fact produced by out-of-plane shear.

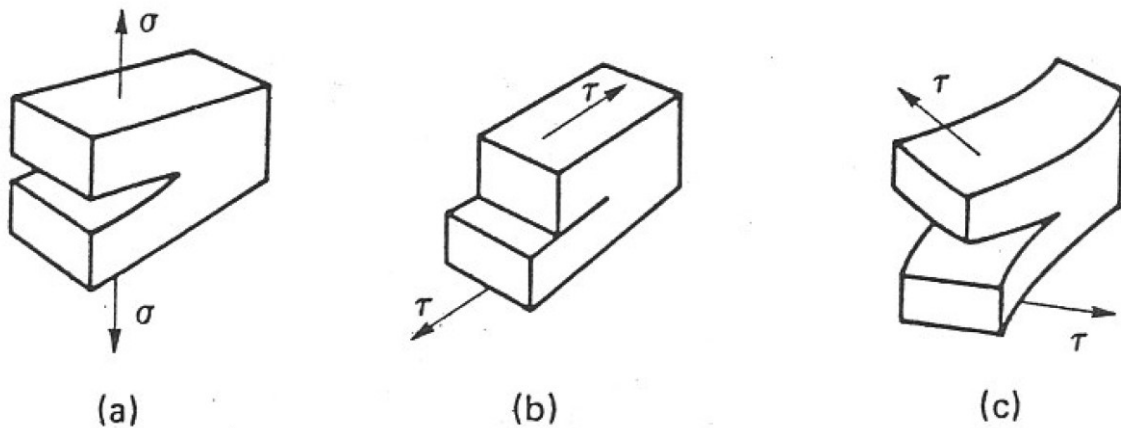


Figure 1.37: The three elementary modes of cracking: (a) opening, (b) sliding, (c) tearing

A simple crack type classification method using AE technique was proposed by Ohtsu (Grosse, Ohtsu, 2008). It is based on two AE parameters:

- the average frequency ( $AF$ ) (expressed in kHz);
- the Rise Angle ( $RA$ ) (expressed in ms/V).

This latter is defined as the ratio of the Rise Time ( $RT$ ), expressed in millisecond, to the peak amplitude ( $A$ ), expressed in Volt:

$$RA = \frac{RT}{A} \quad (1.84)$$

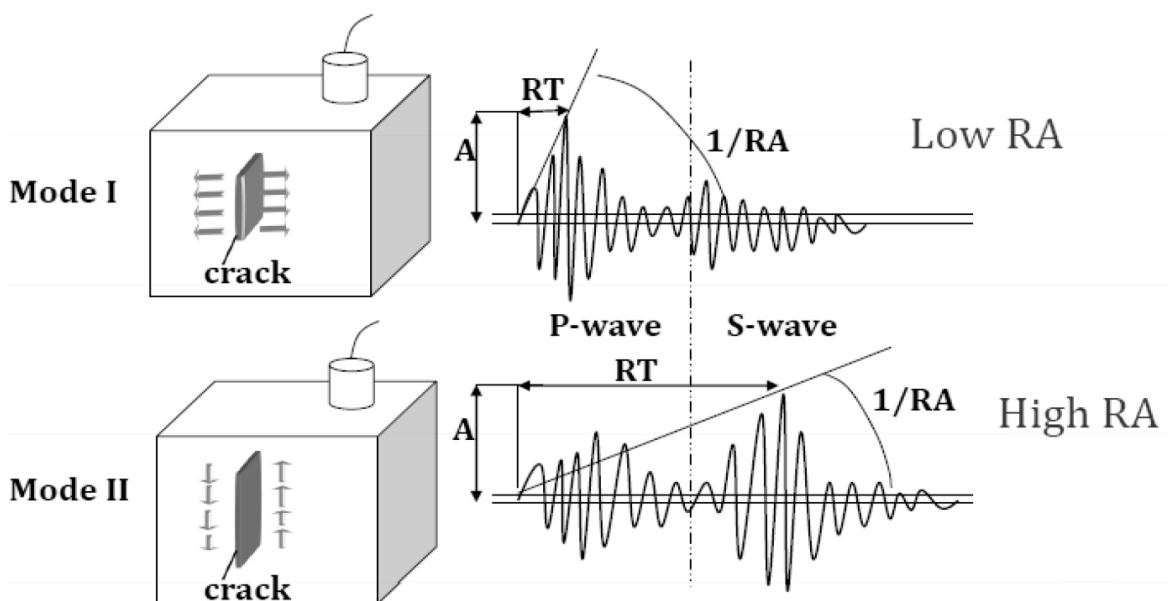


Figure 1.38: Different values of RA parameter in case of tensile and shear events

Figure 1.38 (Carpinteri et al., 2016) shows the reason why RA parameter can be considered a useful tool for a crack classification. Remembering that P-waves (compressional waves) are faster than S-waves (shear waves) and consequently are the first to be captured by sensors, it is possible to observe that:

- low RA values correspond to signals with a prevalence of P compressional waves; it means that they correspond to opening cracks, caused by normal stresses  $\sigma$ ;
- high RA values correspond to signals with a prevalence of S shear waves; it means that they correspond to sliding cracks, caused by tangential stresses  $\tau$ .

In concrete specimens or structures, the classification of crack types proposed by Ohtsu uses a combination of the Average Frequency and Rise Angle values. Each signal can be represented by a point in the  $AF - RA$  diagram (Figure 1.39): if the point is placed above the bisector of this diagram (high frequency and low RA), it represents a mode I crack; if the point is below this bisector (low frequency and high RA), it corresponds to a mode II crack.

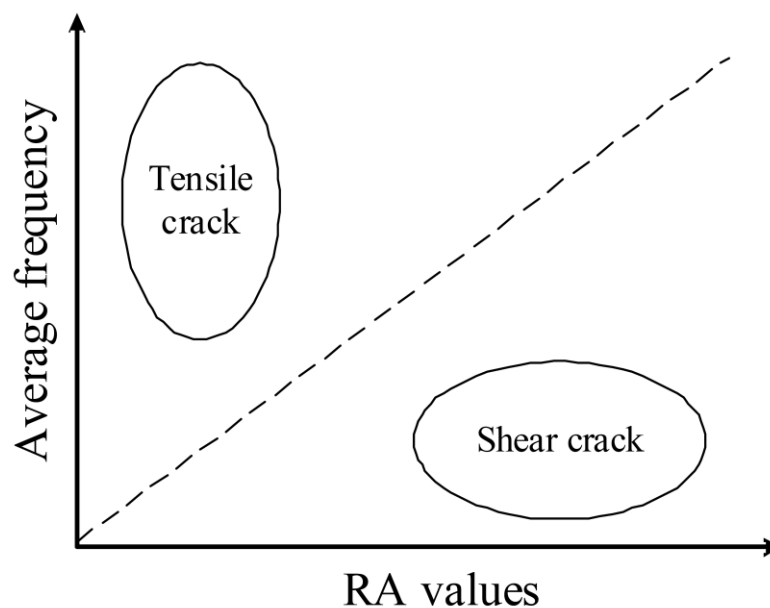


Figure 1.39: Crack type classification proposed by Ohtsu

### 1.3 Dynamic Identification

In addition to AE analysis, a further non-destructive technique of damage monitoring has been used in the present thesis: the Dynamic Identification. It consists in the analysis of the free response signals, captured during the test, in order to reveal variations in natural frequencies and modal shapes. These variations are caused, in fact, by a stiffness reduction of specimen consequently to the progress of damage. Through an inverse procedure, it is possible to obtain information about the damage

severity (e.g. the advancement of a crack), for example by using a finite element model.

### 1.3.1 Non-destructive control based on vibrations

In general, in the monitoring of real structures, it is usually necessary to use more than one method in parallel, because each non-destructive technique presents both pros and cons. For instance, AE analysis represents a valid technique to identify the presence of a damage and to receive an alarm when it is evolving. However, this technique presents also practical limitations when it is necessary to identify the number of defects in the structure, their position and their entity (Ruotolo, 1997). Furthermore, if the AE sensors are placed in points remote from the location of the damage, this technique becomes inefficacious. For this reason, in practical situations there is a need for a technique able to recognize the presence of a damage in the structure using a limited number of sensors. Dynamic Identification technique possesses this requirement. In fact, even with just one sensor, if positioned in a strategic point of the structure, it is possible to estimate the reduction of natural frequencies and, consequently, to reveal the presence of a damage, though it is very distant from this unique sensor.

In other words, the analysis of the dynamic response of the structure represents a global inspection technique.

The development of damage in a structure implies, as expected, a decrease of stiffness, and so a greater deformability for a fixed load. This change of structural behaviour is connected to the decrease of the natural circular frequency, equal to (for a multi degree of freedom discrete system):

$$\omega_n = \sqrt{\frac{k_n}{m_n}} \quad (1.85)$$

Eq.(1.85) shows that a decrease of stiffness  $k_n$  (i.e. an increase of compliance of the structure) implies (supposing that the mass  $m_n$  does not change) a decrease of structure natural frequencies. Furthermore, even the modal curvatures/shapes and the modal dumping will vary.

For these reasons, the Dynamic Identification is based on the correlation between the variation of the dynamic response of the structure (decrease of natural frequencies, changes in modal shapes, etc.) and the severity of damage. Using this technique it is possible, for example, to estimate the crack depth. In the second part of this work, a finite element model of the specimen is used to run a modal analysis for different values of the crack depth. If the real natural frequencies are evaluated during the tests with the Dynamic Identification procedure, it is possible to associate, for a given variation in natural frequencies, the approximate entity of crack propagation.

In real structures monitoring, therefore, a first acquisition of free response signals is performed when the structure has just been completed and so it is intact; it can be done using a low number of sensors (e.g. accelerometers) well positioned on the structure. If a finite element model is used, it can be calibrated (*model updating*) using this first acquisition of natural frequencies. At that point it is necessary to measure periodically the natural frequencies of the structure, in order to understand if they are changed; alternatively, if AE monitoring is also present, a second acquisition of the dynamic response of the structure can be performed when AE analysis points out an alarm situation. Knowing the variation of natural frequencies, it is possible, using the finite element model, to estimate the damage entity by the inverse procedure above described. Furthermore, the Dynamic Identification permits also to localize the damage within the structure, by the observation of localizations in modal curvatures.

## 2 Experimental campaign and results

### 2.1 Outline of experiments

In order to study scale effects on fracture energy and tensile strength in a quasi-brittle material, a set of three-point bending tests was performed on pre-notched plain concrete specimens. These tests were conducted in the MASTRLAB laboratory of Politecnico di Torino, following the RILEM procedure described in Section [1.1.1.4] (RILEM TC 50-FMC,1985). Therefore, specimen sizes prescribed by this Recommendation were taken into account (Table 1). Overall, nine TPB tests will be considered for the purpose of the present thesis. Among these, two tests were already analysed in the article by Carpinteri, Lacidogna, Corrado, Di Battista (2016): those results, in terms of load-displacement curves, will be used also in this work. This is possible because those tests were also conducted following the above mentioned RILEM Recommendation.

Specimens with a depth of 10 cm were tested using a servo-hydraulic MTS universal testing machine (Figure 2.1), while the tests on the other three larger sizes were conducted using a Baldwin testing machine of 500 kN produced by Zwick/Roell (Figure 2.2).



Figure 2.1: Testing machine used for 10 cm specimens



Figure 2.2: Testing machine used for 20 cm, 30 cm, 40 cm specimens

All the specimens were tested until the final failure was reached.

AE analysis was applied in all the tests (except for 20 cm specimen size, for which it is possible to use the results reported in the article by Carpinteri, Lacidogna, Corrado, Di Battista (2016)) in order to execute a damage monitoring. In addition, during two tests, Dynamic Identification technique was also applied and free response signals, in different steps of these tests, were captured.

### 2.1.1 Test set-up (RILEM TC50-FMC Recommendation)

The Recommendation of RILEM TC 50 –FMC provides a method to estimate the fracture energy of a concrete, that is a purpose of the present work in order to discuss the scale effects on this parameter. For this reason, the tests were performed following these standardized procedures.

Only one test, on a 10 cm specimen, was conducted by controlling the crack mouth opening displacement (CMOD), while all the others were conducted by imposing a constant velocity to the vertical displacement  $\delta$  of the hydraulic jack. In all cases, a

stable behaviour was obtained; this allows to use Eq.(1.45) for the evaluation of fracture energy.

### 2.1.1.1 Specimens characteristics

Figure 2.3 shows in scale the specimen sizes recommended by RILEM (Table 1).

Table 2 summarizes the TPB tests which are considered for the scope of the present thesis. Test\_100\_3 and Test\_200\_2, marked with an asterisk in Table 2, were taken from the article by Carpinteri, Lacidogna, Corrado, Di Battista (2016); all the others are analysed for the first time in this work.

Actually, the present experimental campaign was initially planned to test three samples for each size recommended by RILEM. Nevertheless, the missing tests in Table 2 are due to the extreme fragility of the bigger specimens, which fractured already during handling.

All the specimens presented a central pre-notch extended for one half of the beam depth ( $a/D = 1/2$ ), with a width of 4 mm in 10 cm specimens, and of 6 mm in the others.

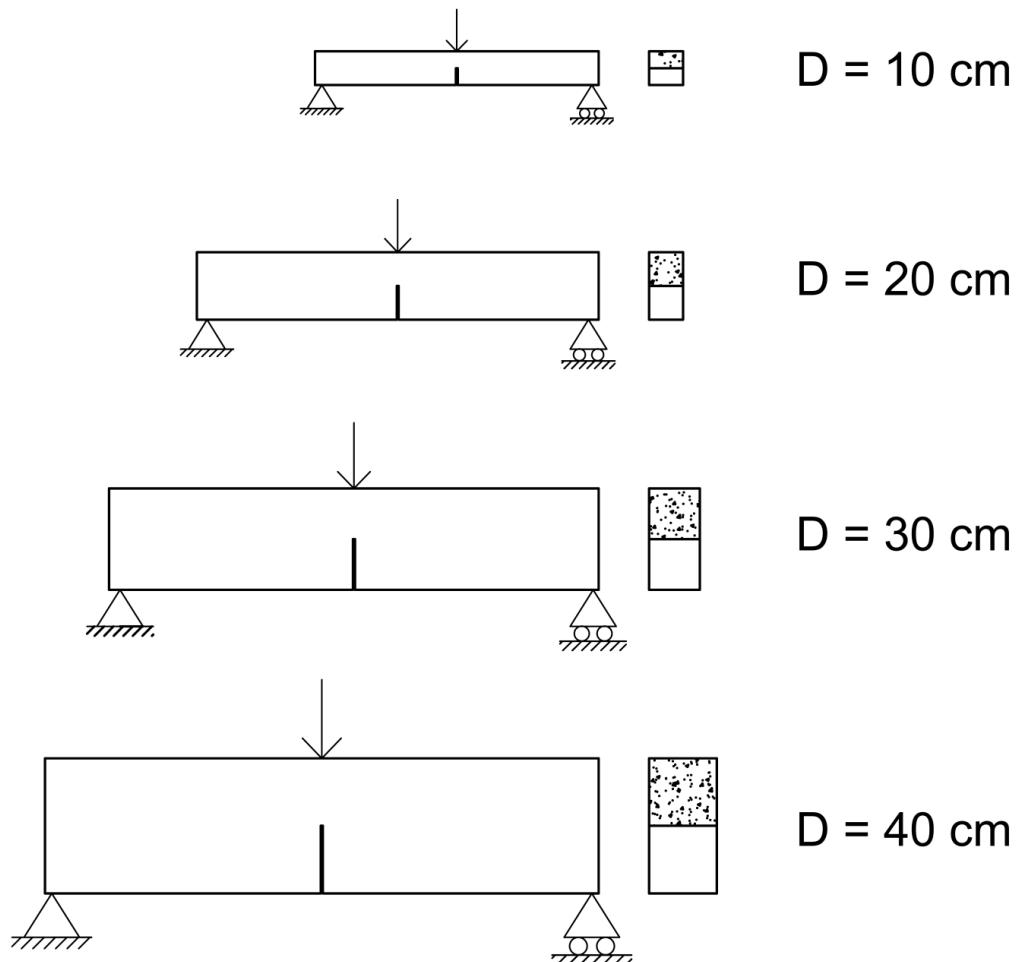


Figure 2.3: Specimen sizes recommended by RILEM TC 50-FMC

<i>Depth (D) [mm]</i>	<i>Number of specimens</i>	<i>Name of the test</i>
100	3	Test_100_1
		Test_100_2
		Test_100_3*
200	2	Test_200_1
		Test_200_2*
300	1	Test_300_1
400	3	Test_400_1
		Test_400_2
		Test_400_3

Table 2: Number and name of TPB tests considered for each size

Test\_100\_1, Test\_100\_3, Test\_200\_2 were conducted by controlling the CMOD rate ( $2 \cdot 10^{-3}$  mm/s). All the others were performed by increasing the vertical displacement  $\delta$  of the hydraulic jack with a constant velocity; this was set differently in the various tests (it depended by the specimen brittleness) and the values are indicated in Table 3.

<i>Name of the test</i>	<i>Constant velocity of the hydraulic jack</i>
Test_100_2	$2 \cdot 10^{-3}$ mm/s
Test_200_1	$2 \cdot 10^{-3}$ mm/s
Test_300_1	$1 \cdot 10^{-3}$ mm/s
Test_400_1	$1 \cdot 10^{-3}$ mm/s
Test_400_2	$2 \cdot 10^{-3}$ mm/s
Test_400_3	$2 \cdot 10^{-3}$ mm/s

Table 3: Feed rate of tests performed by controlling the vertical displacement of the hydraulic jack

### 2.1.1.2 Material properties

The specimens were made with different concrete mixes, containing aggregate with different sizes. Each specimen size recommended by RILEM TC 50-FMC is characterized by a different maximum diameter of aggregate, according to Table 1: the larger is the beam, the larger is the maximum aggregate size. For example, in specimens with a depth of 40 cm, the aggregate diameter can reach 64 mm: this can be observed in Figure 2.4, in which a photo of a cracked ligament of those specimens is reported.

Nevertheless, the four concrete mixes were designed in order to have the same nominal average compression strength. In particular, the average values of mass density  $\rho$  and characteristic compression strength  $R_{ck}$  of these concretes were estimated by laboratory tests performed on five cubic specimens of side 160 mm. The remaining mechanical properties were evaluated according to the Italian

technical regulations (NTC 2008); they are reported in Table 4 (Lacidogna, Piana, Carpinteri, 2017).



Figure 2.4: Cracked ligament area in a 40 cm specimen

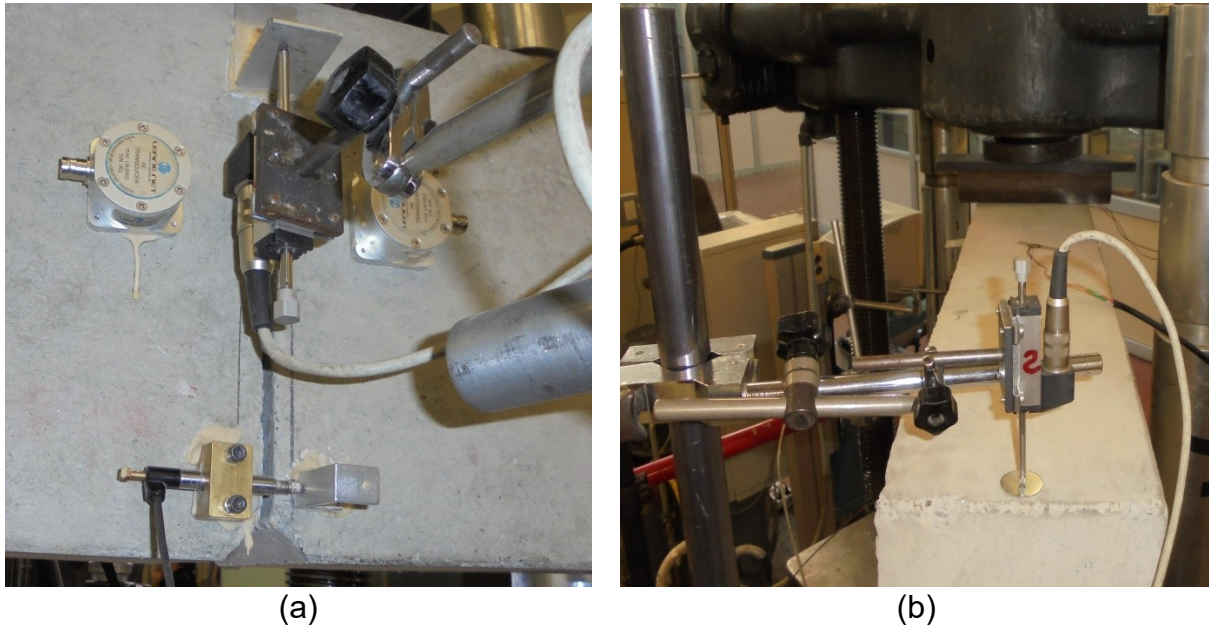
Mass density $\rho$ [kg/m <sup>3</sup> ]	2310
Cubic compression strength $R_{ck}$ [MPa]	26.4
Cylindrical compression strength $f_{ck}$ [MPa]	21.9
Average tensile strength $f_{ctm}$ [MPa]	2.4
Average Young's modulus $E_{cm}$ [MPa]	30570

Table 4: Average mechanical properties of concretes

### 2.1.2 Sensors and instruments

The loading apparatus consisted of two cylindrical rollers that supported the specimen, and a cylindrical roller centred at the top, used to apply the load (Figure 2.1 and Figure 2.2). Actually the testing machines work by raising the base upwards (hydraulic jack) and maintaining the central point fixed. During the tests on 10 cm specimens, CMOD was measured using a clip-on gage applied to the mouth of the notch, while the vertical displacement of the mid-section is taken equal to the displacement of the hydraulic jack. During the tests on the other larger specimens,

instead, the CMOD was measured by an extensometer (Figure 2.5a), while, in order to measure the correct displacement of mid-span section, three transducers were applied on the sample: two in correspondence to the supports (Figure 2.5b), the other one in the mid-span section (Figure 2.5a). However, in order to be consistent with the measures considered for smaller specimens, also in these cases the vertical displacement of the mid-section will be taken equal to the stroke of the hydraulic jack.



**Figure 2.5:** (a) Extensometer for the measure of CMOD and transducer in the mid-span section; (b) transducer in correspondence of the support

As already said, the Acoustic Emission (AE) and Dynamic Identification (DI) were applied simultaneously in order to study the damage progress.

Two or three piezoelectric resonant AE sensors were applied on the specimens during all the tests in order to capture AE signals. The main features of these transducers, produced by Leane Net S.r.l. (Sarzana, Italy), are reported in Table 5.

Resonance frequency	160 kHz
Active element	Ceramic
Case material	Anodized Aluminium
Case shape	Circular: $d \times h = 50 \times 35$ mm
Weight	110 g

**Table 5:** Main characteristics of AE sensors

The connection between sensors and acquisition device was realized by coaxial cables (BNC female) to reduce the effects of electromagnetic noise (Lacidogna, Piana, Carpinteri, 2017). The data were acquired by an 8-channel national instruments digitizer, setting the acquisition threshold to 2 mV and adopting a sampling frequency of 1Msample/s. The registered signals were amplified of 60 dB before to be processed.

On the other hand, Dynamic Identification technique was applied only in Test\_100\_2 and in Test\_400\_3. Therefore, during these two tests the displacement of the hydraulic jack was monotonically increased with a constant velocity, but in a discontinuously way. In other words, these two tests were performed in several steps: the hydraulic jack was stopped in correspondence of different values of load or displacement, in order to apply impulsive forces on the specimen and capture in this way the free response signals. These latter were acquired by means of four piezoelectric pickups (piezo-ceramic buzzers): two positioned on the upper face of the specimen, the other two on the lower one. The adopted sensors are the JPR Plustone 400-403 disks, whose main characteristics are resumed in Table 6 (Lacidogna, Piana, Carpinteri, 2017).

External diameter	20 mm
Frequency range	0 to 20 kHz
Resonant frequency	6.0 ± 0.5 kHz
Operating temperature	-20 to +50 °C
Weight	1 g

Table 6: Main characteristics of piezoelectric pickups for the Dynamic Identification

The data were collected by an 8-channel Audiobox 1818VS1 acquisition device by PreSonus (Baton Rouge, LA, USA); the sampling frequency was set equal to 44.1 kHz.

## 2.2 Numerical (FEM) models

For each specimen sizes considered in the present thesis (Table 1), a Finite Element Model (FEM) was implemented in LUSAS software using plane stress elements.

The use of these models is related to three different purposes:

- i. to perform a modal analysis (linear elastic constitutive law) in order to obtain the first three natural bending frequencies of specimens on which Dynamic Identification technique was applied;
- ii. to perform a modal analysis of a fixed specimen, but with different notch depths, in order to evaluate numerically the decrease of natural frequencies with the increase of crack propagation, so that an inverse procedure can be performed using the experimental results obtained with the Dynamic Identification technique (see Section [1.3.1]);
- iii. to compare the experimental load-deflection curves with numerical ones, obtained by using a non-linear constitutive law of the material, and to evaluate numerically the stresses and the strains in the different steps considered in the non-linear analysis.

### 2.2.1 Numerical bending modes and related natural frequencies

Two Finite Element Models were implemented in LUSAS software in order to obtain the first three bending modes and related frequencies for the unloaded pre-notched beams on which Dynamic Identification technique was applied. They are the specimens used in Test\_100\_2 and in Test\_400\_3, respectively with a depth of 10 cm and 40 cm. These two models, with the relevant mesh, are represented in Figure 2.6 and in Figure 2.7.

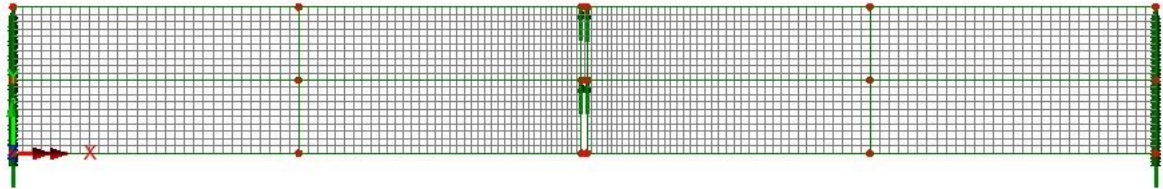


Figure 2.6: Finite Element Model used to perform the eigenvalue analysis for the 10 cm specimen

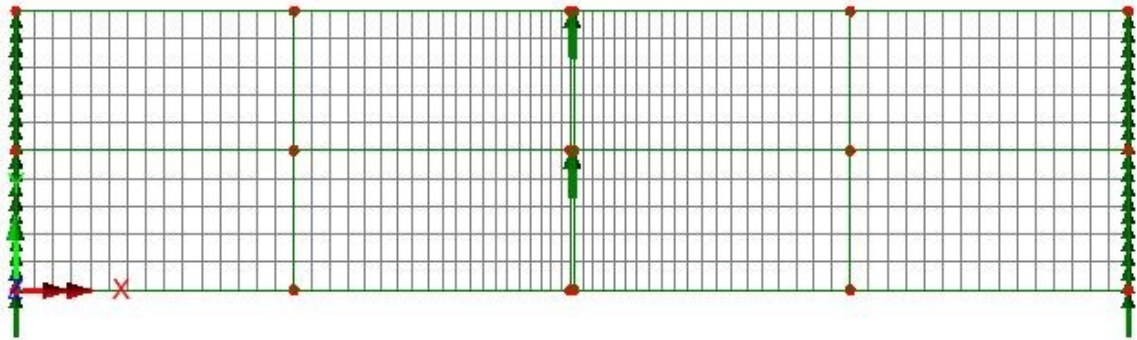


Figure 2.7: Finite Element Model used to perform the eigenvalue analysis for the 40 cm specimen

Quadrilateral plane stress elements were used: the QPM8 (Figure 2.8). This 2D isoparametric element with 8 nodes (quadratic element) belongs to the serendipity family. In the model of the 10 cm specimen, the ligament was vertically divided into 10 equal parts, in order to simply modify the model a sufficient number of times when the decrease of natural frequencies during the crack growth will be numerically evaluated (Section [2.2.2]); in the model of the largest specimen, instead, only 5 elements are vertically present along the ligament. Horizontally, in both cases the mesh becomes thicker near the notch. The constraint conditions concern only the vertical displacements: these are prevented on the two extremity faces and in correspondence of the mid-span section, where there is the third contact point during the TPB test.

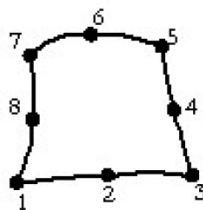


Figure 2.8: QPM8 element

The material is linear elastic (values of Young's modulus and mass density are in Table 4). An Eigenvalue Analysis was performed in order to obtain the first three bending modes and related natural frequencies. In Figure 2.9 e in Figure 2.10 the three modal shapes are represented for the unloaded specimens of 10 cm and 40 cm, respectively. The corresponding natural bending frequencies are reported in Table 7.

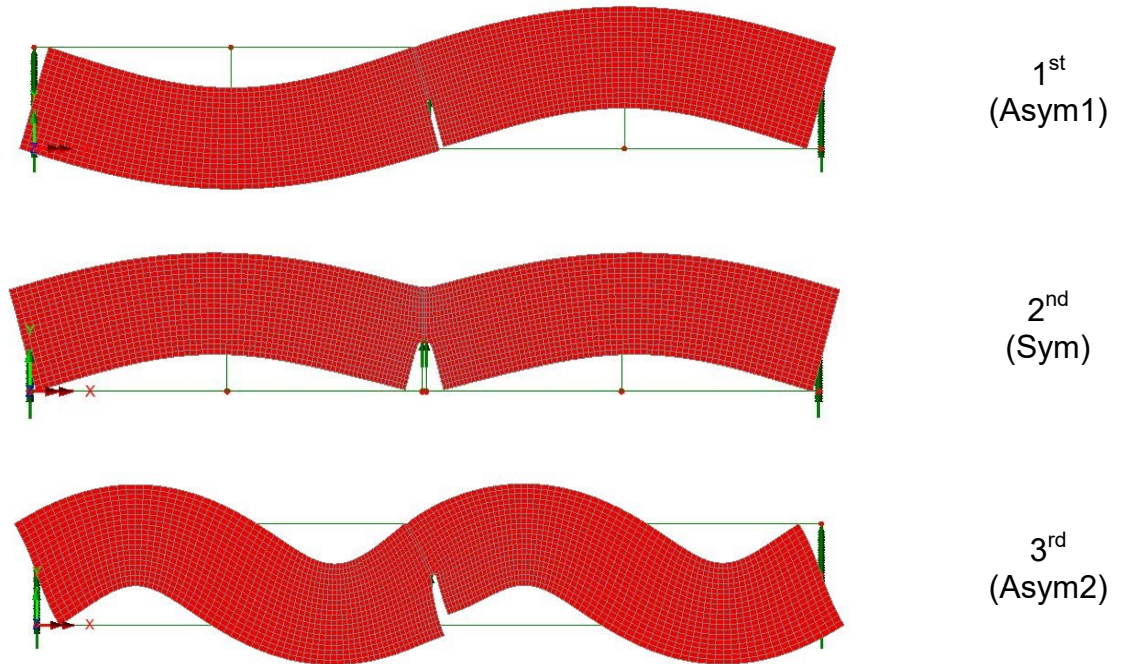
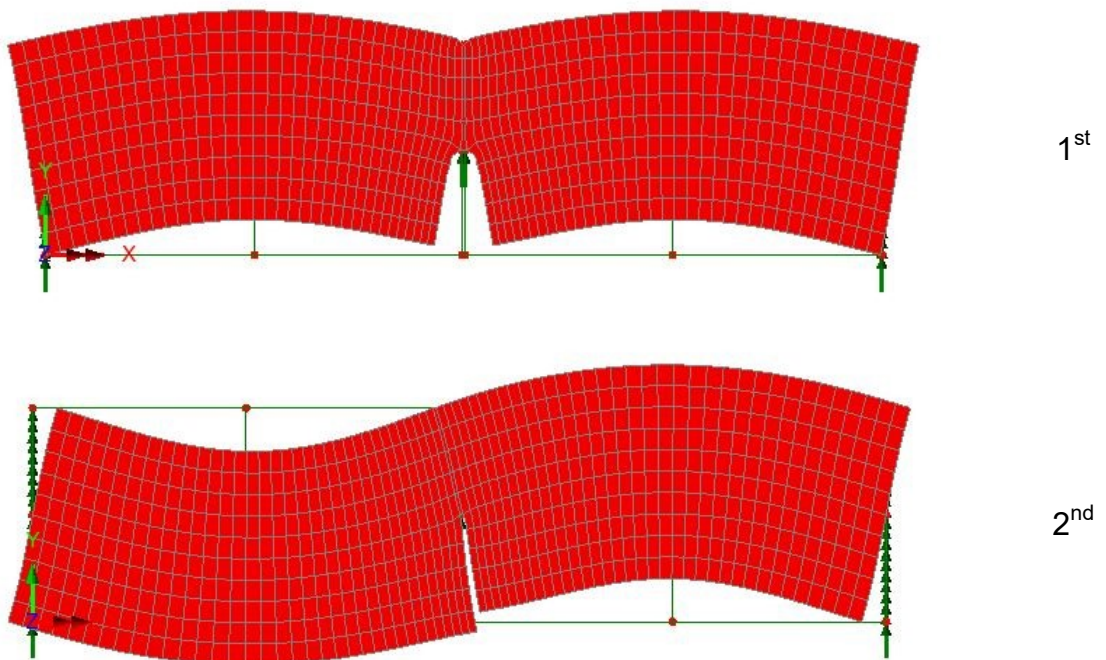


Figure 2.9: The first three bending modes for the 10 cm specimen



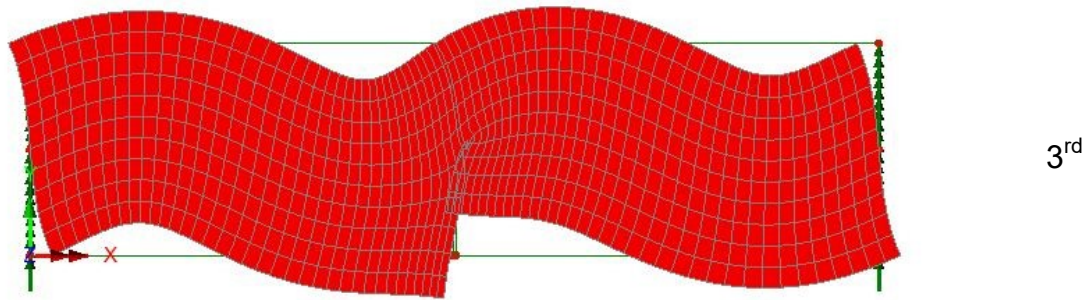


Figure 2.10: The first three bending modes for the 40 cm specimen

For what concerns the smaller specimen (Figure 2.9), the first and the third modal shapes are antisymmetric; on the contrary the third one is symmetric. In the case of the 40 cm specimen (Figure 2.10) the modal shapes are the same, but the first and the second result exchanged with respect to the previous case.

	10 cm specimen	40 cm specimen
1 <sup>st</sup> natural bending frequency [Hz]	992	741
2 <sup>nd</sup> natural bending frequency [Hz]	1102	774
3 <sup>rd</sup> natural bending frequency [Hz]	3263	2052

Table 7: The first three natural bending frequencies, numerically obtained (FEM), for the specimens with a depth of 10 cm and 40 cm

## 2.2.2 Numerical evaluation of the modal frequency variation during the crack growth

The Finite Element Model implemented for 10 cm specimen (Figure 2.6), described in the previous paragraph, was used also to evaluate numerically the variations of the first three natural bending frequencies following the crack propagation. To this purpose, the model was modified increasing the notch depth. In particular, ten different models were considered, each of them obtained eliminating one by one the 10 finite elements that divided the ligament in equal parts. For each of these models, the modal analysis implemented by LUSAS software was repeated. At the beginning of the test  $a/D = 0.5$  (initial notch). The last situation considered is  $a/D = 0.95$ , in which the adopted model has only one finite element along the uncracked ligament. The purpose of this analysis is to apply an inverse procedure in order to estimate the depth of the fracture during the test, using the values of the natural frequencies experimentally evaluated in the different loading steps.

Table 8 contains the values of the first three natural frequencies numerically evaluated by the ten models corresponding to different relative crack depths.

Figure 2.11 and Figure 2.12 show the modified models and the first three bending modal shapes in correspondence of a relative crack depth respectively equal to 0.75 and 0.95.

The decrease of the first three natural frequencies with the crack growth, experimentally determined and described in Table 8, is graphically represented in Figure 2.13.

It is important to note that, with the increase of the damage, the symmetric modal shape becomes the fundamental bending mode. For this reason, in Table 8 the natural frequencies are related to the correspondent modal shape denominated as in Figure 2.9.

		$a/D$									
		0.50	0.55	0.60	0.65	0.70	0.75	0.80	0.85	0.90	0.95
Modal shape	Asym1	992	991	989	986	983	979	975	969	962	951
	Sym	1102	1074	1046	1017	989	959	930	898	861	813
	Asym2	3263	3245	3222	3194	3159	3116	3062	2995	2908	2794

Table 8: The first three natural bending frequencies (1<sup>st</sup>: green; 2<sup>nd</sup>: blue; 3<sup>rd</sup> red) for the 10 cm specimen with different relative crack depths

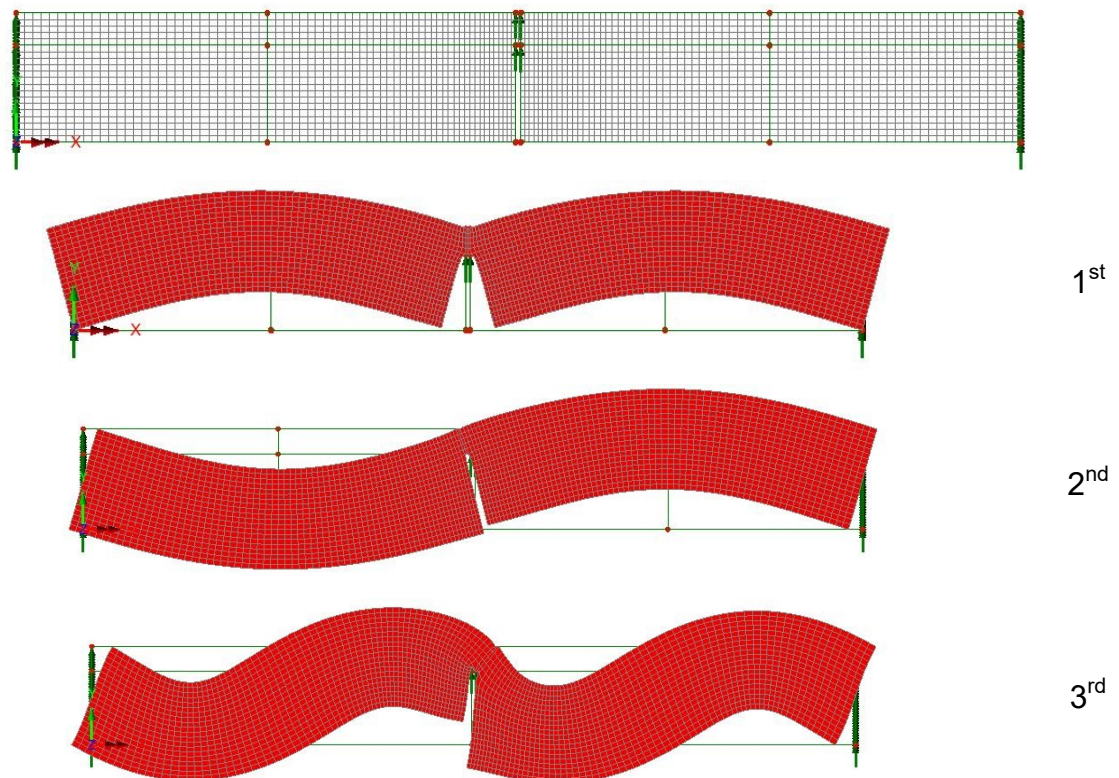


Figure 2.11: Finite Element Model and the first three bending modes related to a crack depth  $a/D = 0.75$

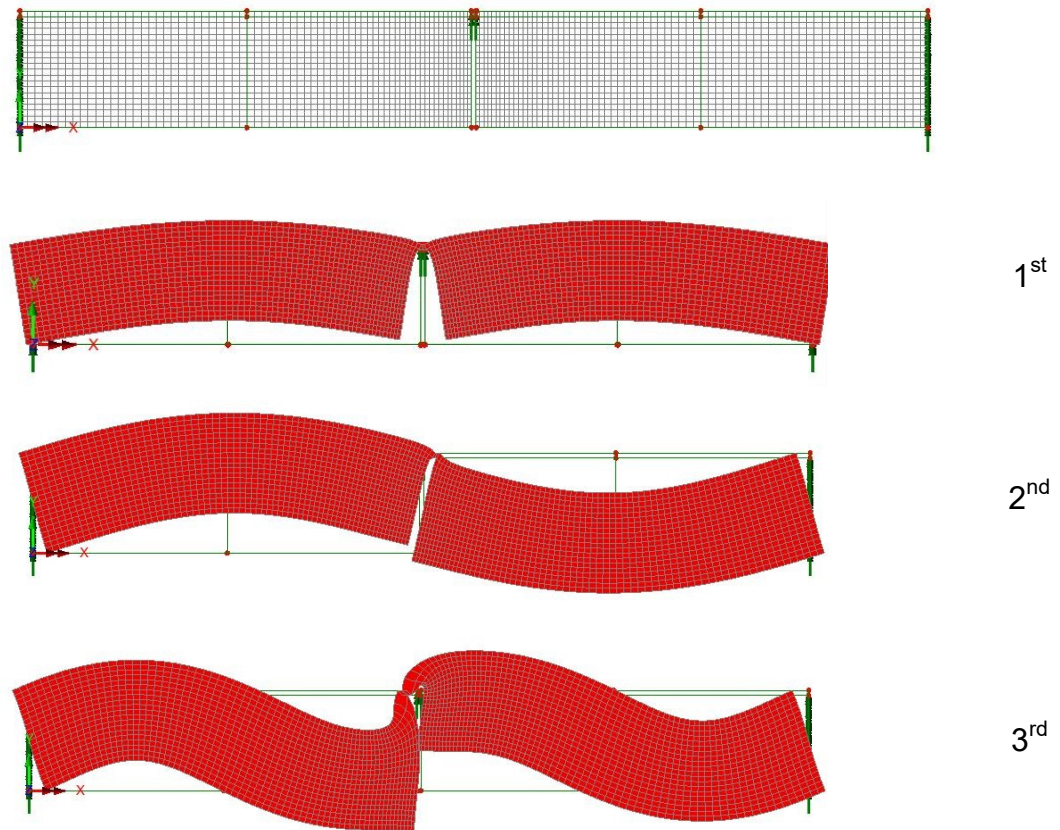


Figure 2.12: Finite Element Model and the first three bending modes related to a crack depth  $a/D = 0.95$

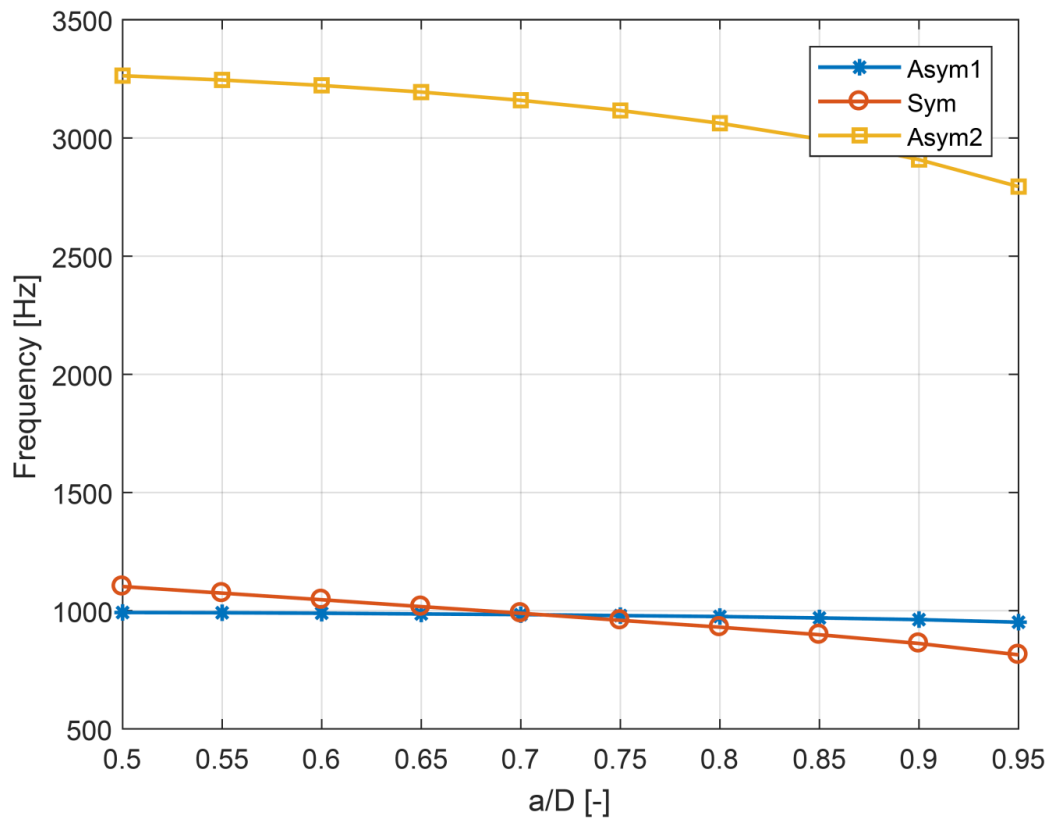


Figure 2.13: Decrease of the first three natural bending frequencies for the 10 cm specimen with the increasing of the relative crack depth  $a/D$

Table 9 shows the percentage decrease of the three natural frequencies due to a relative crack depth  $a/D = 0.95$  with respect to the initial configuration  $a/D = 0.50$ .

Modal shape	Decrease of natural frequency
Asym1	-4.1 %
Sym	-26.2 %
Asym2	-14.4 %

Table 9: Percentage decrease of the first three natural bending frequencies, for the 10 cm specimen, in correspondence of a relative crack depth  $a/D = 0.95$  with respect to the initial configuration

### 2.2.3 Numerical load-displacement curves

A non-linear Finite Element Model was implemented in LUSAS software for each specimen size described in Table 1 in order to obtain the load-deflection curve. The variation of stresses and strains along the uncracked ligament in the different loading steps was also investigated.

A non-linear constitutive law was used to describe the concrete behaviour. In particular, among the models available in the material library of LUSAS software, the *Smoothed Multi Crack Model* (or *Model 102*) was chosen (Figure 2.14); it takes into account the softening behaviour of concrete described in Section [1.1.1.2] and already represented in Figure 1.10.

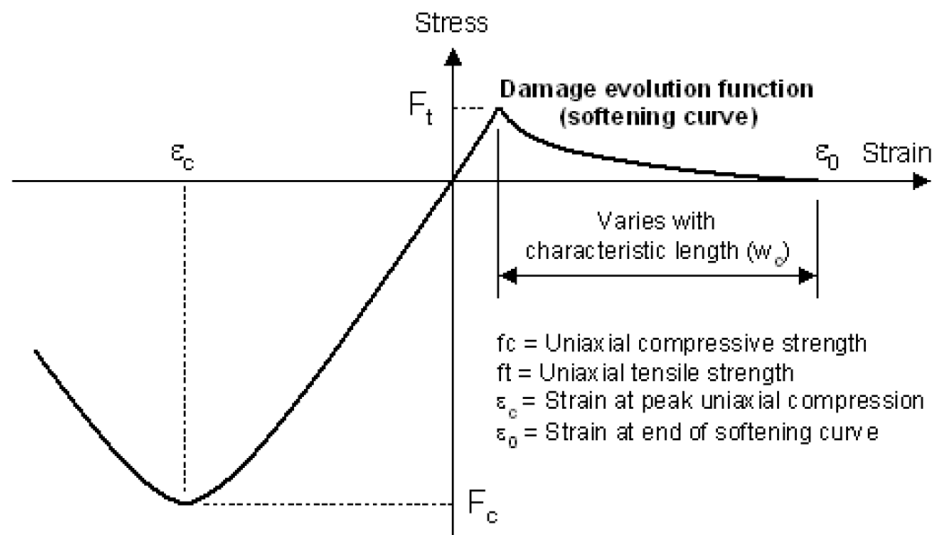


Figure 2.14: Constitutive law for concrete adopted in the numerical analysis (Model 102)

This constitutive law requires the values of the uniaxial compressive and tensile strengths (see Table 4), and the value of fracture energy. This latter was taken equal to the average of the values experimentally determined, for a certain specimen size, using the RILEM procedure; these values will be reported in the next section. In this

case triangular plane stress elements were used: the TPM3 (Figure 2.15). It is a 2D isoparametric element with 3 nodes (linear element). The ligament was vertically divided into equal parts, of 1 cm height each; for example in the model of 30 cm specimen, the ligament is divided in 15 equal parts. The mesh is refined near the notch. The constraint conditions concern only the vertical displacements: these are prevented only in the two extreme points. The “Nonlinear and Transient” analysis implemented in LUSAS software was used. An incremental vertical displacement (downwards) is imposed in correspondence of the mid-span section; the increment for each step of the analysis was set equal to 0.005 mm. Taking as an example the 30 cm specimen, Figure 2.16 shows the model and the mesh realised.

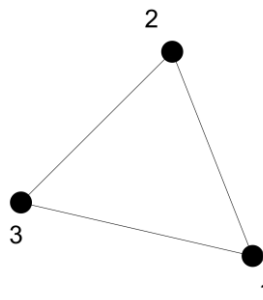


Figure 2.15: TPM3 element

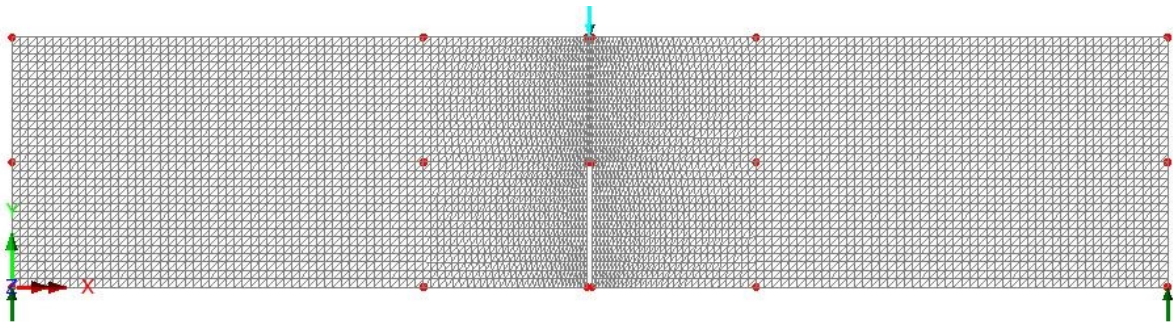


Figure 2.16: FEM of 30 cm specimen used to determine the numerical load-deflection curve

Considering only the 30 cm specimen as an example, in Figure 2.17 the deformed shape in correspondence of the peak load is shown, whereas Figure 2.18 shows the numerical load-displacement curve. In Section [2.3.1] it will be compared with the experimental one.

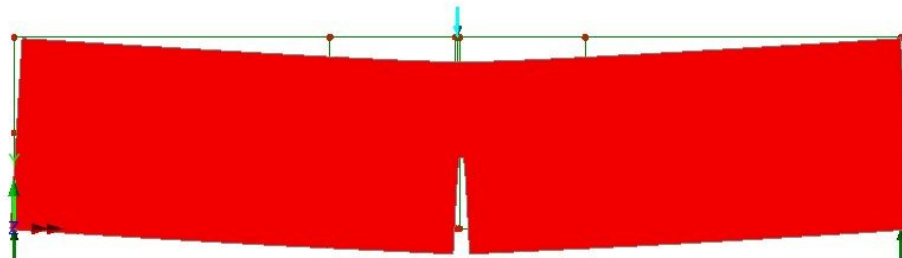


Figure 2.17: Deformed shape of the 30 cm specimen FEM in correspondence of the peak load

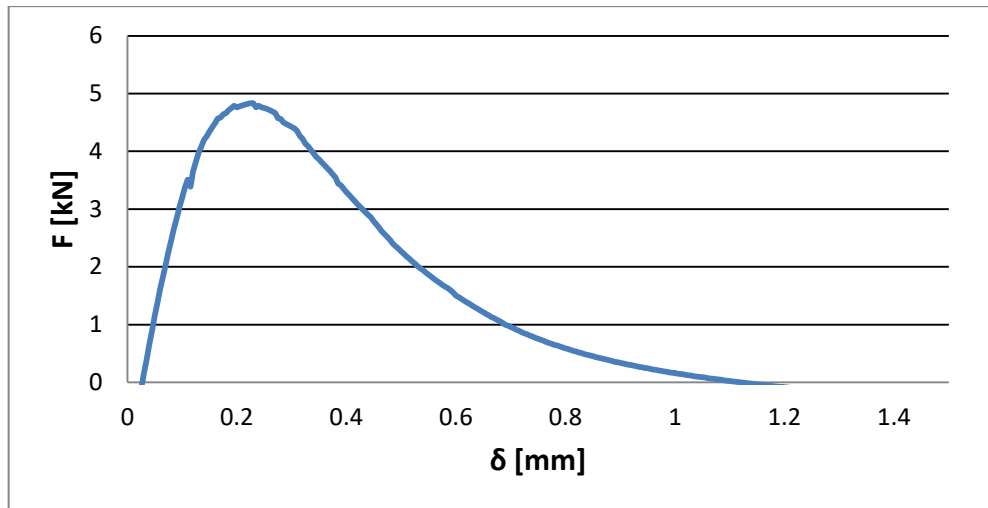
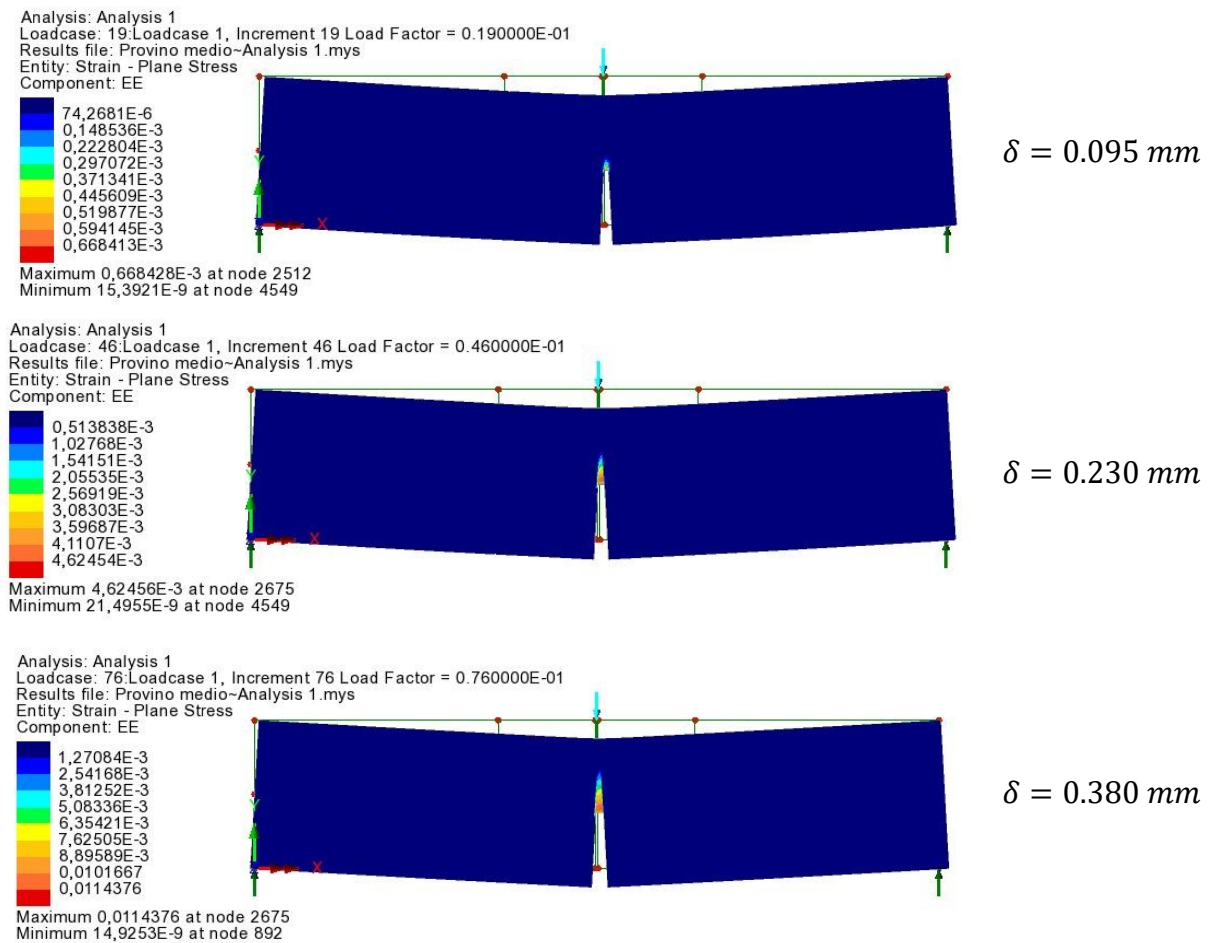
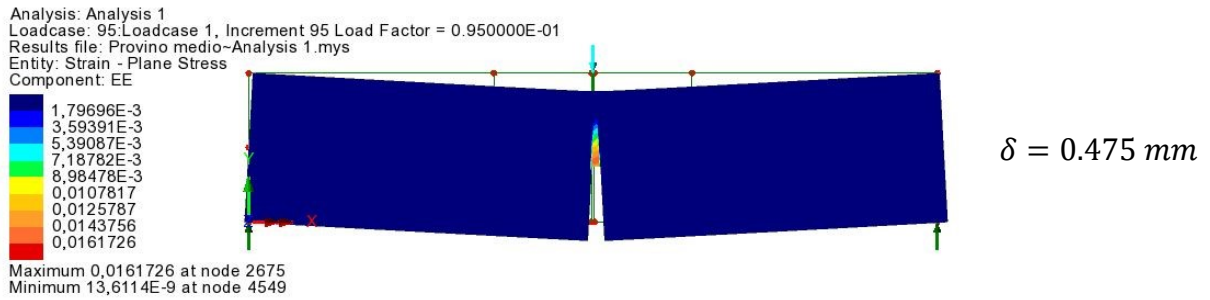


Figure 2.18: Numerical load-displacement curve for the 30 cm specimen

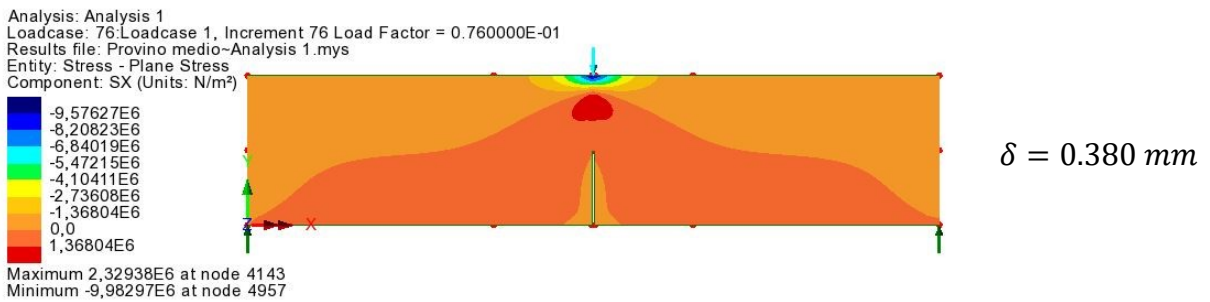
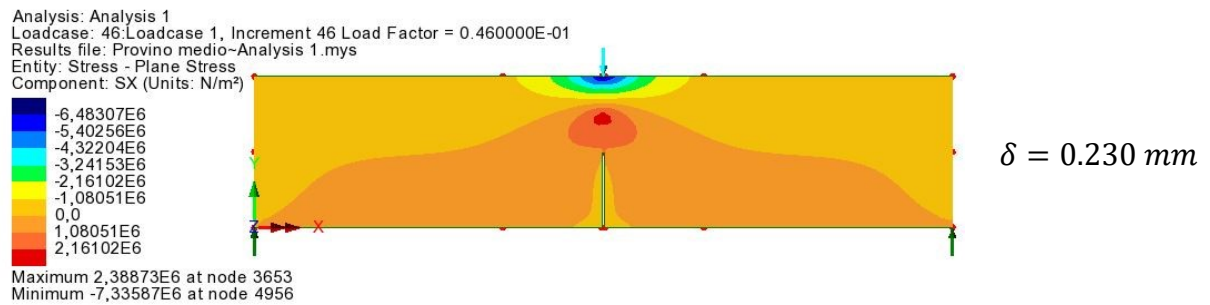
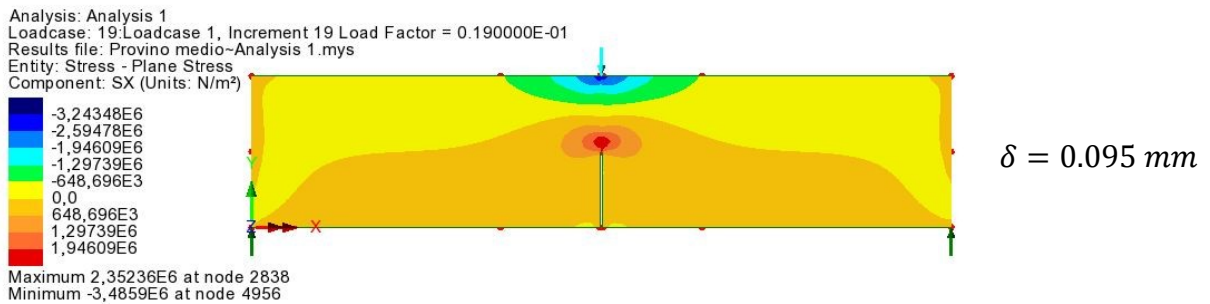
If the values of the strains are plotted using different colours, it is possible to underline the crack propagation in the different steps of the non-linear analysis. This is shown in Figure 2.19, where four different steps are considered, each of them corresponding to a certain point of the curve in Figure 2.18 and so to a certain value of displacement  $\delta$ .





**Figure 2.19: Strain values in the 30 cm specimen model with respect to four different steps of the analysis (crack propagation)**

As results of this non-linear analysis, it is possible to obtain also the stresses along the uncracked ligament, for example in the same steps considered in Figure 2.19. This is done in Figure 2.20, where the values of the longitudinal stresses are associated to different colours (negative stresses indicate compression, positive stresses indicate tension).



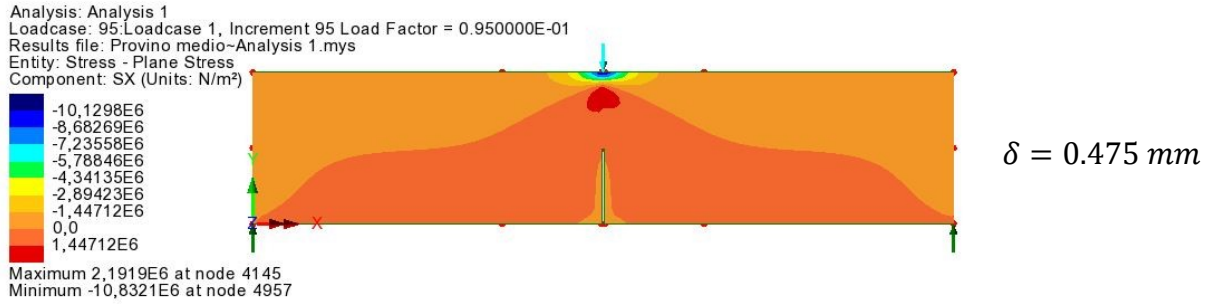


**Figure 2.20: Longitudinal stress values in the 30 cm specimen model with respect to four different steps of the analysis**

It is possible to represent in a diagram the values of the longitudinal stress in the different nodes of the mesh along the ligament, in correspondence of different steps of the analysis. In Figure 2.21 are considered again the previous four steps (coordinate zero in the diagram corresponds to the tip of the initial pre-notch).

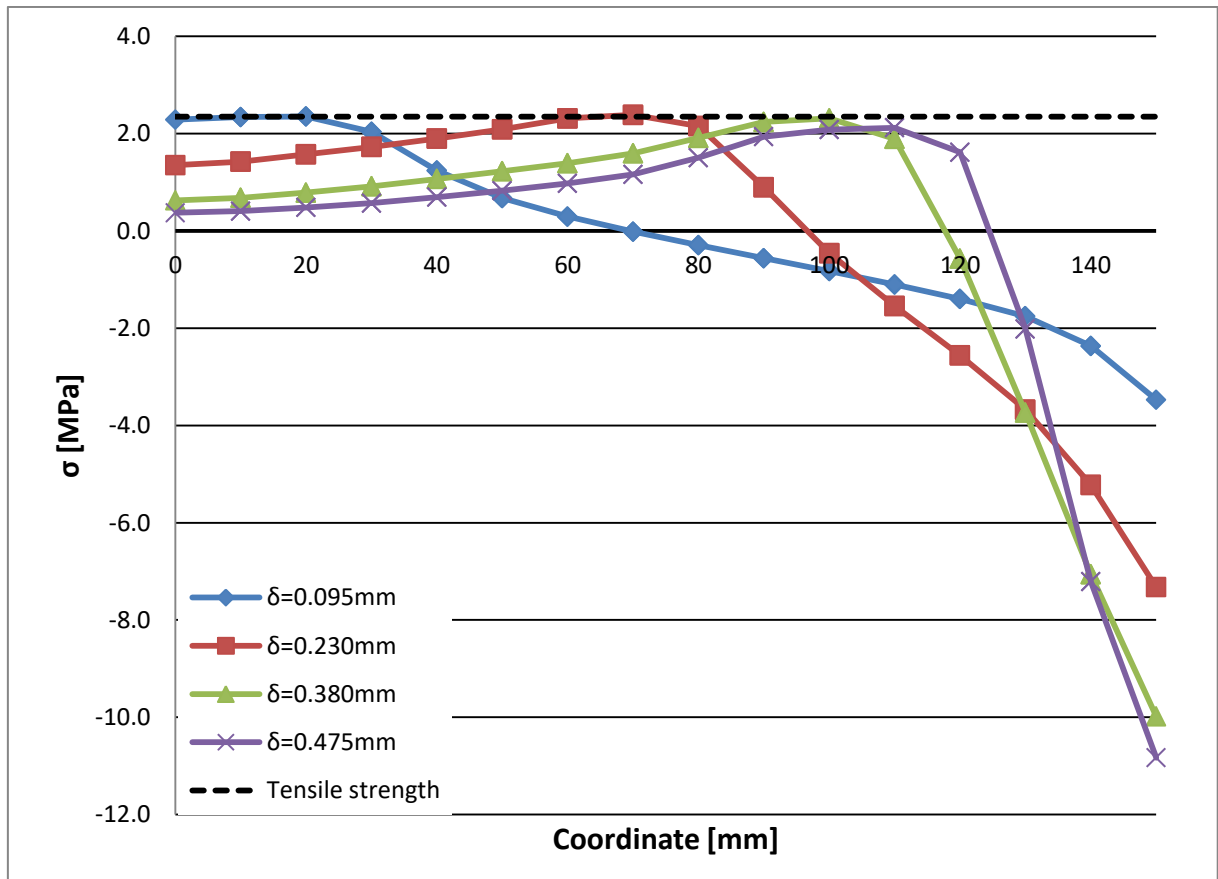


**Figure 2.21: Longitudinal stress in the nodes of the mesh along the ligament of the 30 cm specimen FEM in four different steps of the analysis**

Observing Figure 2.20 and Figure 2.21 it is possible to localize the crack tip in the different considered steps of the numerical analysis: it corresponds to the point in which the tensile stress reaches the material strength. In particular, the curve related to the pre-peak phase ( $\delta = 0.095 \text{ mm}$ ) is almost linear along the ligament (elastic distribution), while, after the peak load, the region subjected to tensile stresses lower than the material strength corresponds to the cracked ligament. Furthermore, it can be observed also how the compressive stresses in the extrados increase during the

simulation, because the reagent part of the ligament is getting smaller due to the crack growth.

### 2.3 A scale-independent fractal cohesive law for bending

In this section the experimental results will be presented. Particular attention will be reserved to bending strength and fracture energy. Scale effects on these two characteristics will be discussed, using the mono-fractal scaling laws. Furthermore, the load-deflection curves will be proposed in a renormalized form, and the energetic brittleness number will be calculated also using a generic definition with the renormalized values of fracture energy and bending strength. Finally, the kinematic aspect will be treated, taking into account the critical value of the rotation angle of the mid-span section in correspondence of the failure. Scale effects on this parameter will be interpreted again with a mono-fractal scaling law, and the relation concerning the three fractal exponents will be verified. A fractal cohesive law for bending, function of the three renormalized values of bending strength, fracture energy and critical rotation angle will be derived, likewise to what has already been done for uniaxial tensile tests (Carpinteri, Chiaia, Cornetti, 2002) and compression tests (Carpinteri, Corrado, 2009).

#### 2.3.1 Experimental results: Load-deflection curves

In Figure 2.22 the load-deflection curves obtained with the TPB tests described in Section [2.1.1.1] are superimposed in the same diagram. However the curves related to Test\_100\_2 and Test\_400\_3, in which Dynamic Identification technique was applied, are interpolating of the actual curves (Figure 2.23 and Figure 2.24). These latter present load drops, due to the fact that these tests were performed discontinuously: in order to apply impulsive forces on the specimen and to capture the free response signals, the test was stopped in correspondence of different displacement or load values. During these acquisitions, the hydraulic jack of the testing machine remained fixed, but the load decreased; when the test restarted, the load returned to its original value and then the test went on, up to the next step of acquisition.

Figure 2.22 shows a reduction in ductility in the behaviour of larger specimens. The peak-loads  $F_{max}$  are reported in Table 10. If the average tensile strength  $f_{ctm}$  of the material is considered (Table 4), it is possible to estimate a theoretical value of the peak load in order to be compared with the experimental one. This value of  $F_{max}$  can be calculated in two limit cases: supposing a linear elastic stress distribution (using Eq.(1.46) with  $W_{el}^{lig}$ ) or a perfectly plastic stress distribution (using Eq.(2.1) with  $W_{pl}^{lig}$ ):

$$\sigma_u = \frac{M_{tot}}{W_{pl}^{lig}} = \frac{\left(F_{max} + \frac{m \cdot g}{2}\right) \cdot \frac{S}{4}}{\frac{B \cdot (D - a)^2}{4}} \quad (2.1)$$

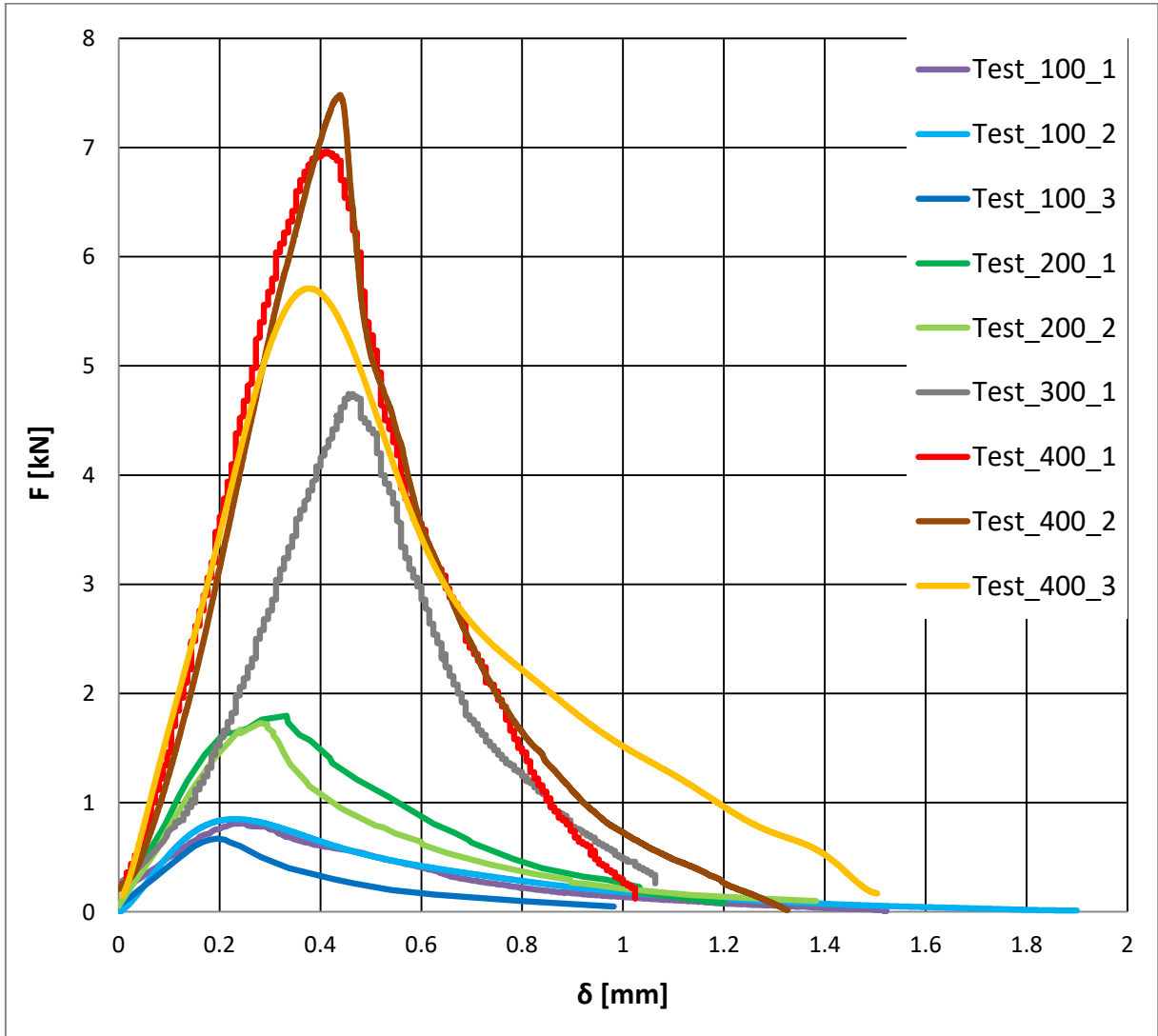


Figure 2.22: Load-deflection curves experimentally obtained with three point bending tests

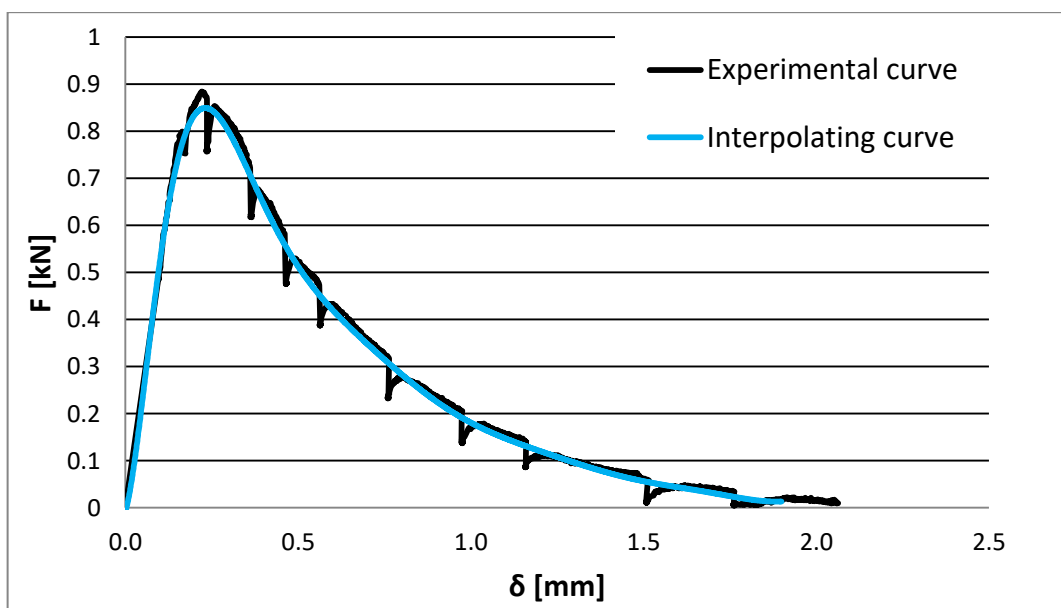


Figure 2.23: Experimental and interpolating curve for Test\_100\_2

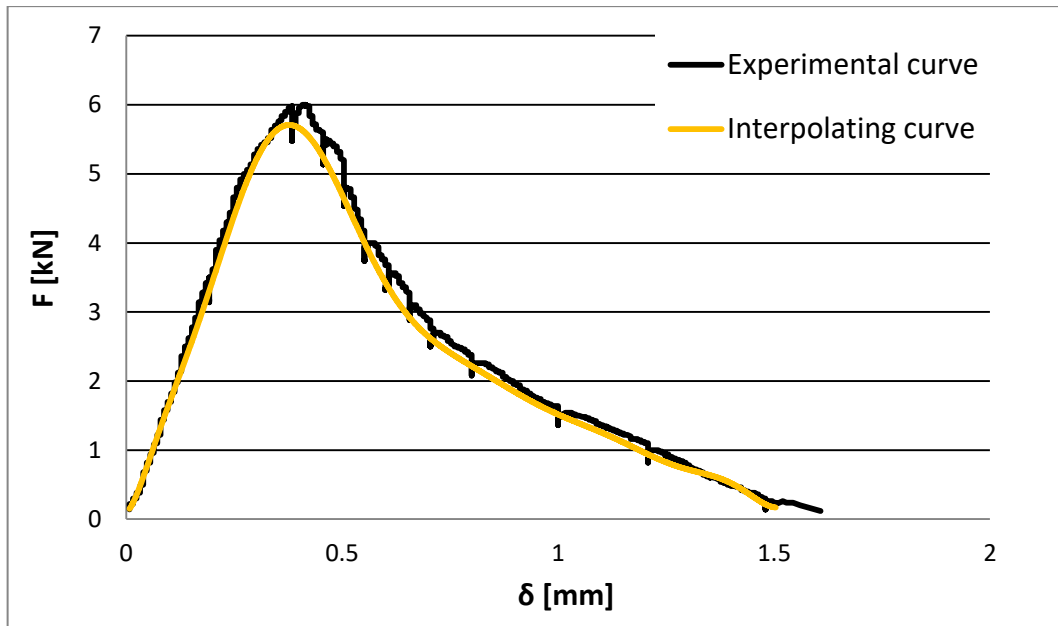


Figure 2.24: Experimental and interpolating curve for Test\_400\_3

	$F_{max}^{experimental}$ [kN]	$F_{max}^{theoretical} (W_{el}^{lig})$ [kN]	$F_{max}^{theoretical} (W_{pl}^{lig})$ [kN]
Test_100_1	0.81	0.40	0.64
Test_100_2	0.88		
Test_100_3	0.67		
Test_200_1	1.79	1.12	1.80
Test_200_2	1.73		
Test_300_1	4.74	3.11	5.02
Test_400_1	6.96	6.38	10.30
Test_400_2	7.48		
Test_400_3	6.00		

Table 10: Experimental peak-loads for the different tests, compared with the theoretical values related to the elastic and the plastic stress distribution on the ligament

Table 10 shows that the real peak loads for the specimens with depths 10, 20 and 30 cm, are closer to the theoretical values calculated with  $W_{pl}^{lig}$ , whereas the specimens with a depth of 40 cm have reached peak-loads that are closer to the values obtained supposing a linear elastic stress distribution along the ligament. This observation underlines how a brittle behaviour of the larger specimens is present.

For each test it is possible to evaluate, following the RILEM Recommendation described in Section [1.1.1.4], the fracture energy and the bending strength, using respectively Eq.(1.45) and Eq.(1.46). The values obtained are shown in Table 11.

	$\sigma_u$ [MPa]	$G_F$ [N/m]
Test_100_1	4.33	150.6
Test_100_2	4.68	/
Test_100_3	3.65	118.0
Test_200_1	3.51	173.0
Test_200_2	3.40	154.0
Test_300_1	3.35	160.2
Test_400_1	2.52	153.2
Test_400_2	2.68	177.8
Test_400_3	2.24	/

Table 11: Experimental values of fracture energy and bending strength

Test\_100\_2 and Test\_400\_3 cannot be used to determine the fracture energy, because these tests, in which Dynamic Identification technique was applied, were performed in a discontinuous way, not in agreement with the RILEM Recommendation.

Table 11 shows clearly the scale effects on bending strength and fracture energy. These will be interpreted with the mono-fractal scaling laws in the next paragraphs.

Furthermore, the behaviour of the specimens can be described by the energy brittleness number (Eq.(1.27)). The values of this parameter are represented, for each test (except for Test\_100\_2 and Test\_400\_3), in Figure 2.25.

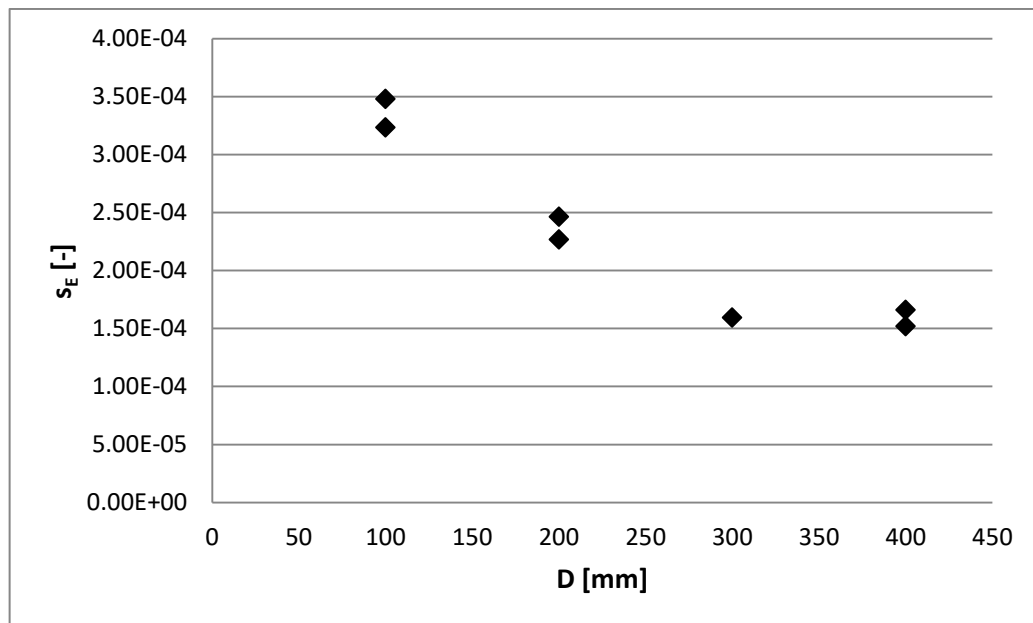


Figure 2.25: Values of the energy brittleness number ( $s_E$ ) for each TPB test

Considering the energy brittleness number for each test, the brittle behaviour of the larger specimens is highlighted.

One last consideration concerns the numerical (FEM) load-deflection curves discussed in Section [2.2.3]. They can be compared with the experimental curves represented in Figure 2.22.

Figure 2.26 shows, for example, this comparison with respect to the 10 cm specimens (Test\_100\_1 and Test\_100\_2).

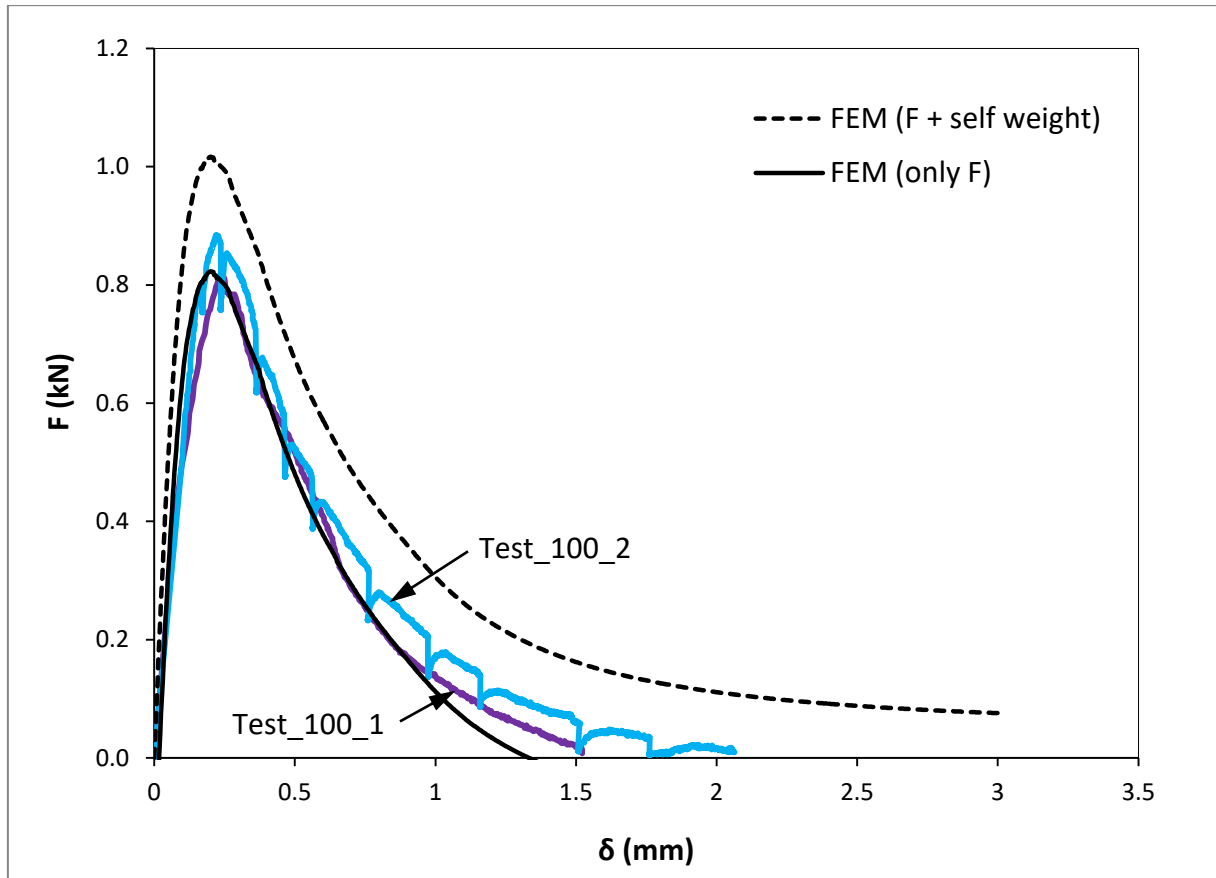


Figure 2.26: Comparison between the experimental and the numerical (FEM) load-deflection curves for the 10 cm specimens (Test\_100\_1, Test\_100\_2)

A good superimposition between experimental and numerical curves is found. In Figure 2.26 the numerical curve obtained considering the effect of self-weight is also represented.

### 2.3.2 Scale effects on bending strength

The values of bending strength determined in each TPB test are reported in Table 11. They can be graphically represented in a bilogarithmic diagram, in which the horizontal axis contains the logarithms of the specimen depths. The mono-fractal scaling law, described in Section [1.1.2.2], was used to fit the experimental results. In a bilogarithmic diagram this law is represented by a straight line (Eq.(1.67)), whose equation provides the values of the renormalized (scale-independent) bending strength  $\sigma_u^*$  and the exponent  $d_\sigma$ . It is represented in Figure 2.27.

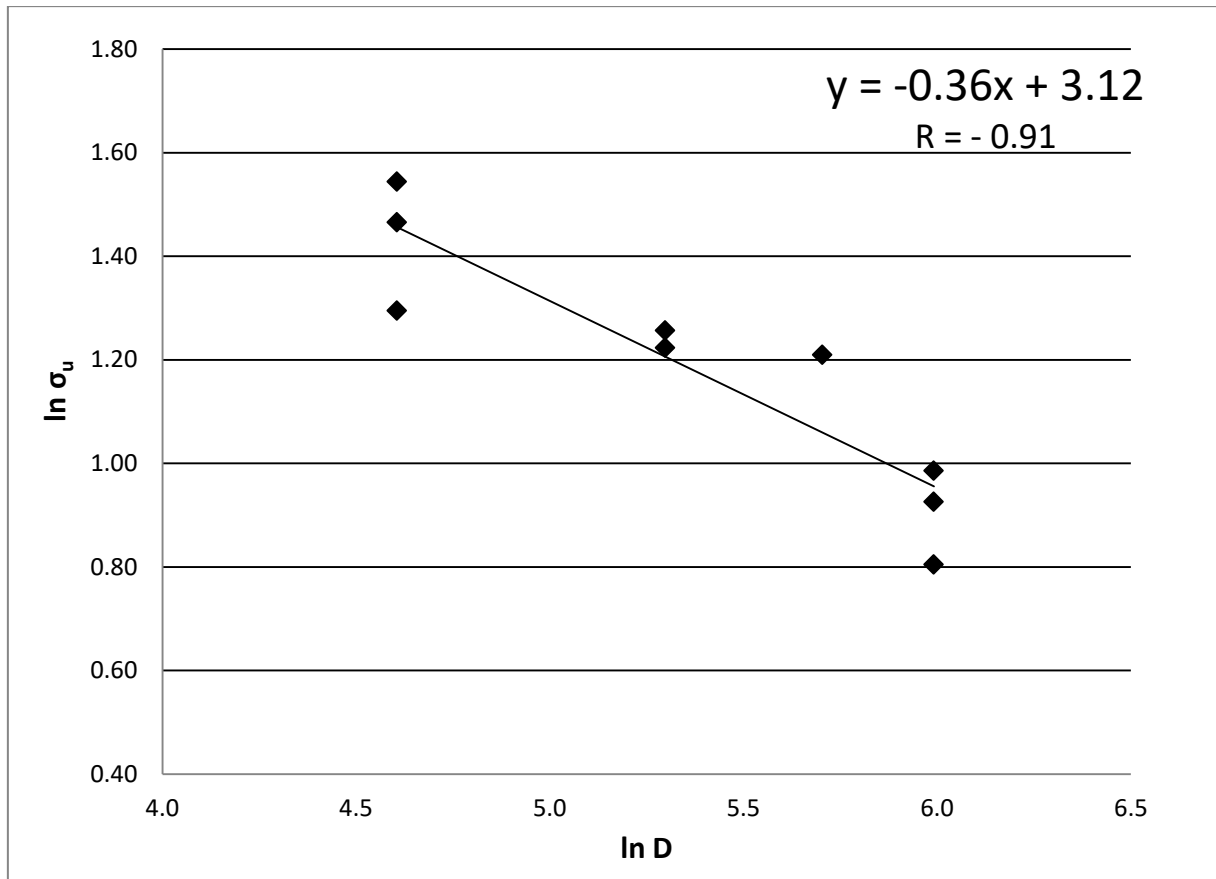


Figure 2.27: Scale effects on bending strength: mono-fractal scaling law

The best fitting procedure using the mono-fractal scaling law described in Section [1.1.2.2] provides a fractal exponent  $d_\sigma = 0.36$ . Hence, the ligament results to be a fractal domain with a dimension 1.64. In the diagram of Figure 2.27 is also introduced the value of  $R$ , that is the Pearson correlation coefficient. It is a measure of the linear correlation between two variables (in this case the logarithms of the specimen depth and of the experimental bending strength) and it is defined as the covariance of the two variables divided by the product of their standard deviations. This coefficient assumes values between -1 and +1, where 1 is the total positive linear correlation, 0 is no linear correlation, and -1 is total negative linear correlation. In Figure 2.27 it is equal to 0.91: it means that the mono-fractal scaling law is suitable to describe the scale effects experimentally observed.

Considering again Eq.(1.67), it is possible to calculate for each test the value of  $\ln \sigma_u^*$  in the following way:

$$\ln \sigma_u^* = \ln \sigma_u + d_\sigma \cdot \ln D \quad (2.2)$$

These values are represented in Figure 2.28. They are almost constant. Through a linear regression, that presents in fact a slope practically equal to zero, the value of the renormalized bending strength can be derived: it is  $\sigma_u^* = 22.6 \text{ N} \cdot \text{mm}^{-1.64}$ .

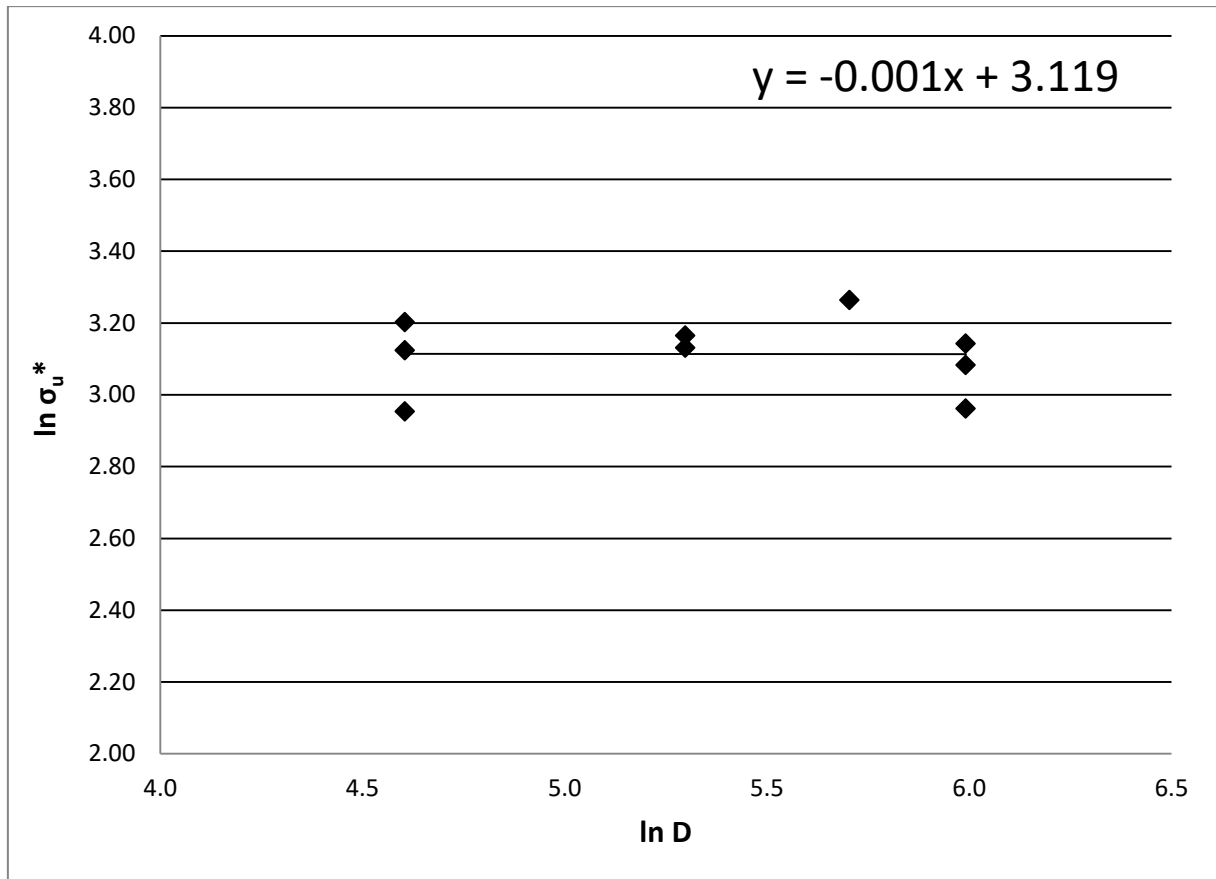


Figure 2.28: Renormalized bending strength

With respect to the results related to uniaxial tensile test (Carpinteri, Ferro, 1994) presented in Section [1.1.2.2], in this case, concerning three point bending tests, a larger value of  $d_\sigma$  is obtained. A possible explanation of this result concerns the stress distribution on the specimen cross-section: while in uniaxial tensile test the whole section bears the tensile forces, in TPB test, conversely, there is also a part of the ligament subjected to compression stresses.

### 2.3.3 Scale effects on fracture energy

As seen in Section [1.1.2.2], another power law can be used for the scale effects on fracture energy. If the experimental results concerning this parameter (presented in Table 11) are represented in a bilogarithmic diagram (Figure 2.29), this law will be a straight line described by Eq.(1.64). With a best fitting procedure, the value of the fractal exponent  $d_G$  can be determined. It results  $d_G = 0.19$ . This means that the energy dissipation occurs in a fractal space of dimension 2.19. Starting from Eq.(1.64), it is possible to determine, for each test, the value of  $\ln G_F^*$  as follows:

$$\ln G_F^* = \ln G_F - d_G \cdot \ln D \quad (2.3)$$

Also in this case these values, for the different tests, are almost constant, and the straight line that is used in Figure 2.30 to fit the experimental results is practically horizontal. It provides the renormalized (scale independent) value of the fracture energy, that represents the real material property: it results  $G_F^* = 209.9 \text{ J} \cdot \text{m}^{-2.19}$ .

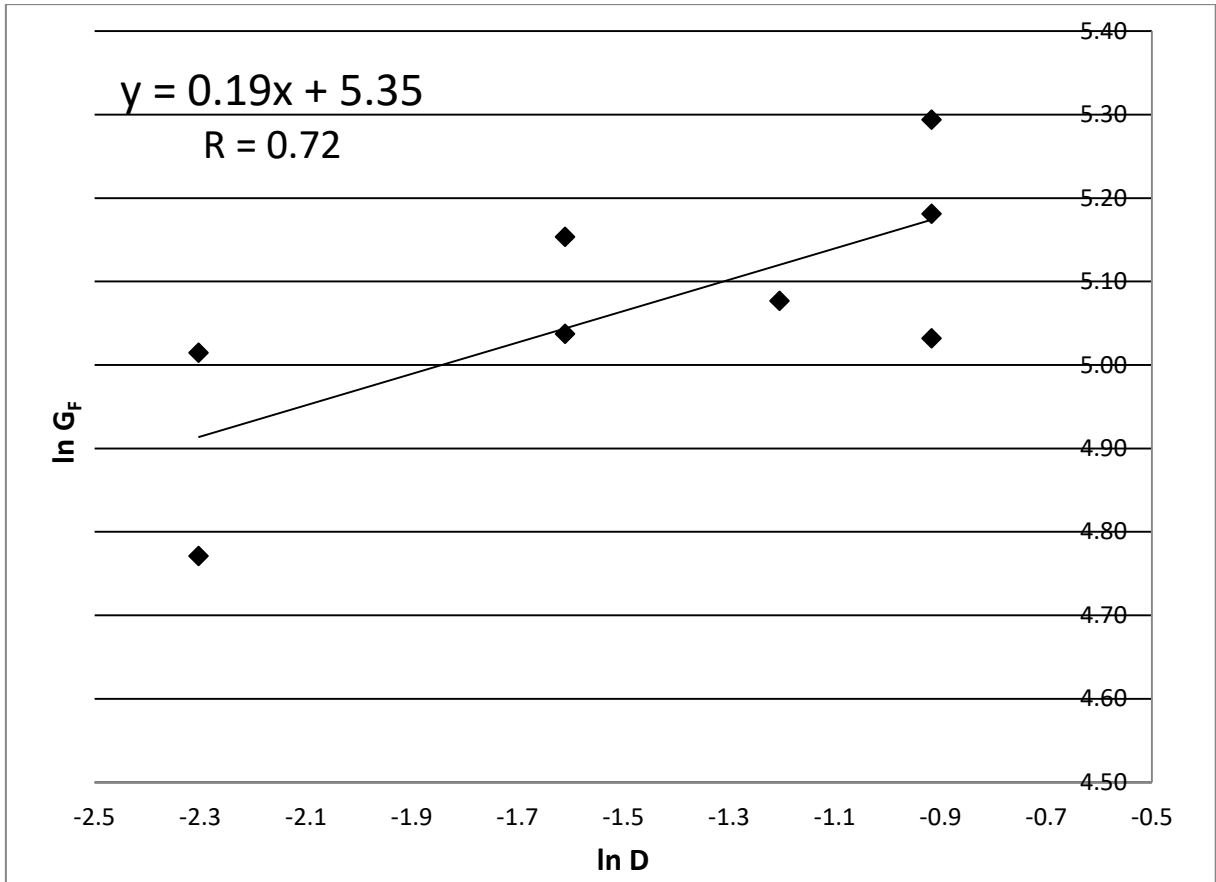


Figure 2.29: Scale effects on fracture energy: mono-fractal scaling law

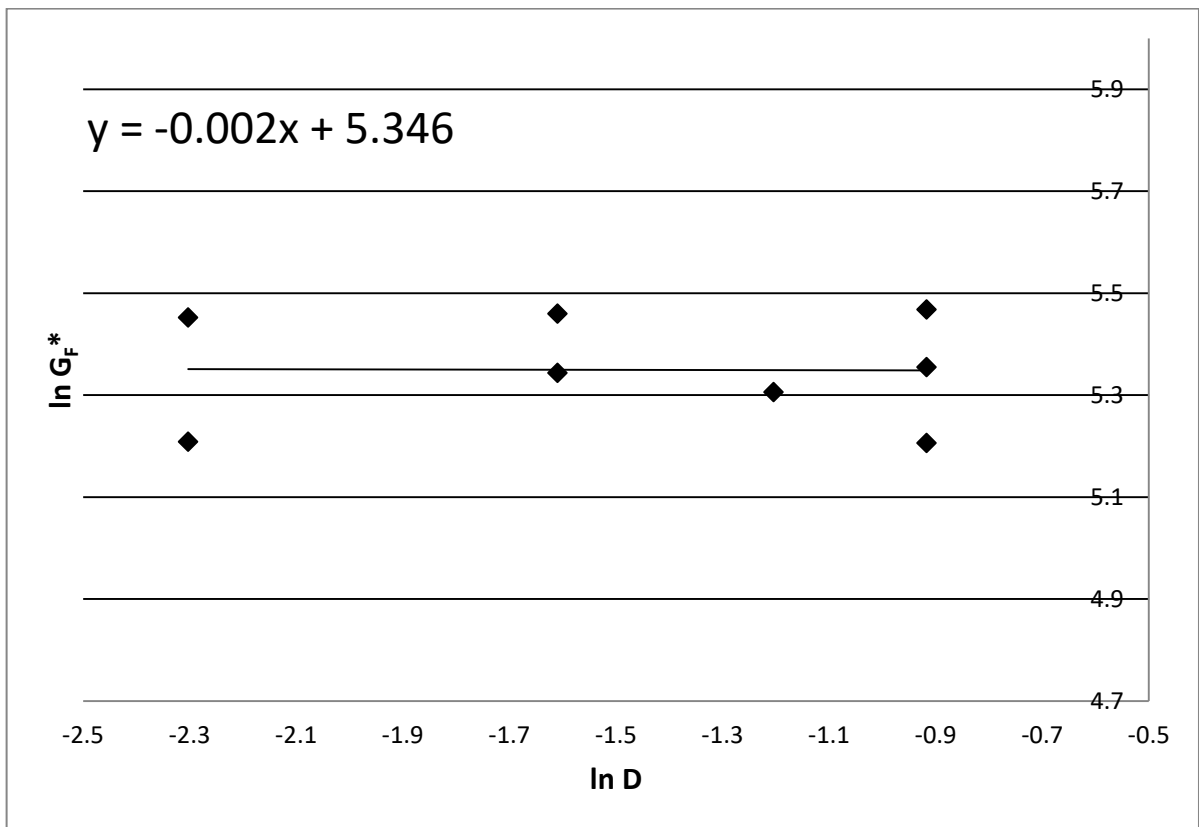


Figure 2.30: Renormalized fracture energy

### 2.3.4 Renormalized load-deflection curves

In Figure 2.22 the load-deflection curves obtained experimentally during TPB tests were superimposed. The remarkable dispersion between the different curves, due to the scale effects, can be minimized by operating a correct renormalization of these curves (Carpinteri, Ferro, 1998). In order to express in dimensionless form the quantities on the two axis of Figure 2.22, it is necessary to use the renormalized bending strength  $\sigma_u^*$  determined in Section [2.3.2], and the characteristic size  $D$  of specimens rescaled by the fractal dimension of the ligament at the peak load. In particular, the dimensionless values of the load will be:

$$\tilde{F} = \frac{F}{\sigma_u^* \cdot B \cdot D^{0.64}} \quad (2.4)$$

$B$  and  $D$  are respectively the width and the depth of the specimen. On the other hand, the dimensionless values of the displacements  $\delta$  will be evaluated dividing by the rescaled characteristic dimension:

$$\tilde{\delta} = \frac{\delta}{D^{0.64}} \quad (2.5)$$

The renormalized load-deflection curves obtained (excluding those related to the tests in which Dynamic Identification technique was applied) are represented in Figure 2.31.

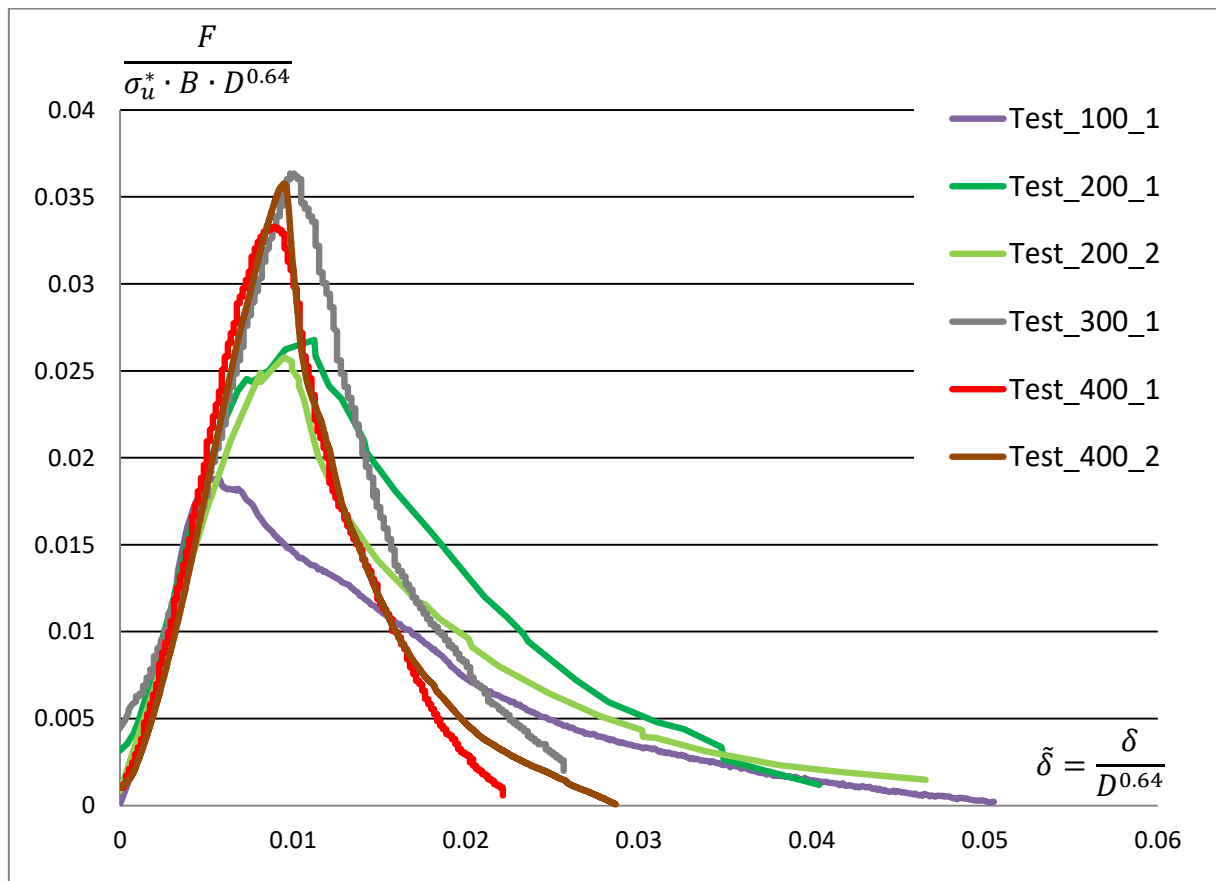


Figure 2.31: Renormalized load-deflection curves

In the elastic branch, when isolated micro-cracks are forming, the curves overlap almost perfectly, because in this phase the fractal dimension of the ligament is exactly the one obtained in Figure 2.27 through the renormalization procedure. On the other hand, the softening branches of the different curves still exhibit considerable differences. This happens because during that phase a macro-crack propagates, and this causes a decrease of the fractal dimension of the material ligament, until it becomes zero in correspondence of the complete failure and two-part separation. In order to obtain a complete overlap also of the softening branches, it would be necessary to use not a constant but a variable fractal exponent to renormalize the curves (Carpinteri, Ferro, 1998). In other words, the mono-fractality hypothesis is not suitable for the softening phase.

One last consideration concerns the generalization of the energy brittleness number ( $s_E^*$ ), expressed by Eq.(1.69). Using the fractal exponents and the renormalized values of bending strength and fracture energy, it can be evaluated for the different specimen sizes in order to give a measure of their brittleness (Figure 2.32).

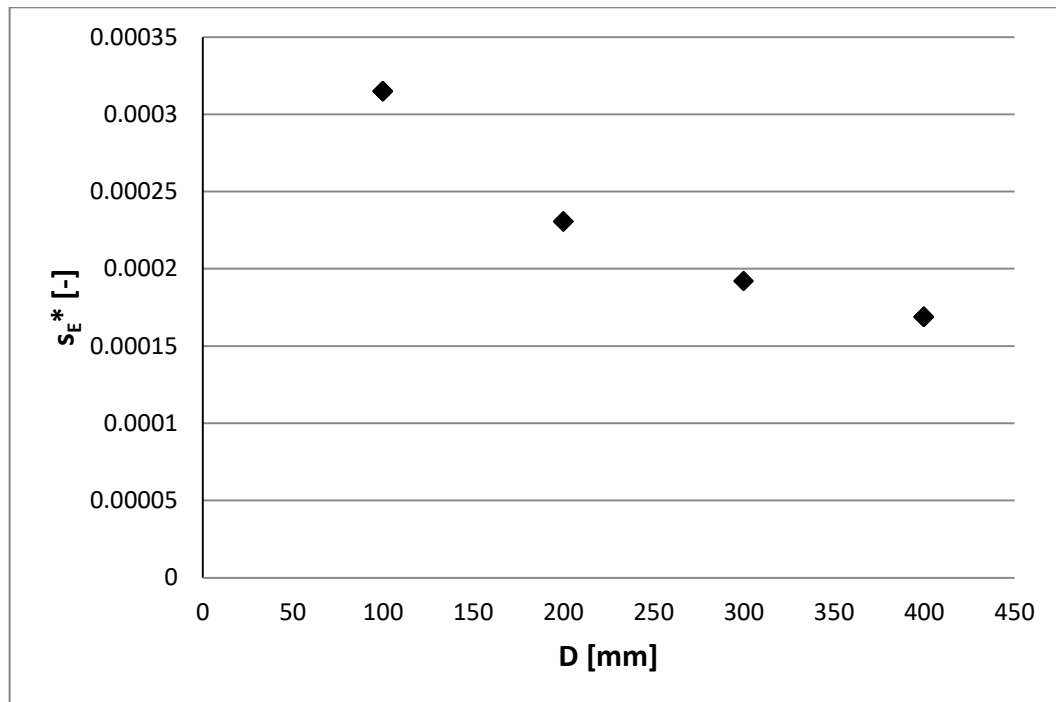


Figure 2.32: Generalization of the energy brittleness number ( $s_E^*$ )

### 2.3.5 Scale effects on the critical rotation angle: Kinematic aspects

Fracture energy, tensile strength and critical displacement are the three parameters that characterize the classical cohesive law described in Section [1.1.1.2] (Figure 1.9b). They are considered as material properties. However experimentally evidences, such as the results discussed in the present thesis (Sections [2.3.2] and [2.3.3]), have shown their scale dependence. Furthermore, also the kinematic parameter, such as the critical displacement  $w_c$ , is affected by the scale problem. This was observed, for example, by Carpinteri, Chiaia, Cornetti (2002), that analysed

the results of uniaxial tensile tests, performed by Carpinteri and Ferro (1994). They determined the cohesive laws for the different specimen sizes (the curves represented in Figure 1.30b) and observed that the critical displacement  $w_c$  increases with the specimen size. Consequently, it is necessary to introduce also a fractal kinematical quantity that, in the case of uniaxial tensile tests, was represented by the fractal critical strain  $\varepsilon_c^*$ . Nevertheless, in case of three point bending tests, it is difficult to use the longitudinal strain, because it varies along the ligament; moreover also the curvature  $\chi$  is not suitable to describe the damage process in a TPB test, because it will present a discontinuity in correspondence of the cracked section. For these reasons, the kinematic parameter that was chosen in the present thesis to describe the critical situation in TPB tests is the rotation angle of the mid-span section. In order to evaluate the critical value of this angle, i.e. its value in correspondence of the final failure, when the applied load is zero and  $\delta = \delta_0$  (see Figure 1.20 for the meaning of  $\delta_0$ ), simply geometric considerations were used, based on the scheme in Figure 2.33.

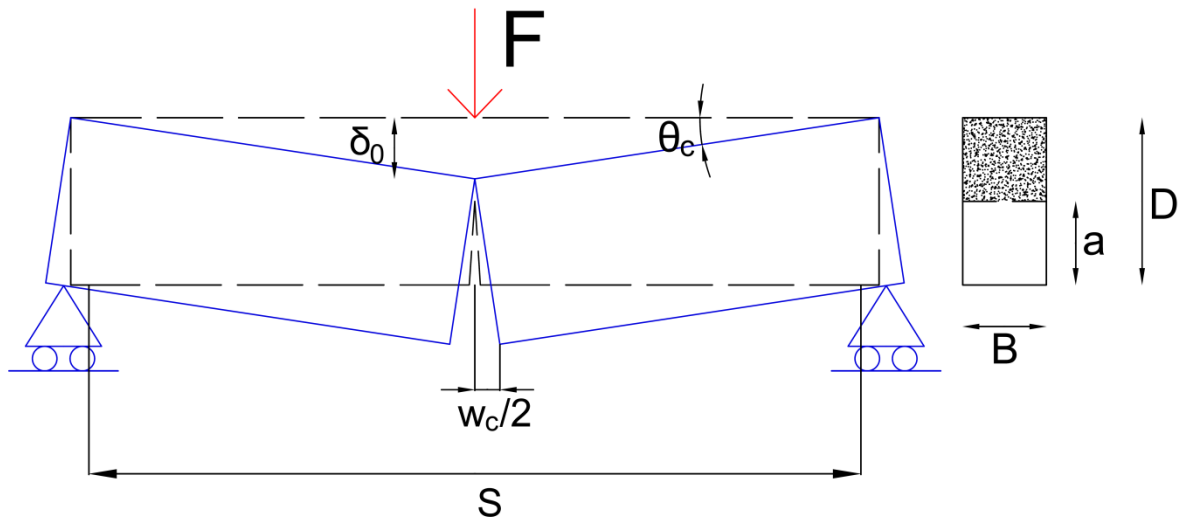


Figure 2.33: Limit situation of final failure in a TPB test

The rotation angle can be simply evaluated, in a generic instant of the test, as:

$$\tan \theta = \frac{\delta}{S/2} \quad (2.6)$$

In correspondence of the final failure (limit situation represented in Figure 2.33), Eq.(2.6) can be rewritten in critical terms:

$$\tan \theta_c = \frac{\delta_0}{S/2} \quad (2.7)$$

The critical rotation angle  $\theta_c$  can be substituted with its tangent:

$$\theta_c \cong \frac{\delta_0}{S/2} \quad (2.8)$$

On the other hand, the crack opening displacement  $w$ , in a generic instant of the test, can be evaluated as:

$$\frac{w}{2} = \bar{w} = D \cdot \sin \theta \cong D \cdot \theta \quad (2.9)$$

where  $\sin \theta$  can be substituted with the angle value because it is small enough. Eq.(2.9) can be rewritten in critical terms:

$$\bar{w}_c \cong D \cdot \theta_c \quad (2.10)$$

Using Eq.(2.8), it is possible to evaluate the critical value of the rotation angle for each TPB test. These values are graphically represented in Figure 2.34 in a bilogarithmic diagram.

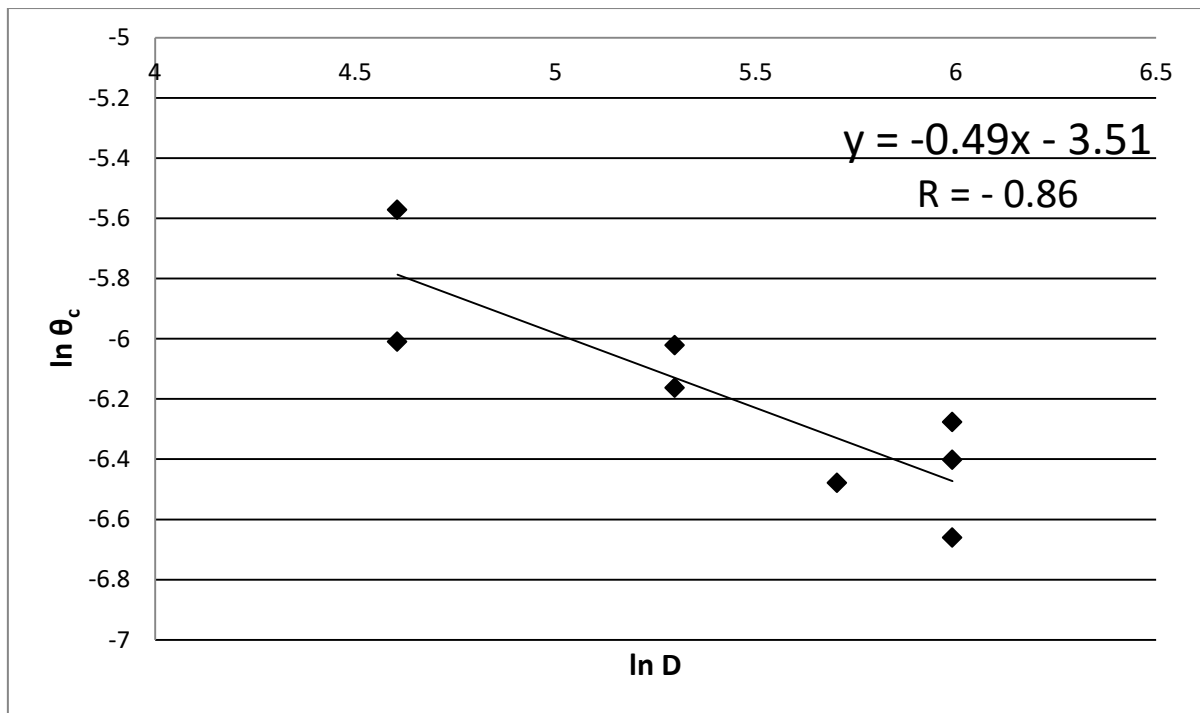


Figure 2.34: Scale effects on the critical value of rotation angle

A power law, similar to Eq.(1.71) used for the critical strain in uniaxial tensile tests, is now proposed to describe the scale effects on the critical value of the kinematic parameter concerning TPB tests:

$$\theta_c = \theta_c^* \cdot D^{-d_\theta} \quad (2.11)$$

Eq.(2.11) represents the mono-fractal scaling law for the critical rotation angle.  $\theta_c^*$  is the renormalized value of the critical rotation angle, i.e. the true material constant. It is not a dimensionless value, but it has a non-integer physical dimension  $[L]^{d_\theta}$ .  $d_\theta$  is the fractal exponent concerning the kinematic aspect of the TPB problem (it is the equivalent of  $d_\varepsilon$  discussed in Section [1.1.2.2] for uniaxial tensile tests). Eq.(2.11) can be rewritten in a logarithmic form:

$$\ln \theta_c = \ln \theta_c^* - d_\theta \cdot \ln D \quad (2.12)$$

From the equation of the linear regression used in Figure 2.34 to fit the experimental results, it is possible to get the two quantities that characterize the mono-fractal scaling law (Eq.(2.12)):  $d_\theta = 0.49$  and  $\theta_c^* = 0.03 \text{ mm}^{0.49}$ .

The result that must be underlined is the experimental validation of the fundamental relation between the three fractal exponents (Eq.(1.76) for the uniaxial tensile test):

$$d_\sigma + d_G + d_\theta = 0.36 + 0.19 + 0.49 = 1.04 \cong 1 \quad (2.13)$$

At this point, a fractal cohesive law can be derived, starting from the fracture energy definition proposed by RILEM Recommendation (Eq.(1.45)). Disregarding the term related to the weight of the specimen, the fracture energy in a TPB test is (referring to Figure 1.20 and to Figure 1.13):

$$G_F = \frac{1}{A_{lig}} \cdot \int_0^{\delta_0} F \cdot d\delta = \frac{1}{B \cdot (D - a)} \cdot \int_0^{\delta_0} F \cdot d\delta \quad (2.14)$$

The external load  $F$  can be expressed as a function of the stress  $\sigma$ ; supposing a linear elastic distribution of stresses along the ligament:

$$\sigma = \frac{M}{W_{el}} = \frac{F \cdot S/4}{\frac{B \cdot (D - a)^2}{6}} \quad (2.15)$$

the load will be:

$$F = \frac{W_{el} \cdot \sigma}{S/4} \quad (2.16)$$

On the other hand, using Eq.(2.6) and Eq.(2.9), the displacement  $\delta$  can be expressed as a function of  $\bar{w}$  :

$$\bar{w} = D \cdot \frac{\delta}{S/2} \quad (2.17)$$

Consequently:

$$d\delta = \frac{S}{2 \cdot D} \cdot d\bar{w} \quad (2.18)$$

Substituting Eq.(2.18) and Eq.(2.16) in Eq.(2.14), and remembering that for  $\delta = \delta_0$  Eq.(2.10) provides  $\bar{w} = \bar{w}_c$  , it is possible to write:

$$G_F = \frac{2 \cdot W_{el}}{A_{lig} \cdot D} \cdot \int_0^{\bar{w}_c} \sigma \cdot d\bar{w} = \frac{1}{3} \cdot \frac{(D - a)}{D} \cdot \int_0^{\bar{w}_c} \sigma \cdot d\bar{w} \quad (2.19)$$

The specimens recommended by RILEM TC 50-FMC, that are the object of the present work, present a notch depth  $(D - a) = D/2$  ; consequently:

$$G_F = \frac{1}{6} \cdot \int_0^{\bar{w}_c} \sigma \cdot d\bar{w} \quad (2.20)$$

Using Eq.(2.9) and Eq.(2.11), the power law concerning the crack opening displacement can be deduced:

$$\bar{w} = \theta_c^* \cdot D^{1-d_\theta} \quad (2.21)$$

Introducing Eq.(2.21) and Eq.(1.77) into Eq.(2.20), the fracture energy will be expressed as:

$$G_F = \frac{1}{6} \cdot \int_0^{\theta_c^*} \sigma^* \cdot D^{-d_\sigma} \cdot D^{1-d_\theta} \cdot d\theta^* = D^{1-d_\theta-d_\sigma} \cdot \frac{1}{6} \cdot \int_0^{\theta_c^*} \sigma^* \cdot d\theta^* \quad (2.22)$$

Comparing Eq.(2.22) with the mono-fractal scaling law defined for fracture energy (Eq.(1.63)), the fundamental relation between fractal exponents is found again:

$$1 - d_\theta - d_\sigma = d_G \quad (2.23)$$

Furthermore:

$$G_F^* = \frac{1}{6} \cdot \int_0^{\theta_c^*} \sigma^* \cdot d\theta^* \quad (2.24)$$

Eq.(2.24) represents the definition of the renormalized fracture energy as the area under the fractal cohesive law  $\sigma^*(\theta^*)$ , that is the real material property, function of the renormalized values of fracture energy, bending strength and critical rotation angle.

## 2.4 Damage monitoring by Acoustic Emission and modal frequency analysis

In addition to the study of scale effects on mechanical properties of concrete, another purpose of the present thesis is to apply Acoustic Emission and Dynamic Identification techniques.

In the first part of this section, AE results will be presented and discussed; particular attention will be reserved to the Rise Angle analysis, in order to perform a classification of the cracks corresponding to the acquired AE signals. Finally, scale effects on the AE energy per unit ligament area will be underlined and interpreted in the context of the fractal theory.

In the second part the decrease of natural frequencies of the specimens with a depth of 10 cm and 40 cm (Test\_100\_2 and Test\_400\_3) will be shown. Furthermore, for the 10 cm specimen, an attempt to apply an inverse procedure, in order to correlate the decrease of natural frequency experimentally observed with an approximate

value of crack propagation, will be proposed, using the numerical (FEM) results presented in Section [2.2.2].

In the third part the correlations between the two damage monitoring techniques will be shown, pointing out their benefits and cons.

### 2.4.1 AE Analysis

AE sensors were applied in all the tests, except in Test\_200\_1: AE results concerning a 20 cm specimen can be found in the article by Carpinteri, Lacidogna, Corrado, Di Battista (2016), with respect to Test\_200\_2.

In this section the main results obtained with AE analysis will be presented in terms of emitted energy, cumulated AE events, Average Frequencies (AF) of signals and Rise Angle (RA) values. For this purpose, a test for each specimen size will be taken into account.

Each signal, captured by AE sensors during the tests, was analysed by an algorithm implemented in LabVIEW (National Instruments), which is able to calculate the Fast Fourier Transform (FFT). Observing the FFT, it is possible to identify the frequency to which most of the signal's energy is associated. In Figure 2.35 a typical recorded AE signal is represented, while the FFT of an AE signal is shown in Figure 2.36.

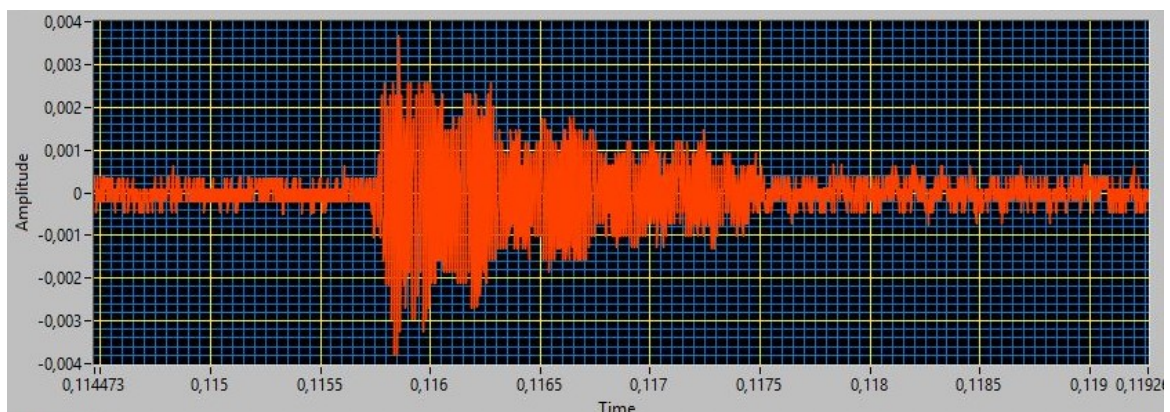


Figure 2.35: A typical AE signal recorded by piezoelectric sensors

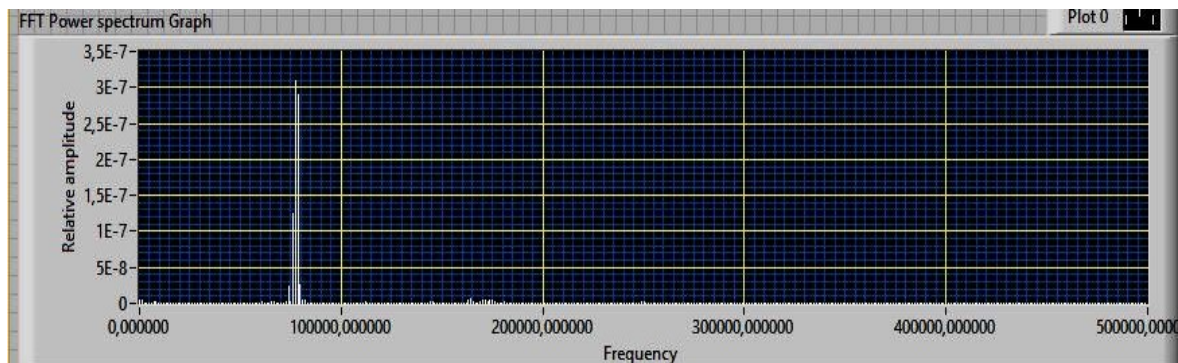


Figure 2.36: FFT (Fast Fourier Transform) of an AE signal

The amplitudes of recorded AE signals were amplified of 60 dB before being processed. Using Eq.(1.83) the energy of each AE signal was calculated, so that it was possible to obtain the cumulated value of the emitted energy at the end of each test.

In the following, the results related to only one AE sensor will be presented, also if during the tests more than one resonant sensors were applied to the specimens.

#### 2.4.1.1 Cumulated AE energy

The tests that will be considered to discuss the AE results are: Test\_100\_1 ( $D = 10\text{ cm}$ ), Test\_300\_1 ( $D = 30\text{ cm}$ ) and Test\_400\_2 ( $D = 40\text{ cm}$ ). The cumulated AE energy vs. time diagrams for these tests are represented respectively in Figure 2.37, Figure 2.38 and Figure 2.39, where they are superimposed to the correspondent load-time curve of the test.

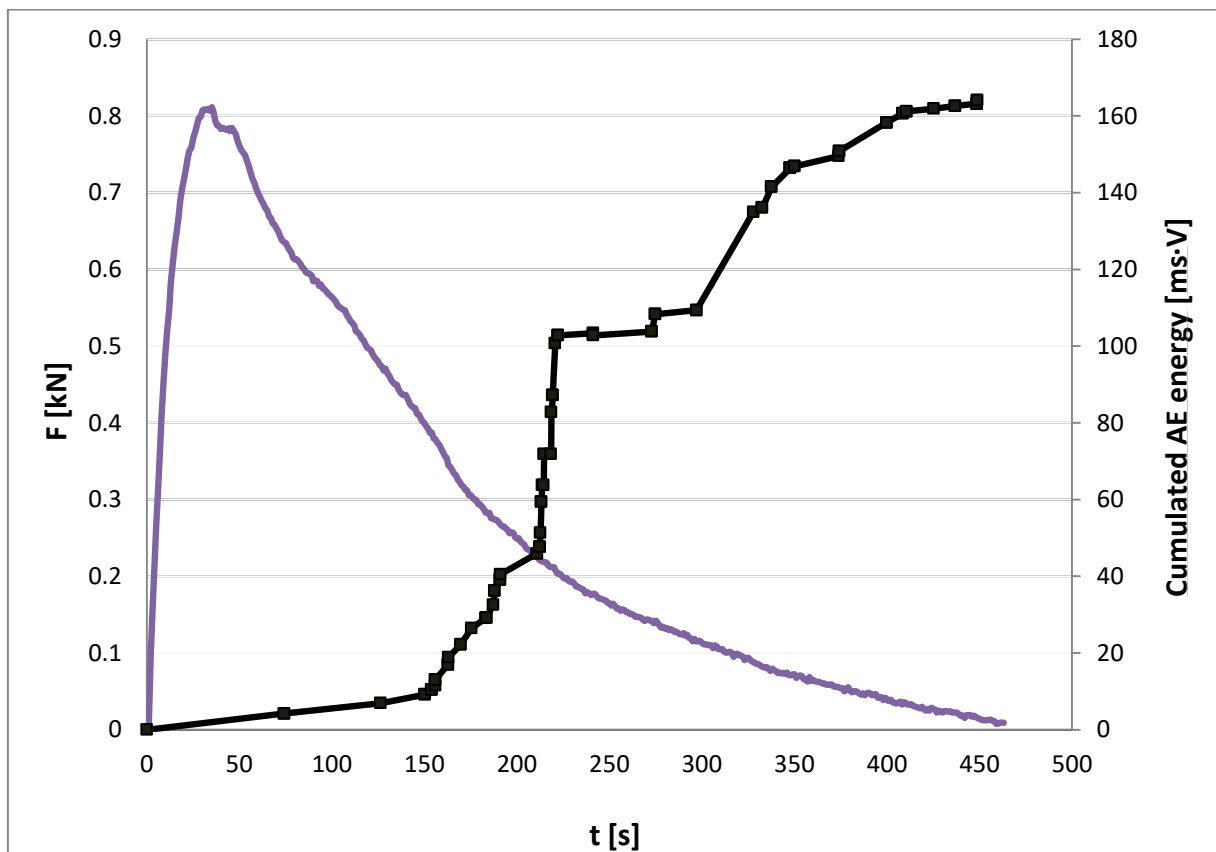


Figure 2.37: Load and cumulated AE energy vs. time diagrams for 10 cm specimen (Test\_100\_1)

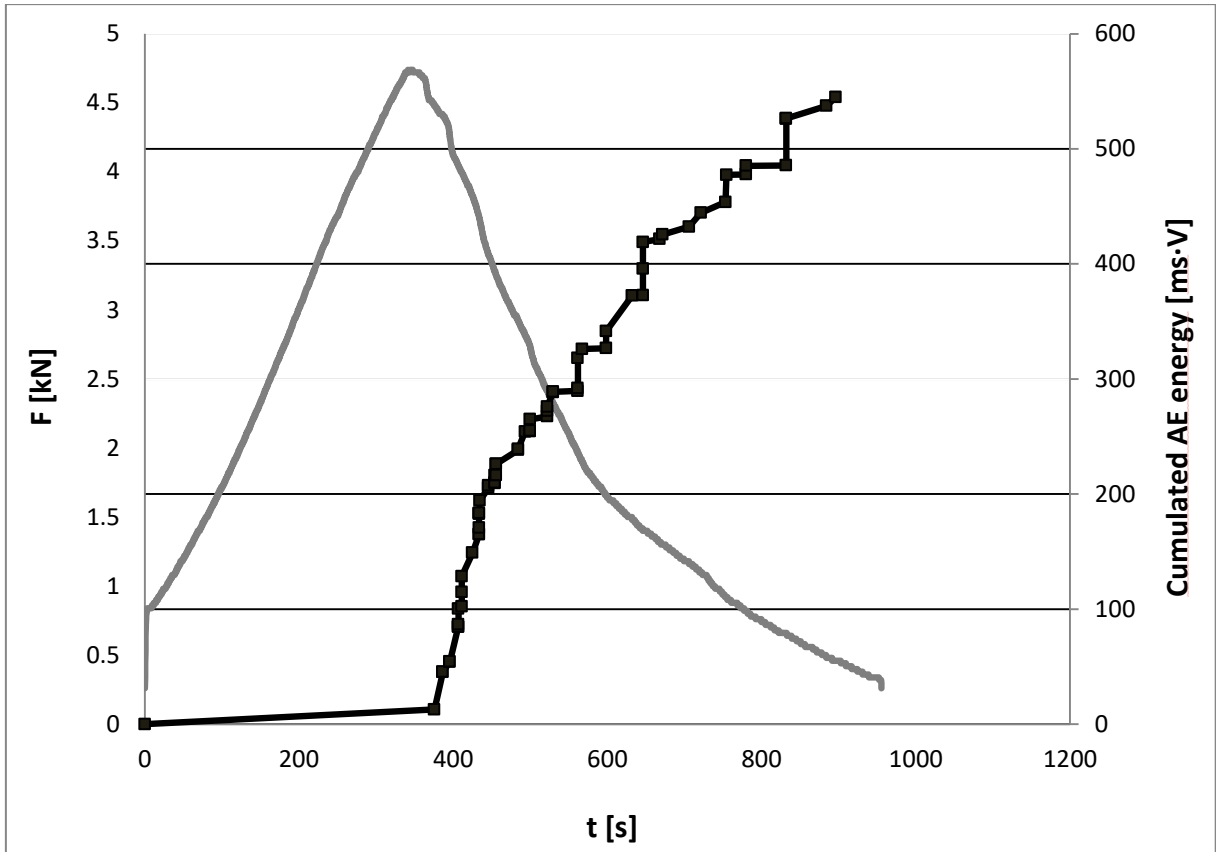


Figure 2.38: Load and cumulated AE energy vs. time diagrams for 30 cm specimen (Test\_300\_1)

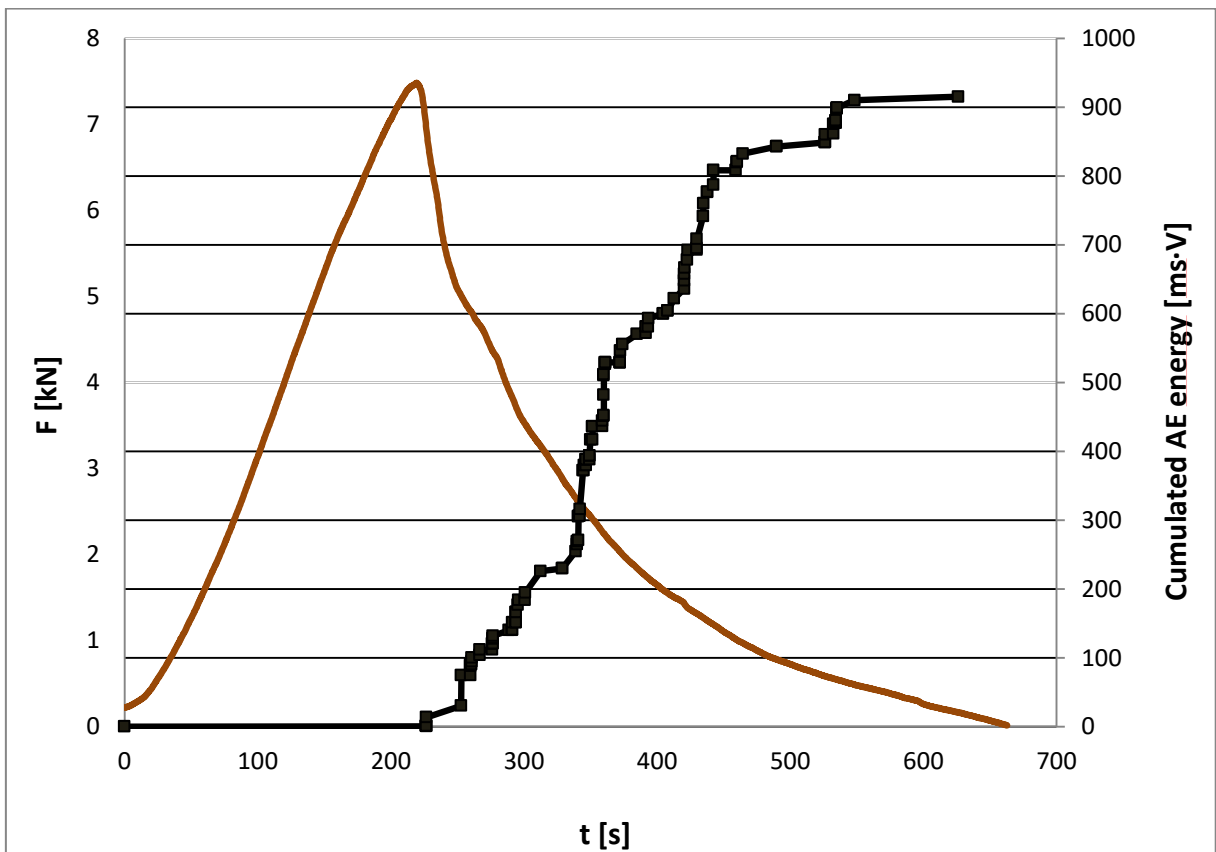


Figure 2.39: Load and cumulated AE energy vs. time diagrams for 40 cm specimen (Test\_400\_2)

Sudden increases of AE energy correspond to local snap-back instabilities (micro-cracking). The same can be observed by looking at the cumulated AE events vs. time diagrams in Figure 2.40.

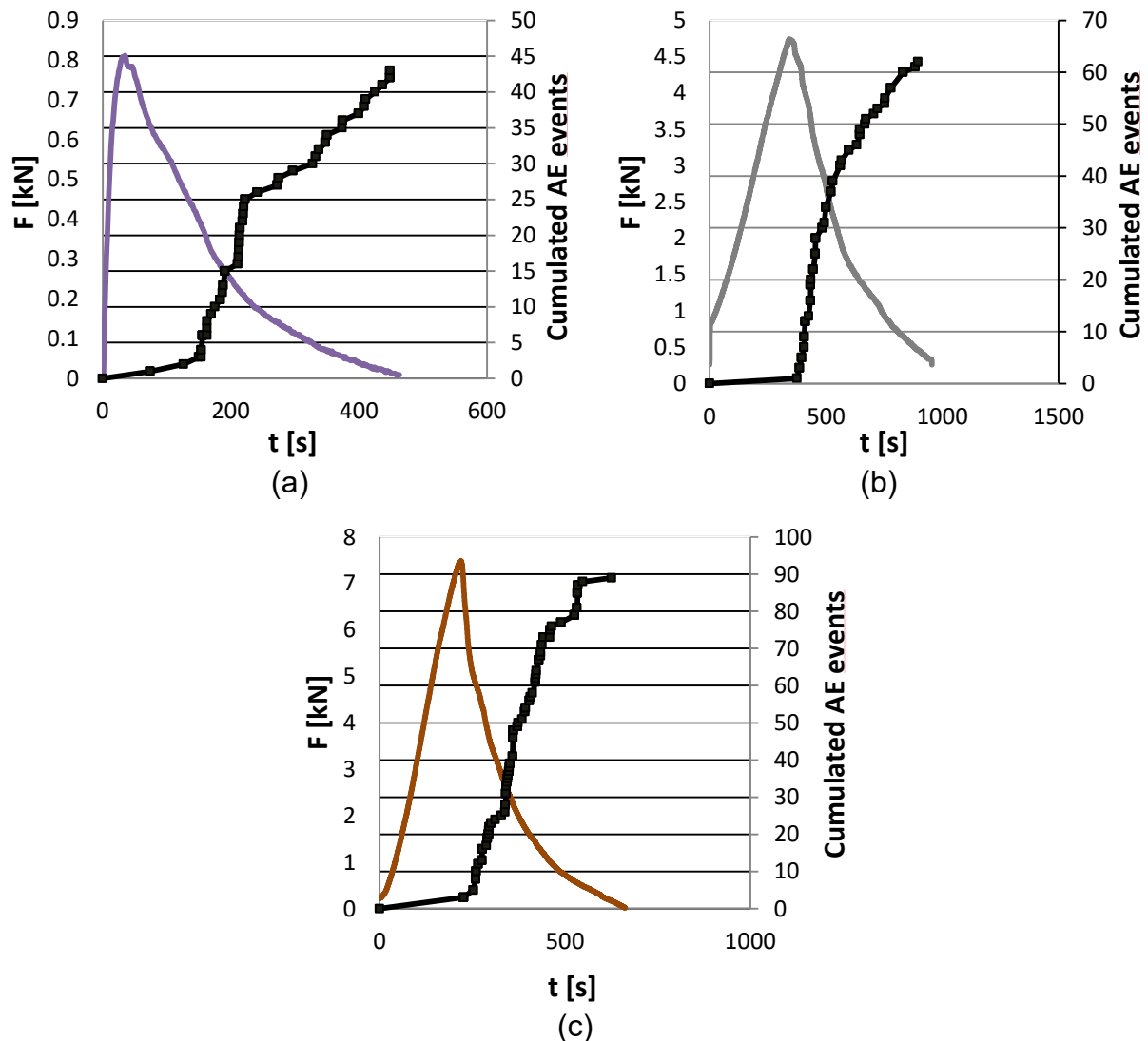


Figure 2.40: Load and cumulated AE events vs. time diagrams for (a) 10 cm specimen (Test\_100\_1), (b) 30 cm specimen (Test\_300\_1) and (c) 40 cm specimen (Test\_400\_2)

#### 2.4.1.2 Characterization of the fracture mode by Rise Angle value and Average Frequency

In Section [1.2.2] the simple method, proposed by Ohtsu, to classify the cracks using the results of AE analysis was described. It is used in the present work: for each signal, the Rise Angle (RA) value was evaluated, using the Rise Time and the amplified peak amplitude (Eq.(1.84)); from the FFT, the Average Frequency of each signal was determined. Consequently, it is possible to represent each captured AE signal by a point in the AF vs. RA field. Considering again Test\_100\_1 ( $D = 10\text{ cm}$ ), Test\_300\_1 ( $D = 30\text{ cm}$ ) and Test\_400\_2 ( $D = 40\text{ cm}$ ), this representation of AE signals is presented respectively in Figure 2.41, Figure 2.42 and Figure 2.43. The

method consists in tracing the bisector of this diagram: if the point associated to an AE signal is placed above this bisector, that signal is related to a mode I crack; if the point is below, it corresponds to a mode II crack.

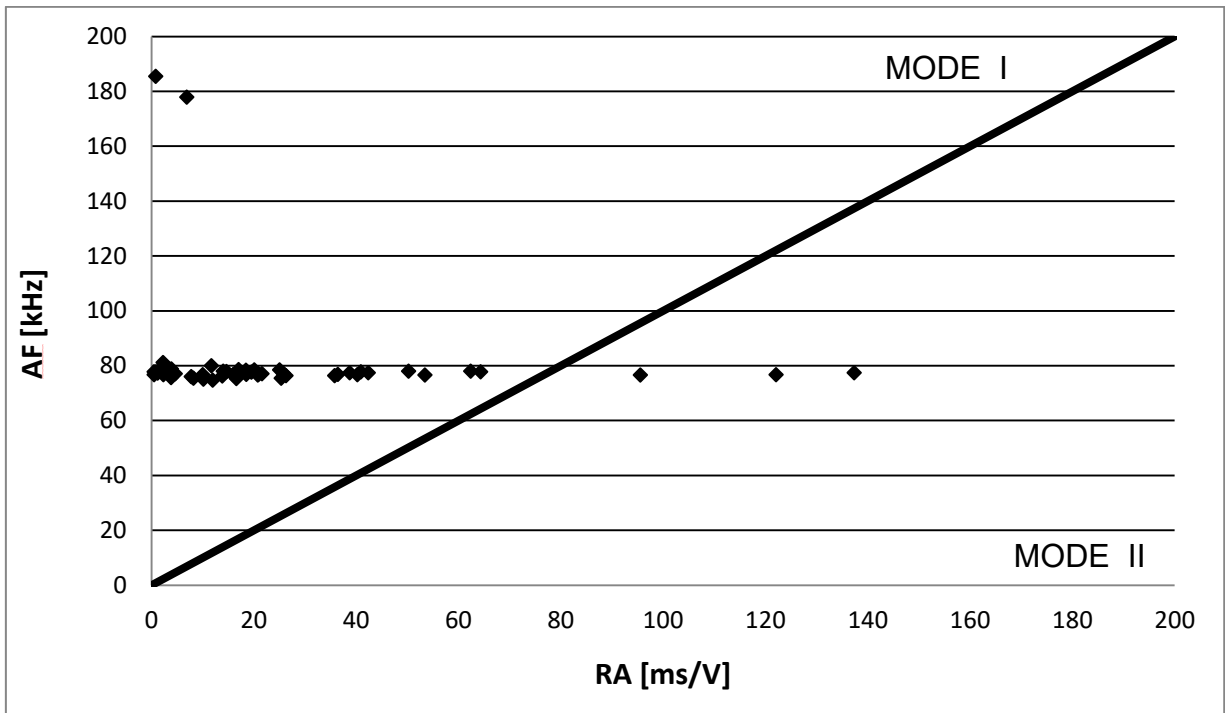


Figure 2.41: RA values of detected AE events in Test\_100\_1 (D=10 cm)

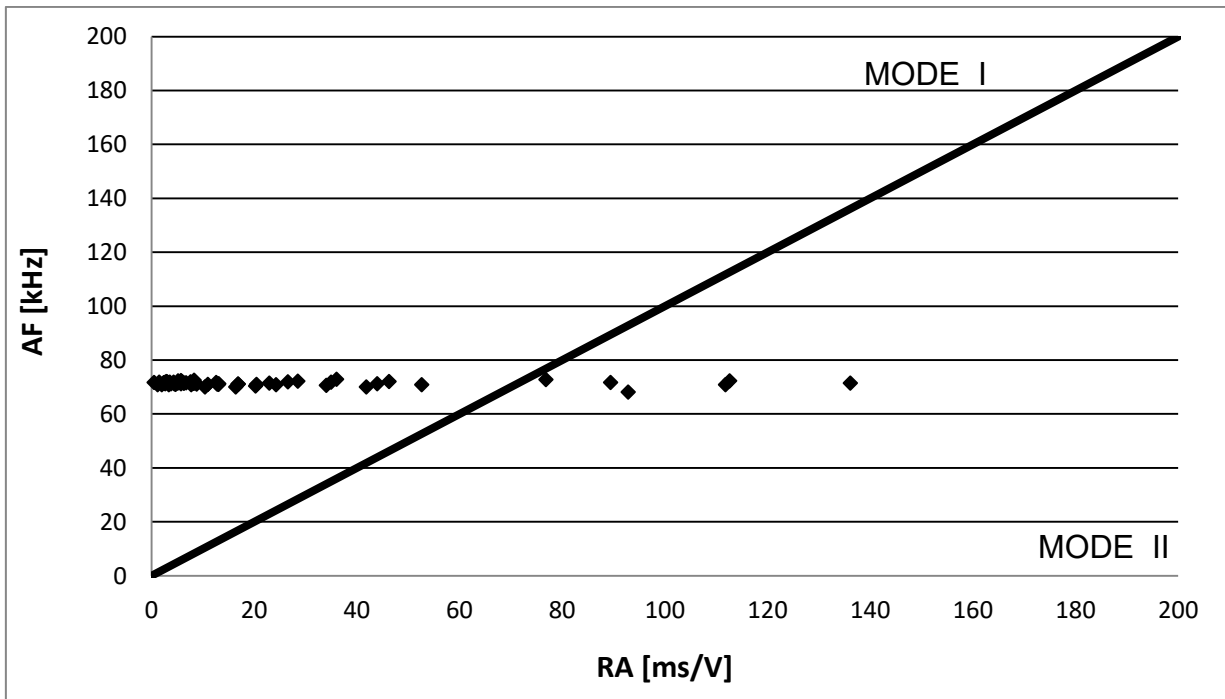


Figure 2.42: RA values of detected AE events in Test\_300\_1 (D=30 cm)

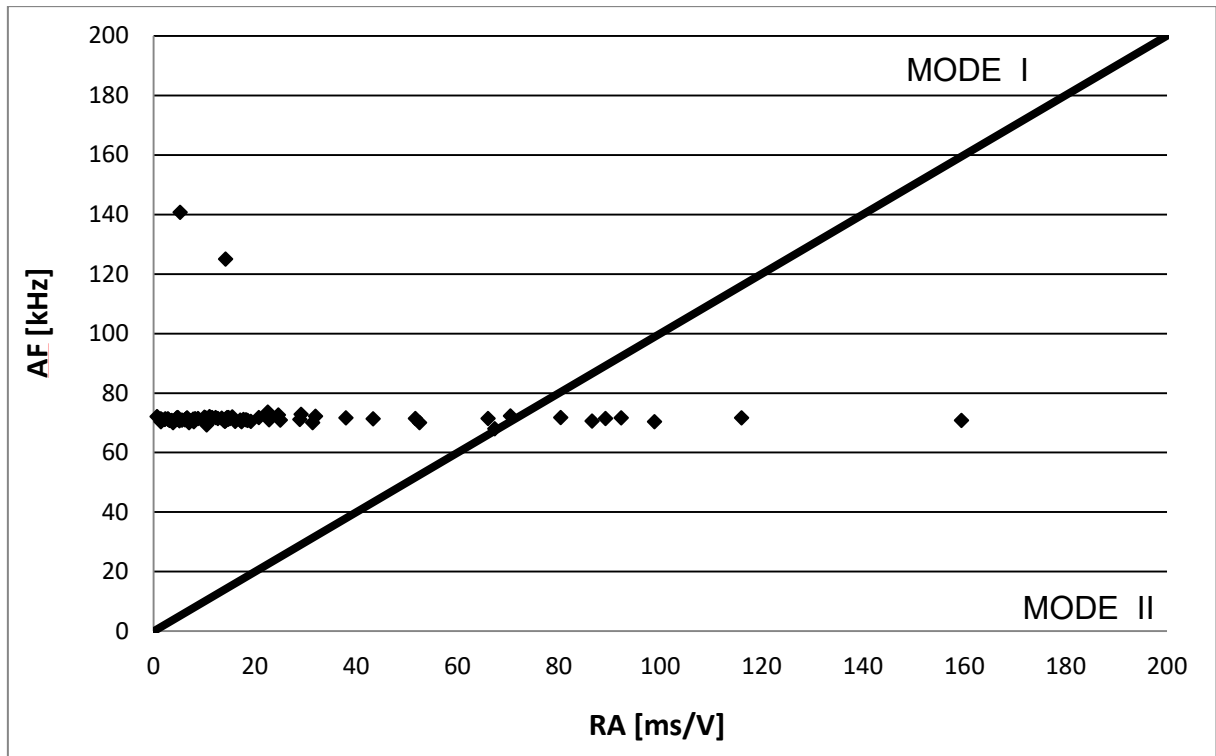


Figure 2.43: RA values of detected AE events in Test\_400\_2 (D=40 cm)

The frequencies of the captured AE signals are almost the same and equal to about 75 kHz; this happens because the AE sensor used is a resonant one. As expected in a bending test, the prevalent cracking mode is the Mode I, i.e. the opening mode (Figure 1.37a).

#### 2.4.1.3 Scale effects on the specific AE energy: A fractal explanation

In Section [2.4.1.1] the cumulated AE energy and AE events vs. time diagrams are shown for three different specimen sizes. Obviously, the absolute values of AE energy and AE events increase with the specimen size. It is resumed in Table 12 and represented graphically in Figure 2.44 and Figure 2.45.

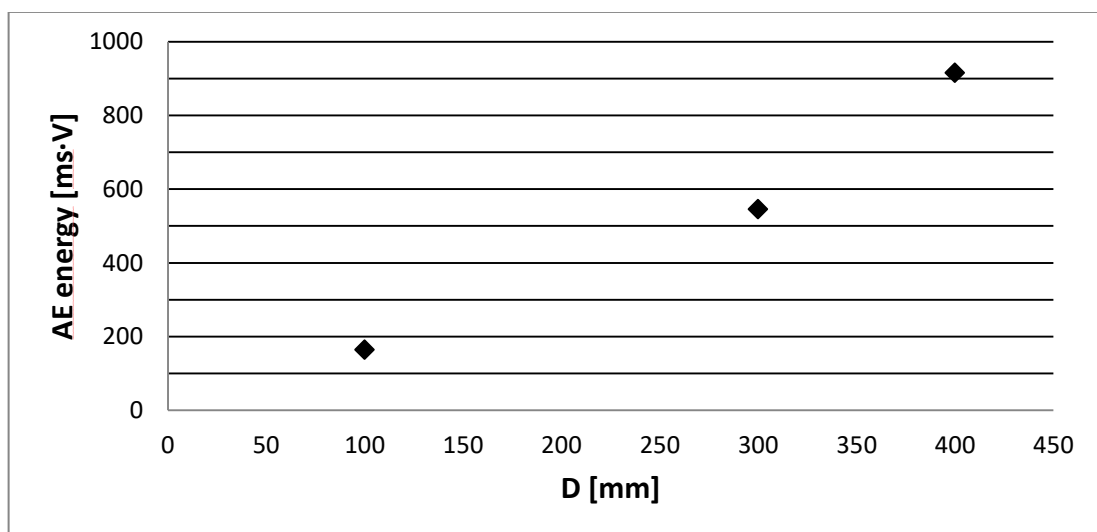


Figure 2.44: Absolute values of AE energy for three specimen sizes (Test\_100\_1, Test\_300\_1, Test\_400\_2)

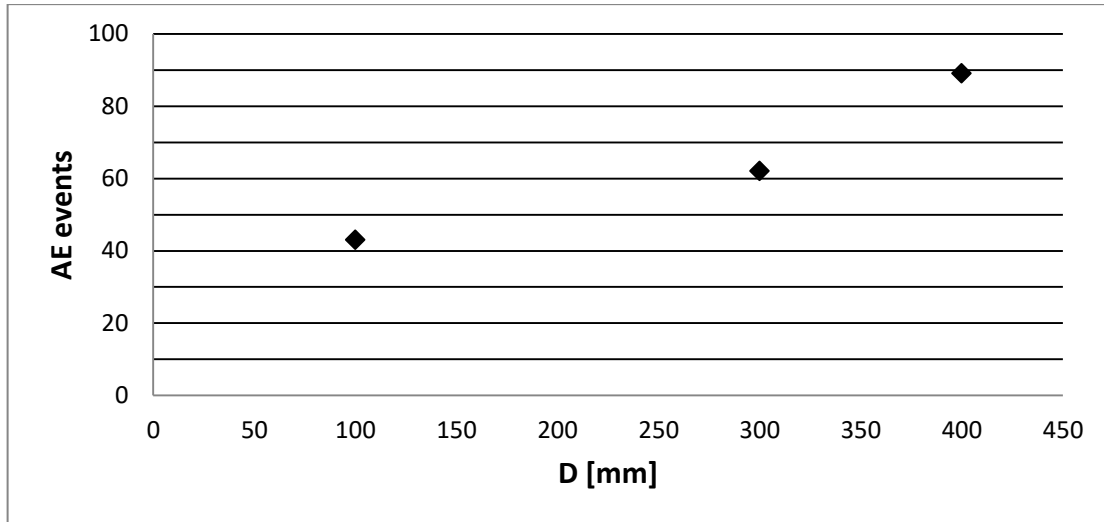


Figure 2.45: AE events for three specimen sizes (Test\_100\_1, Test\_300\_1, Test\_400\_2)

	$D = 10 \text{ cm}$ (Test_100_1)	$D = 30 \text{ cm}$ (Test_300_1)	$D = 40 \text{ cm}$ (Test_400_2)
$AE \text{ energy}$ [ms·V]	164.0	544.8	915.1
$AE \text{ events}$	43	62	89
$\frac{AE \text{ energy}}{\text{ligament area}}$ [ms·V/m <sup>2</sup> ]	32800	24213	22878

Table 12: Absolute AE energy, AE events and AE energy per surface unit for three different beam sizes

In Table 12, the values of AE energy divided by the ligament area of the corresponding specimen are also reported. It is clear how this specific value of the emitted energy decreases with the increase of specimen size. The same result was obtained also in the article by Carpinteri, Lacidogna, Corrado, Di Battista (2016). Thus, the AE energy per unit area exhibits an opposite trend with respect to the fracture energy (see Table 11). It is a further demonstration of the complete independence between the emitted and the dissipated energy.

The values of the specific AE energy presented in Table 12 are graphically represented in a bilogarithmic diagram in Figure 2.46. An attempt to apply a mono-fractal scaling law even for the emitted energy is now proposed. Actually, Figure 2.46 shows that a linear regression in the bilogarithmic diagram fits well with experimental data. This straight line should be represented by the following equation:

$$\ln \bar{E}_{EA} = \ln \bar{E}_{EA}^* - d_{EA} \cdot \ln D \quad (2.25)$$

where  $\bar{E}_{EA}$  represents the total AE energy measured in a test divided by the ligament area of the specimen.  $\bar{E}_{EA}^*$  is instead the renormalized specific AE energy, that should represent the true material constant, independent from the scale;  $d_{EA}$  is the fractal (lacunar) exponent for the emitted energy. Practically the hypothesis proposed in this paragraph is that the AE energy is emitted during the damage in a lacunar fractal

domain with physical dimension lower than 2. Consequently, dissipated energy (fracture energy) and emitted energy (AE energy) are released on two different fractal domains: the former is invasive, the latter is lacunar.

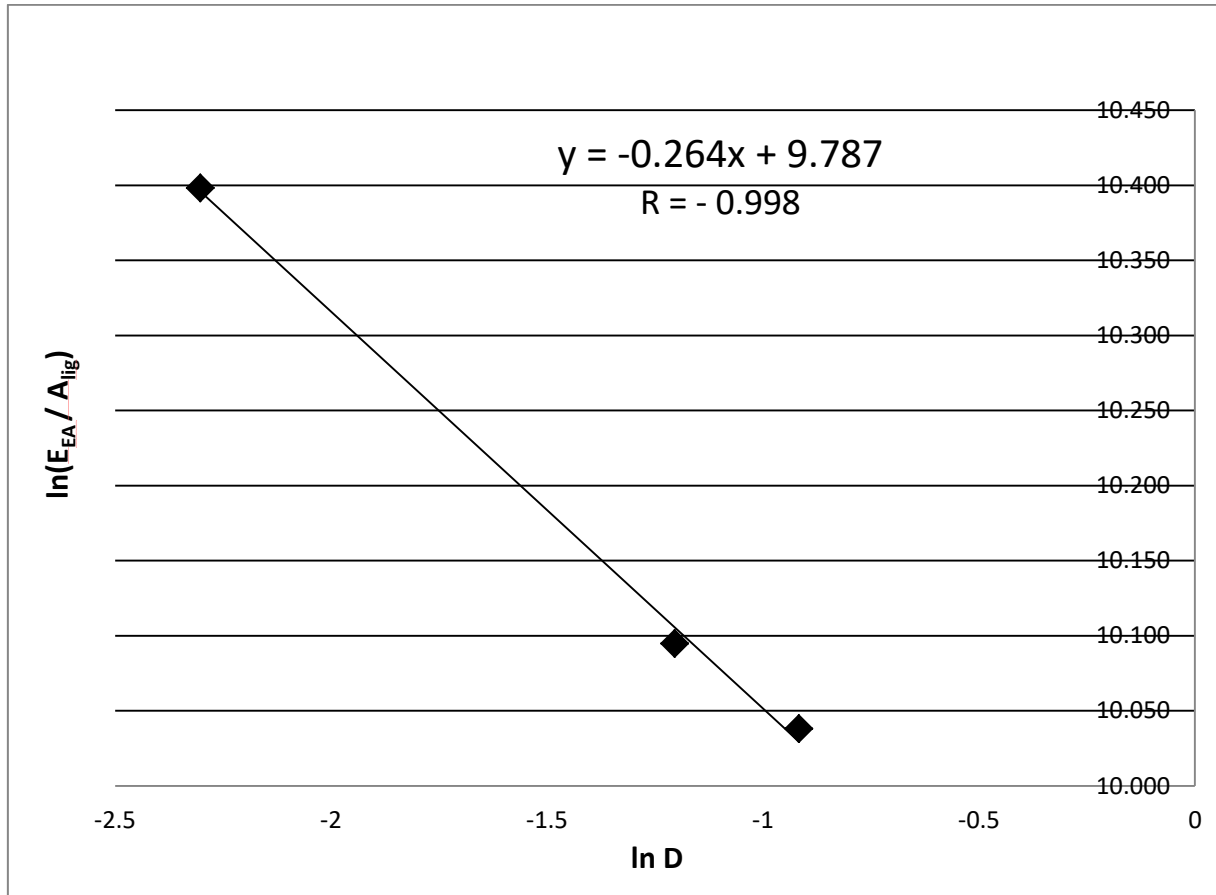


Figure 2.46: Scale effects on AE energy per unit area: mono-fractal scaling law

From the equation of the linear regression shown in Figure 2.46, in light of Eq.(2.25), it is deduced that  $d_{EA} = 0.26$  while  $\bar{E}_{EA}^* = 17800 \text{ ms} \cdot \text{V} \cdot \text{m}^{-1.74}$ .

Thus the AE energy seems to be emitted on a lacunar fractal domain with a physical dimension  $[L]^{1.74}$ . Eq.(2.25) can be rewritten as a power law:

$$\bar{E}_{EA} = \bar{E}_{EA}^* \cdot D^{-d_{EA}} \quad (2.26)$$

## 2.4.2 Modal frequency variation

During Test\_100\_2 and Test\_400\_3 the Dynamic Identification technique was applied: these two tests were stopped several times, in order to excite the specimens by impulsive forces and to capture, by means of four piezoelectric pickups, the free response signals.

The recording of the free vibration signals allowed the extraction of the natural frequencies of the two specimens in correspondence of each step in which the tests were stopped. In fact, using a FFT (Fast Fourier Transform) algorithm implemented in

MATLAB, it was possible to evaluate the PSD (Power Spectral Density). This latter contains different peaks, in correspondence of the frequencies related to the vibration modes of the specimen that reacted with greater energy to the impulsive force. However, these modes could concern all the possible motions of the specimen in the space (axial modes, torsional, lateral or vertical bending etc.). In order to individuate the peaks of interest, corresponding to the vertical bending modes, a modal analysis was performed with LUSAS software using a Finite Element Model for the 10 cm and 40 cm specimens (the results are presented in Section [2.2.1]).

First of all, the electrical signals captured by the four PZT pickups are acquired by an audio device (8-channel Audiobox 1818VS1 acquisition device by PreSonus) and recorded as audio tracks (.WAV extension) by the software StudioOne2 produced by PreSonus. In each step of the test, five acquisitions (due to five impulsive forces) were made. In Figure 2.47 one of these signals is represented. Using the already mentioned algorithm implemented in MATLAB, it was possible to perform the frequency analysis of each signal by evaluating the PSD (an example is in Figure 2.48). Knowing the frequencies of interest (those related to the first three vertical bending modes) from the numerical analysis, it was possible, using the PSD, to evaluate the bending natural frequencies of specimens in each step, in order to estimate their decrease with the crack growth. The final values of those frequencies in each step were obtained evaluating for each sensor the average of the five acquisitions; finally the average of these values related to the four sensors were considered. Table 13 contains the so evaluated frequencies with respect to the 10 cm specimen (Test\_100\_2).

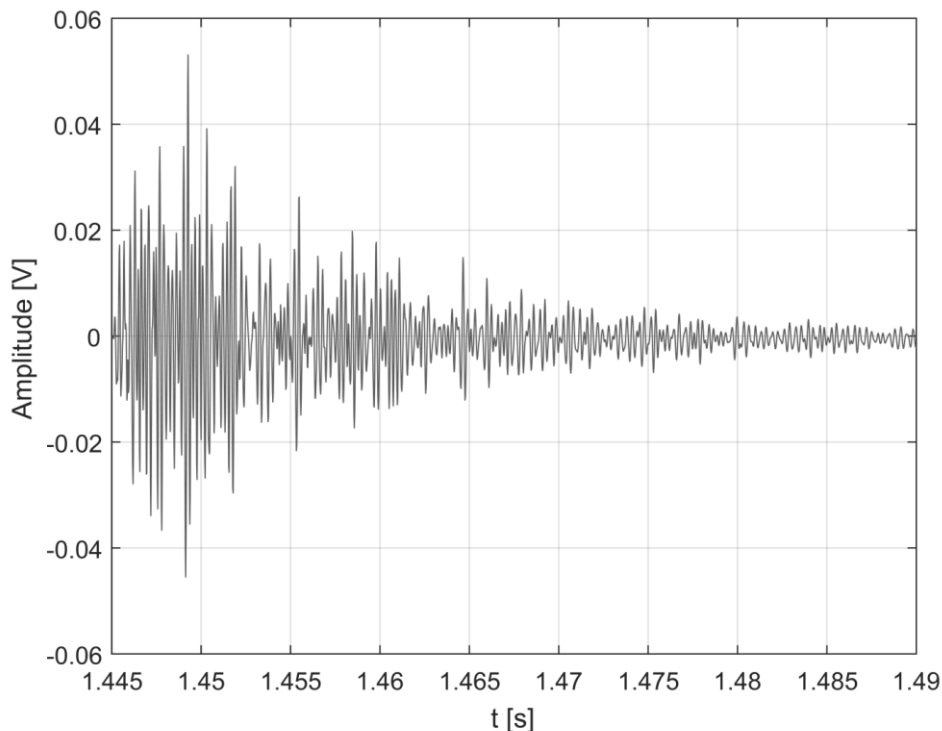


Figure 2.47: Free response signal due to an impulsive force

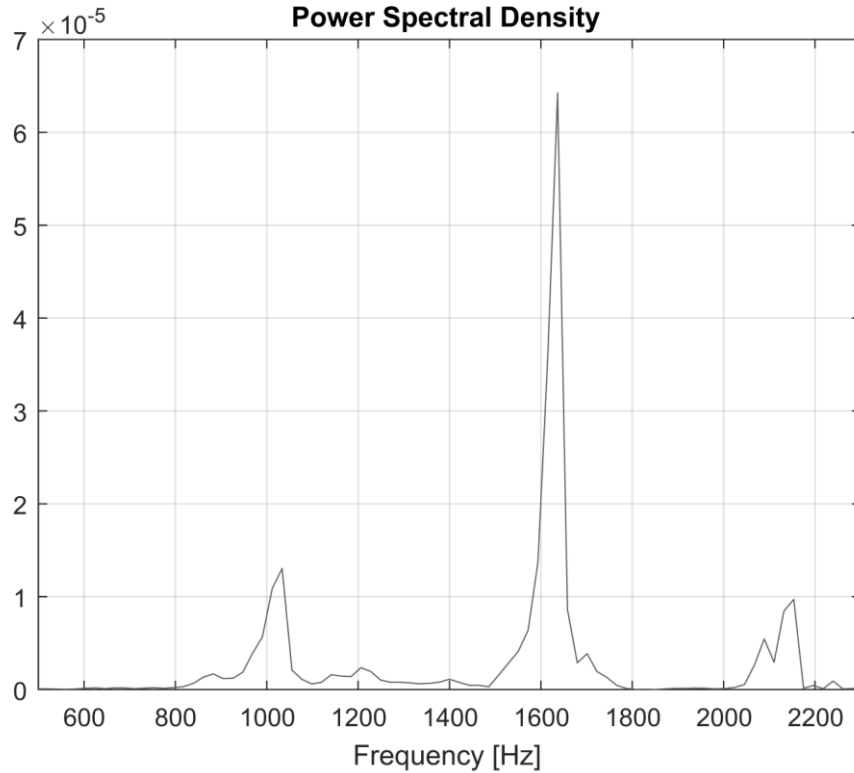


Figure 2.48: Power Spectral Density (PSD) of a free response signal due to an impulsive force

	$\delta$ [mm]	Natural bending frequency related to Asym1 mode [Hz]	Natural bending frequency related to Sym mode [Hz]	Natural bending frequency related to Asym2 mode [Hz]
Step I	0.170	1018.9	1145.8	3279.5
Step II	0.236	1015.5	1141.2	3284.9
Step III	0.361	1006.1	1124.3	3270.9
Step IV	0.462	990.9	1060.8	3236.5
Step V	0.561	972.6	1021.1	3214.9
Step VI	0.763	969.4	917.3	3146.2
Step VII	0.974	962.9	885.9	3088.1
Step VIII	1.160	946.6	878.5	3017.2
Step IX	1.512	934.8	854.8	2918.4
Step X	1.762	928.2	840.7	2846.3
Total decrease		8.9%	26.6 %	13.2 %

Table 13: Values of the first three natural frequencies of 10 cm specimen experimentally evaluated in each step of Test\_100\_2 and their total observed decrease in percentage (the names of the modes are referred to Figure 2.9)

The experimentally evaluated decrease of the first three natural bending frequencies of the 10 cm specimen is represented in Figure 2.49 in a unique diagram, together

with the load-deflection curve of Test\_100\_2, and separately in Figure 2.50, Figure 2.51 and Figure 2.52.

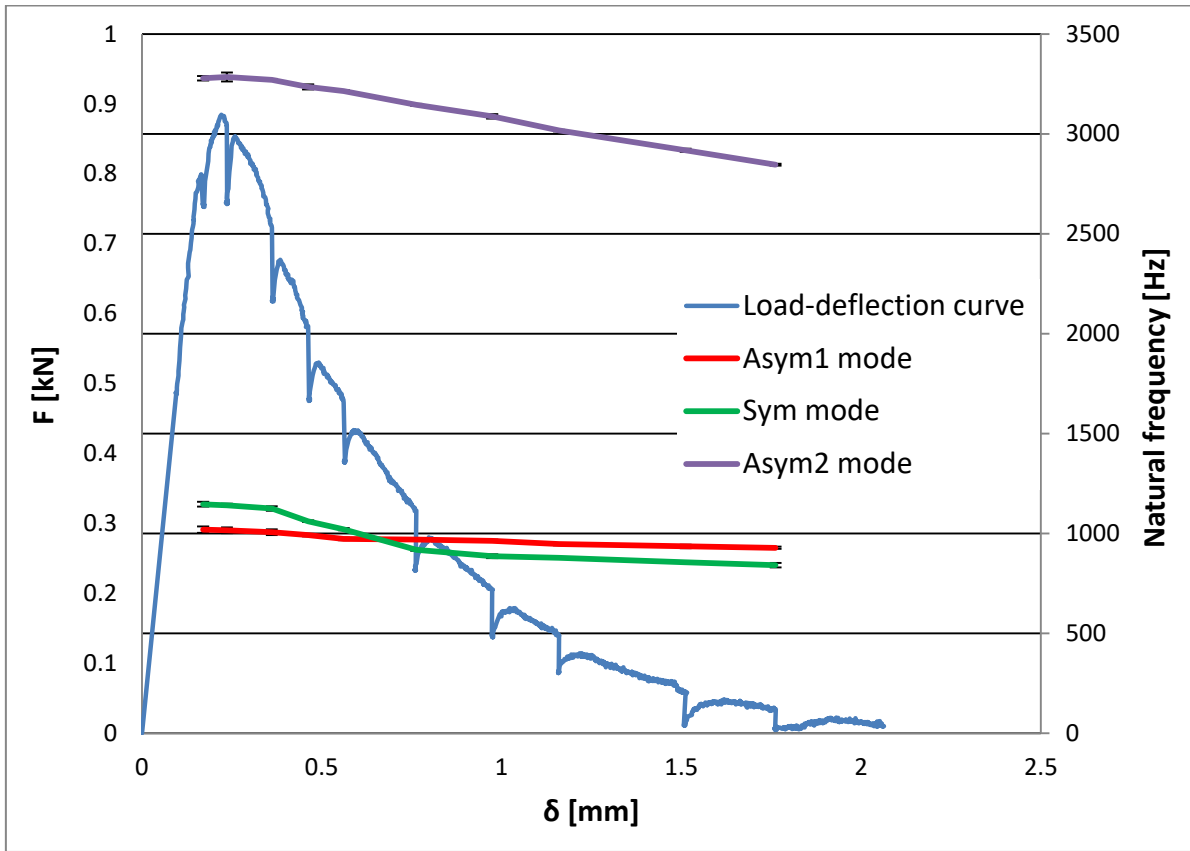


Figure 2.49: Experimentally evaluated decrease of the first three natural frequencies of the 10 cm specimen with the imposed vertical displacement during Test\_100\_2

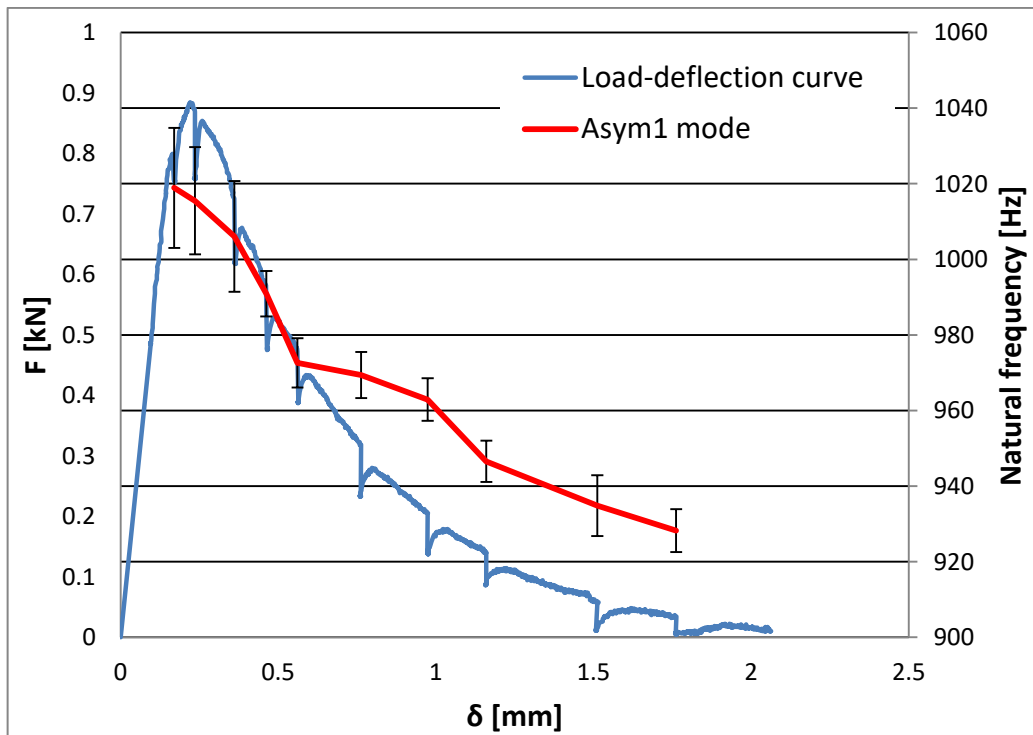


Figure 2.50: Experimentally evaluated decrease of the natural frequency related to asym1 mode of the 10 cm specimen during Test\_100\_2

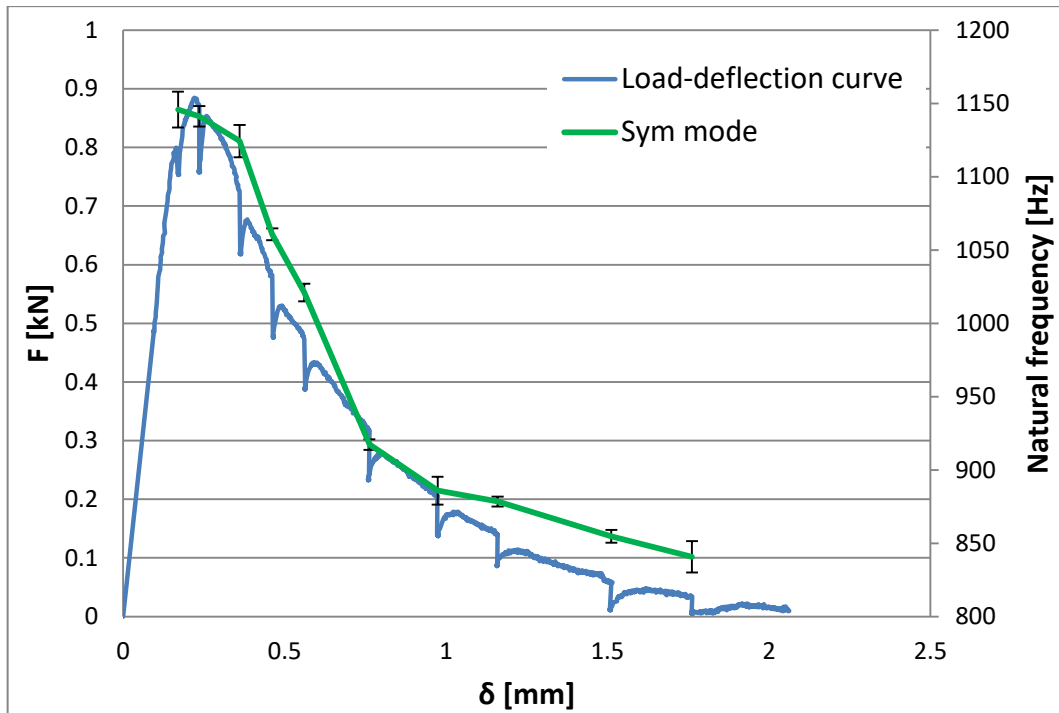


Figure 2.51: Experimentally evaluated decrease of the natural frequency related to sym mode of the 10 cm specimen during Test\_100\_2

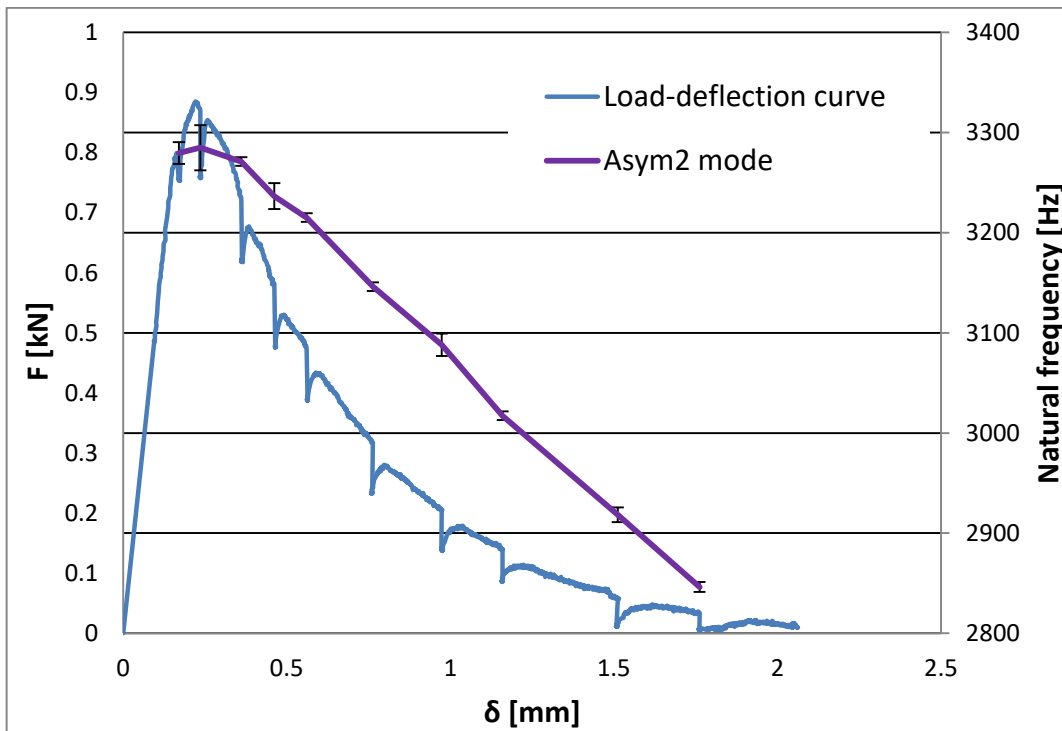


Figure 2.52: Experimentally evaluated decrease of the natural frequency related to asym2 mode of the 10 cm specimen during Test\_100\_2

In Test\_100\_2 the acquisitions of the free response signals were made only in the post-peak phase, because before the peak load the natural frequencies supposedly remain constant. The biggest decrease interests the frequency related to the

symmetric mode: it results the second frequency at the beginning of the test; then, with the damage progress, it becomes the first one.

The experimental results are in agreement with the numerical ones presented in Section [2.2.2]: comparing Table 13 with Table 9 it is possible to observe that the total decrease of the three natural frequencies, expressed as a percentage, is almost the same in the experimental and numerical (FEM) evaluation. In particular, in the numerical analysis it was determined as a function of the relative crack depth (Figure 2.13). Consequently, an inverse procedure can be applied, in order to associate the decrease of natural frequencies experimentally observed with an approximate value of the crack depth and so of the damage severity. Since the mode associated to final stages and collapse is the symmetric one, the corresponding frequency was selected to apply this inverse procedure. Overlapping the variation numerically (FEM) determined (Figure 2.13) with the experimental one (Figure 2.51), an approximate value of relative crack depth can be obtained. This combination is presented in Table 14. Figure 2.53 shows the overlap of experimental and numerical curves in dimensionless terms (dividing by the initial value of the natural frequency).

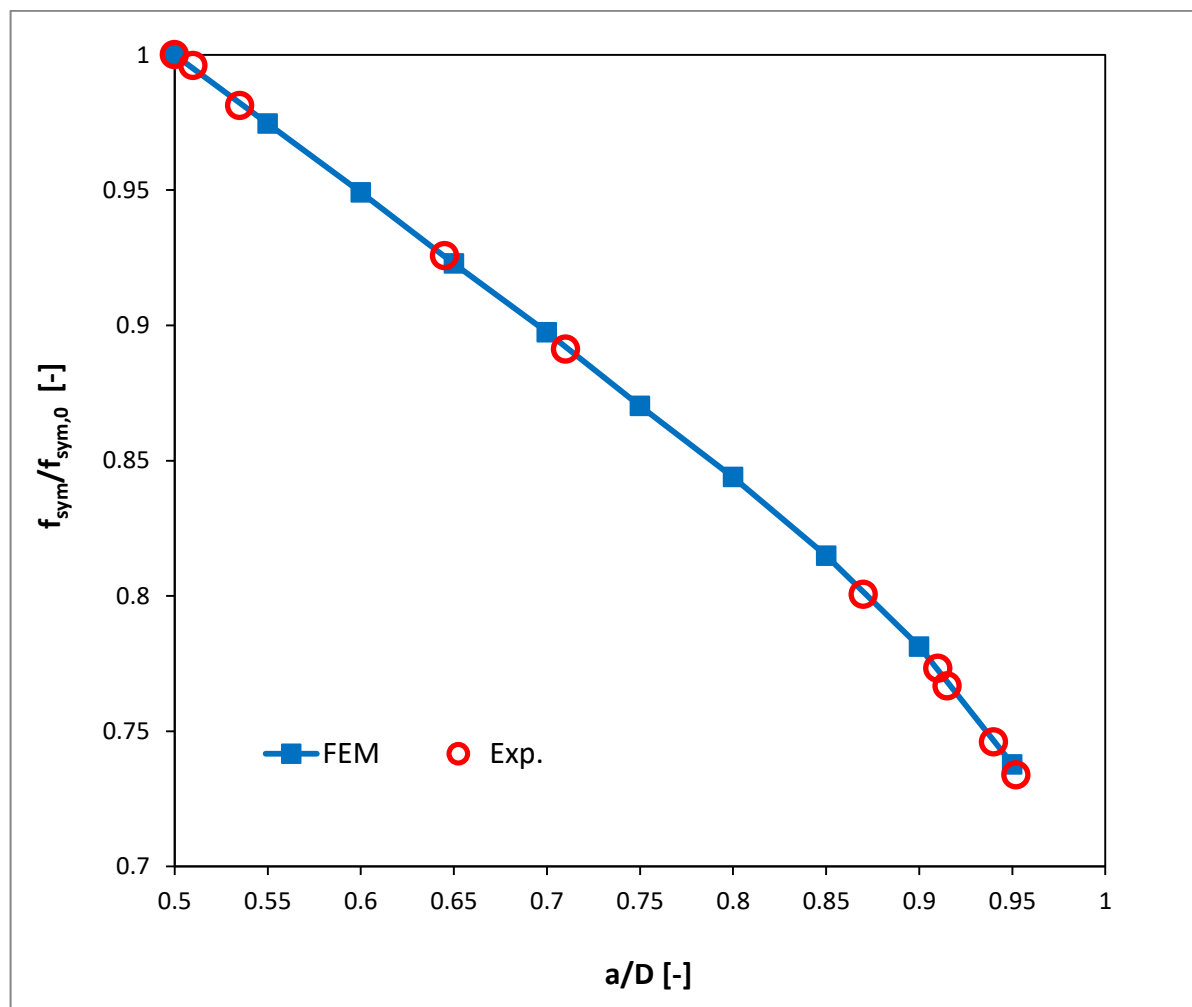


Figure 2.53: Overlap of dimensionless experimental values with the dimensionless numerical (FEM) curve describing the variation of the natural frequency, related to the symmetric mode of the 10 cm specimen (Test\_100\_2), as a function of the relative crack depth

	$\delta$ [mm]	Natural bending frequency related to Sym mode [Hz]	Estimated relative crack depth $a/D$ [-]
Step I	0.170	1145.8	0.500
Step II	0.236	1141.2	0.510
Step III	0.361	1124.3	0.535
Step IV	0.462	1060.8	0.645
Step V	0.561	1021.1	0.710
Step VI	0.763	917.3	0.870
Step VII	0.974	885.9	0.910
Step VIII	1.160	878.5	0.915
Step IX	1.512	854.8	0.940
Step X	1.762	840.7	0.952

Table 14: Estimated values of the relative crack depth in the different steps considered in Test\_100\_2 with the 10 cm specimen, using the natural frequency related to the symmetric mode

The Dynamic Identification technique was applied also in Test\_400\_3 on the 40 cm specimen. Table 15 contains the experimental values of the first three natural frequencies corresponding to the bending modes of the beam represented in Figure 2.10. The decrease of these three natural frequencies is shown in a unique diagram in Figure 2.54 together with the load-deflection curve of Test\_400\_3, and separately in Figure 2.55, Figure 2.56 and Figure 2.57.

	$\delta$ [mm]	1 <sup>st</sup> natural bending frequency [Hz]	2 <sup>nd</sup> natural bending frequency [Hz]	3 <sup>rd</sup> natural bending frequency [Hz]
Step I	0.044	693	815	2102
Step II	0.187	693	816	2106
Step III	0.383	694	816	2106
Step IV	0.500	689	811	2065
Step V	0.550	683	808	2038
Step VI	0.600	674	799	2022
Step VII	0.650	674	795	1998
Step VIII	0.700	660	793	1969
Step IX	0.800	657	787	1930
Step X	1.000	644	770	1872
Step XI	1.200	641	758	1835
Total decrease		5.8%	5.7%	12.7%

Table 15: Values of the first three natural frequencies of 40 cm specimen experimentally evaluated in each step of Test\_400\_3 and their total observed decrease in percentage (the modal shapes are represented in Figure 2.10)

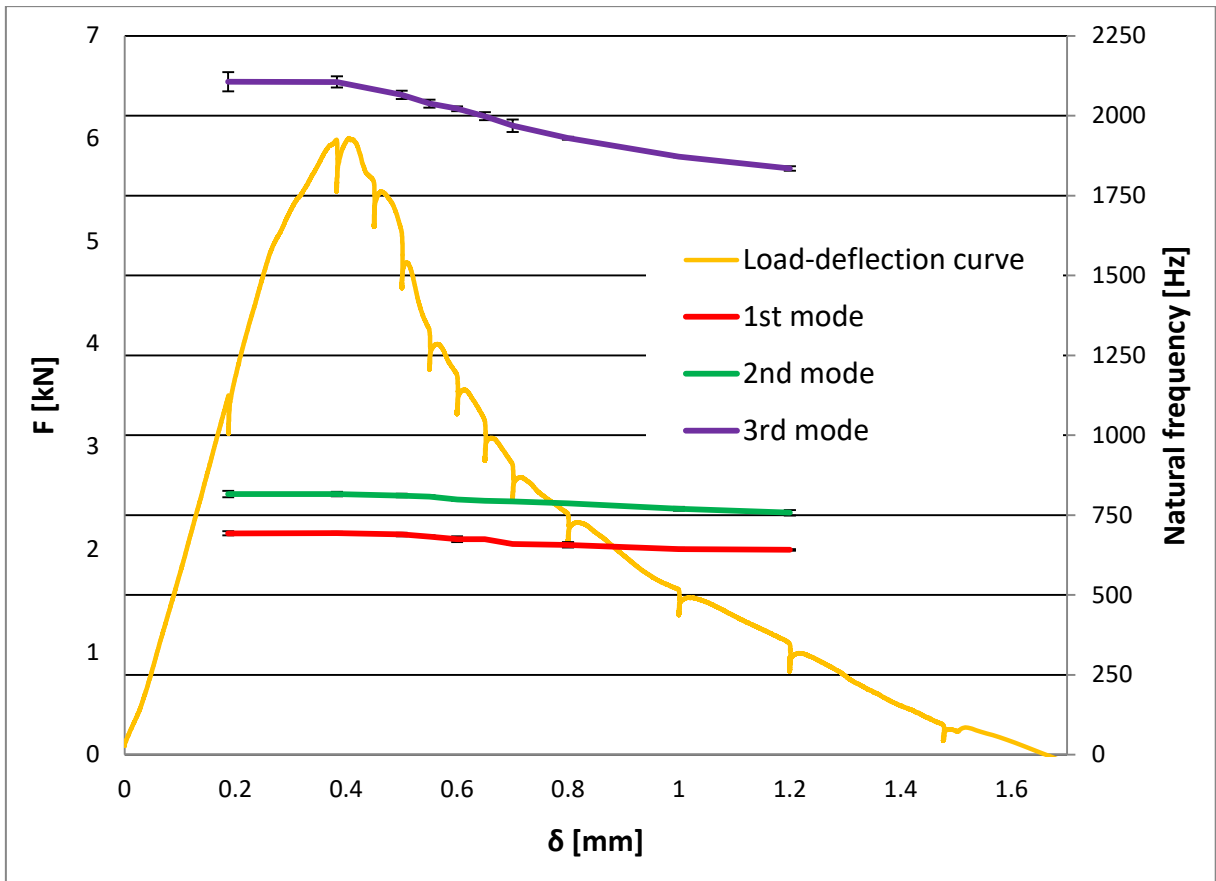


Figure 2.54: Experimentally evaluated decrease of the first three natural frequencies of the 40 cm specimen with the imposed vertical displacement during Test\_400\_3

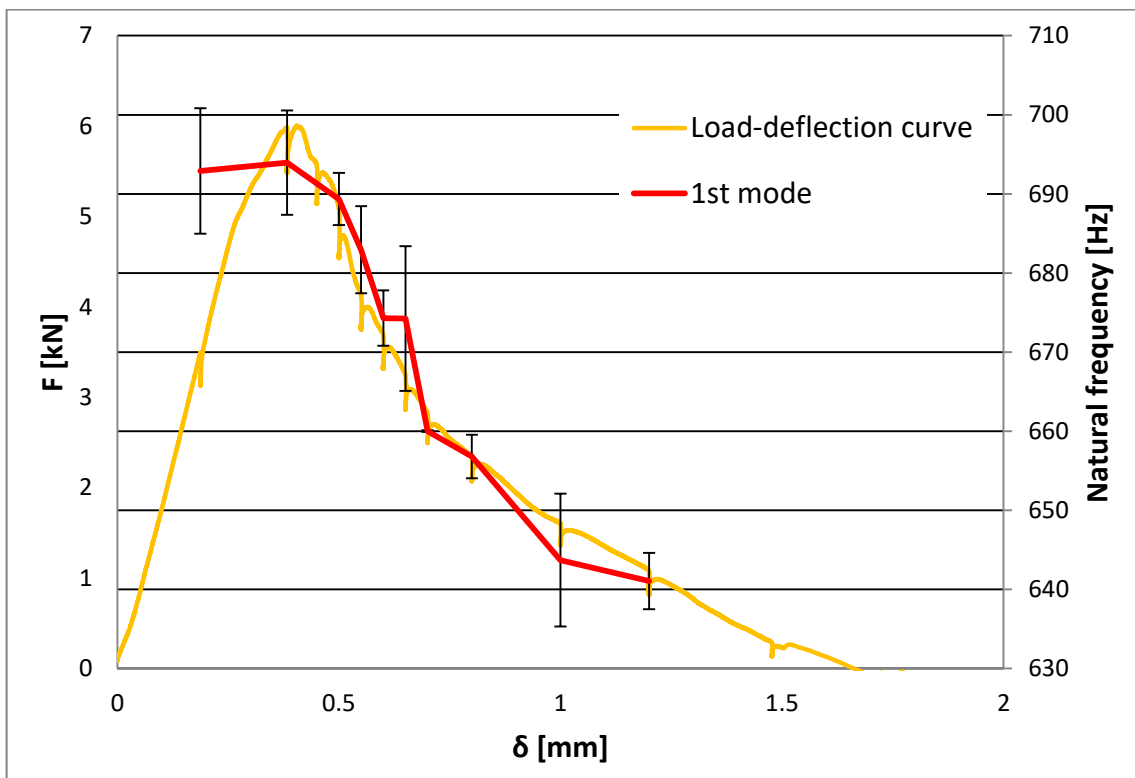


Figure 2.55: Experimentally evaluated decrease of the first natural bending frequency of the 40 cm specimen during Test\_400\_3

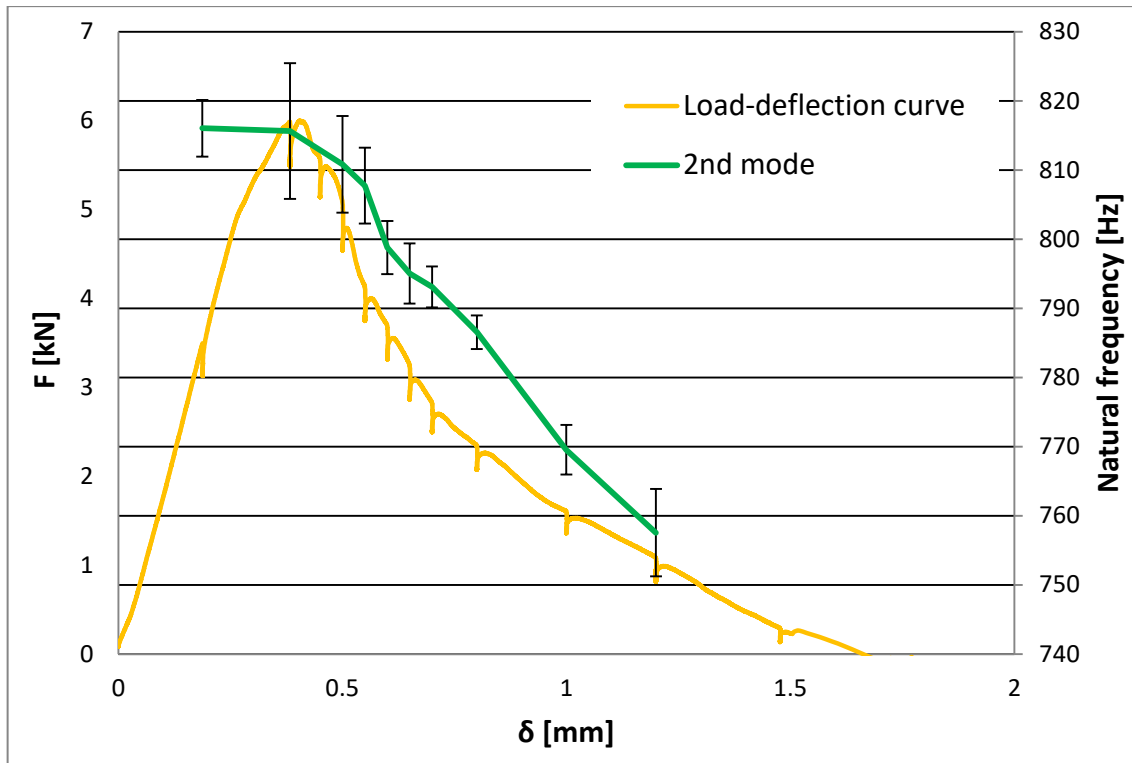


Figure 2.56: Experimentally evaluated decrease of the second natural bending frequency of the 40 cm specimen during Test\_400\_3

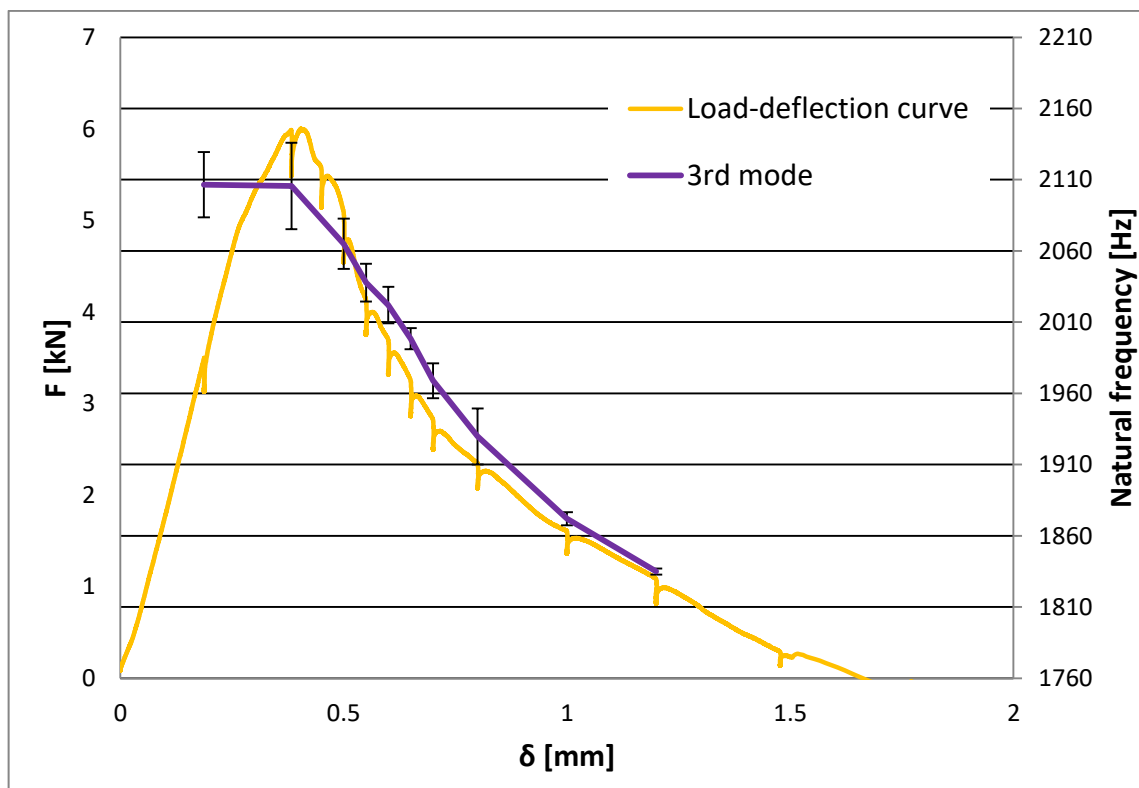


Figure 2.57: Experimentally evaluated decrease of the third natural bending frequency of the 40 cm specimen during Test\_400\_3

In this case an acquisition of the free response signals was made also before the peak load; it is evident, however, that the natural frequencies in that step are practically the same of the ones measured in correspondence of the peak load.

### 2.4.3 Correlations between the two monitoring techniques

In Figure 2.60 and Figure 2.61 a correlation between AEs and natural frequency variation is proposed, respectively for 10 cm and 40 cm specimens. In Figure 2.58 and in Figure 2.59 are represented the load and cumulated AE energy vs. displacement diagrams respectively for Test\_100\_2 and Test\_400\_3, since they were not presented in Section [2.4.1].

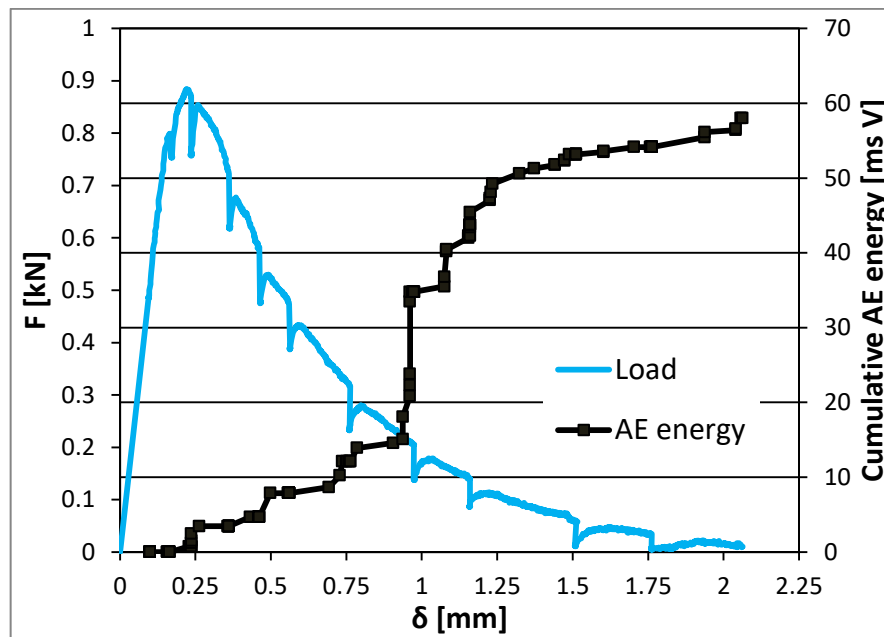


Figure 2.58: Load and cumulated AE energy vs. time diagrams for 10 cm specimen (Test\_100\_2)

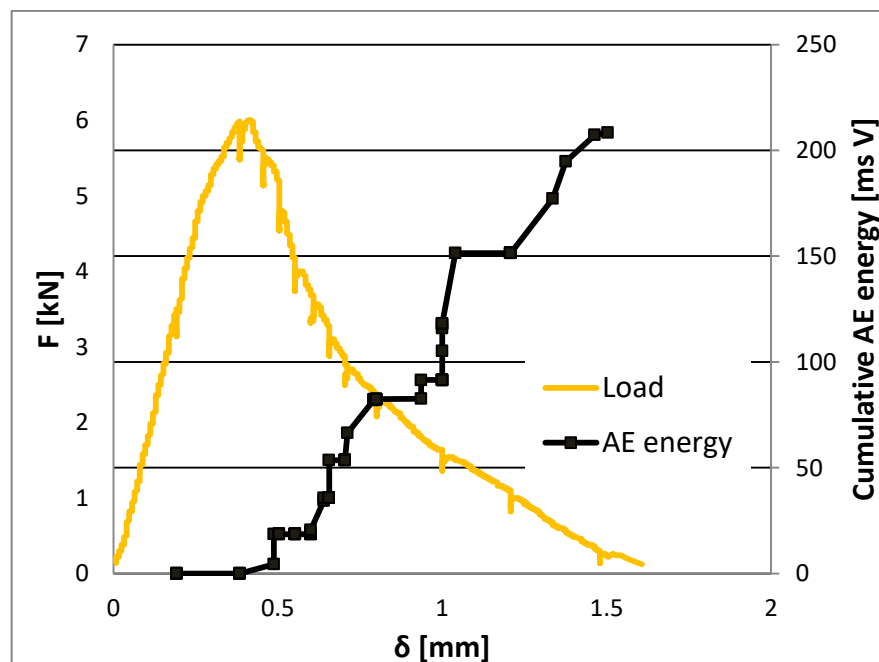


Figure 2.59: Load and cumulated AE energy vs. time diagrams for 40 cm specimen (Test\_400\_3)

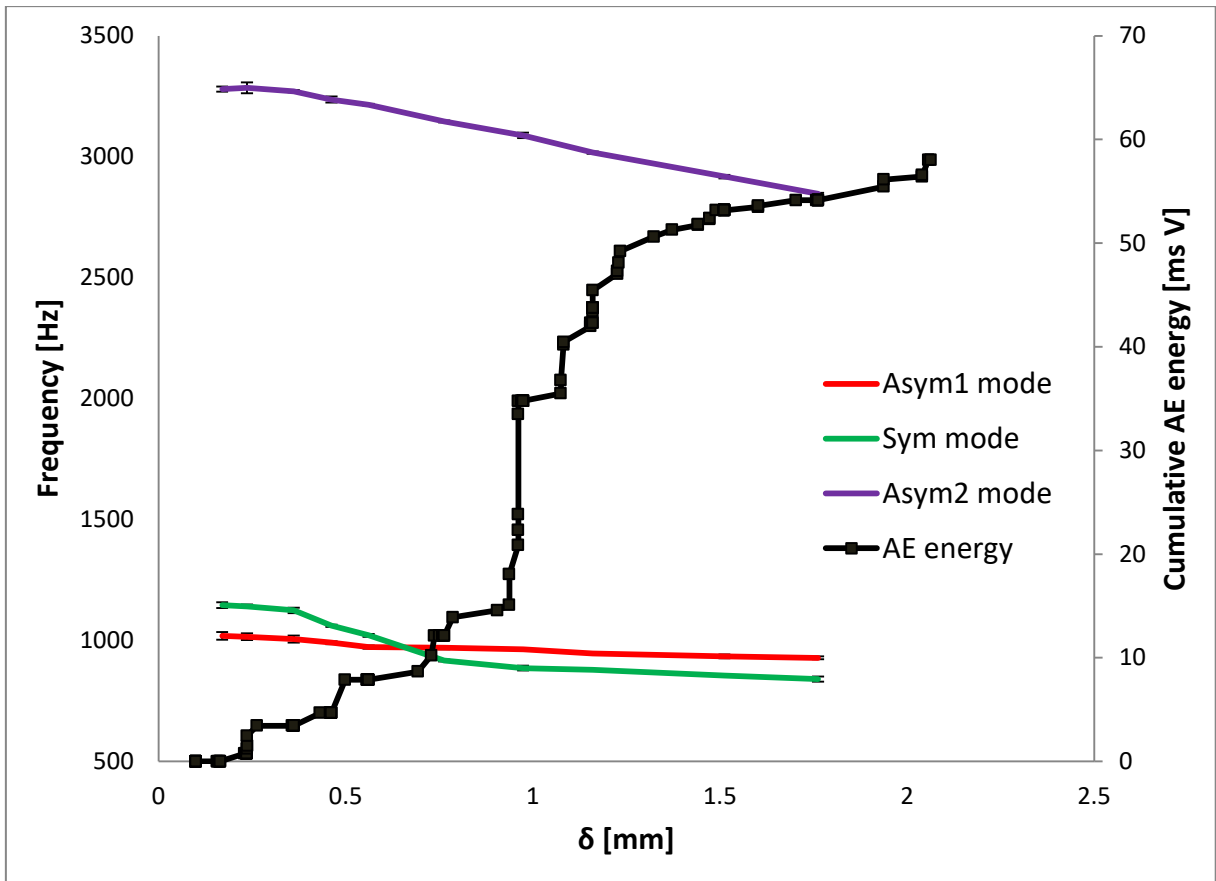


Figure 2.60: Experimental natural frequencies and AE energy vs. displacement in Test\_100\_2 ( $D = 10\text{ cm}$ )

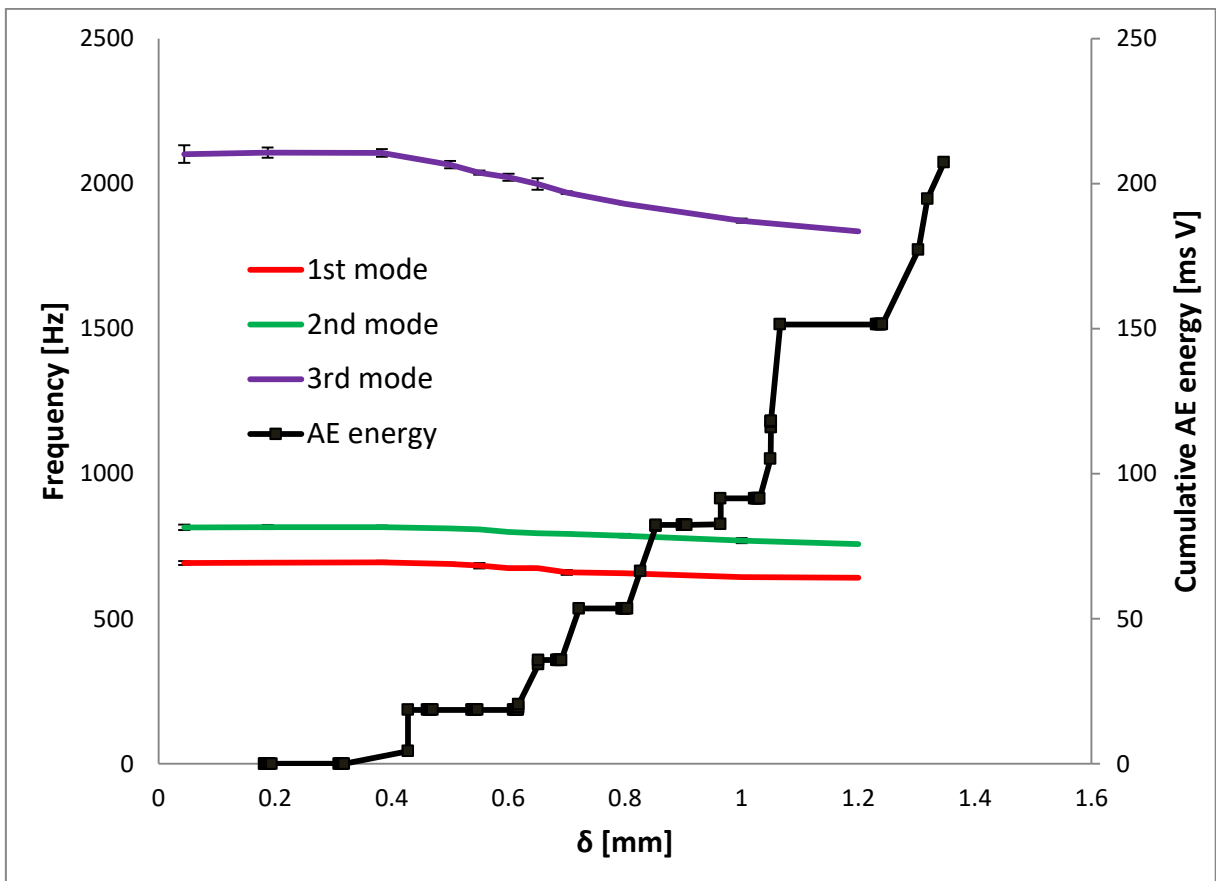


Figure 2.61: Experimental natural frequencies and AE energy vs. displacement in Test\_400\_3 ( $D = 40\text{ cm}$ )

It is evident that, as the damage progresses, the cumulated AE energy increases while the natural frequencies decrease. These two parameters are used in the present work as two independent damage indicators: AEs related to the emitted energy due to the crack formation and propagation in the bulk of material, and the modal frequency variations related to the loss in stiffness due to the crack propagation and cross-section reduction.

However, these two non-destructive techniques can be combined in the practical situations concerning the damage monitoring of full-scale structures: AE signal analysis is available as damage precursor and alarm instrument, while the analysis of the variations in modal parameters can be used to recognize a decrease of the structural global stiffness and to evaluate the damage severity by inverse procedure. A possible combined system of damage monitoring is described in the article by Lacidogna, Piana, Carpinteri (2017):

- installation of AE and DI sensors on the structure;
- evaluation of the most important natural frequencies of the integer structure;
- identification of possible variations in natural frequencies or localizations in modal curvature with periodical acquisition of the dynamic response of the structure, especially when many AE signals are captured;
- implementation of a numerical (e.g., FEM) model of the damaged structure in order to determine, by an inverse procedure, the damage level, knowing the decrease of natural frequencies.

## 2.5 Comparison between three and four point bending results

In the article by Lacidogna, Piana, Carpinteri (2017), four-point bending tests are considered, on specimens with a depth of 10 cm and the same geometrical and material properties of the specimens used for the present thesis. In Figure 2.62 the three load-deflection curves obtained in these tests are represented in dimensionless form (dividing the loads by the peak value of one test, and the displacements for the value in correspondence of the peak of the same test); they are superimposed on the load-displacement curves of two TPB tests analysed in the present thesis (Test\_100\_1 and Test\_100\_2), also represented in dimensionless form (using the same criteria).

In both kinds of tests, the failure of specimens was reached due to plastic collapse and not unstable crack propagation. In other words, the final rupture occurred due to the overcoming of the tensile strength, and not due to the overcoming of the fracture toughness ( $K_{IC}$ ). Nevertheless, observing the dimensionless load-deflection curves of Figure 2.62, it is clear that the four-point bending tests manifested a more brittle behaviour with respect to the TPB ones. In two of the three performed tests, in fact, a global snap-back instability occurred after the peak-load. It can be explained also by using the LEFM concepts presented in Section [1.1.1.1]: in the elastic phase of the tests, the stress intensity factor calculated for four-point bending tests (Eq.(1.10)

and Eq.(1.12)) is (for the same load value) lower than the stress intensity factor evaluated for TPB tests (Eq.(1.10) and Eq.(1.11)).

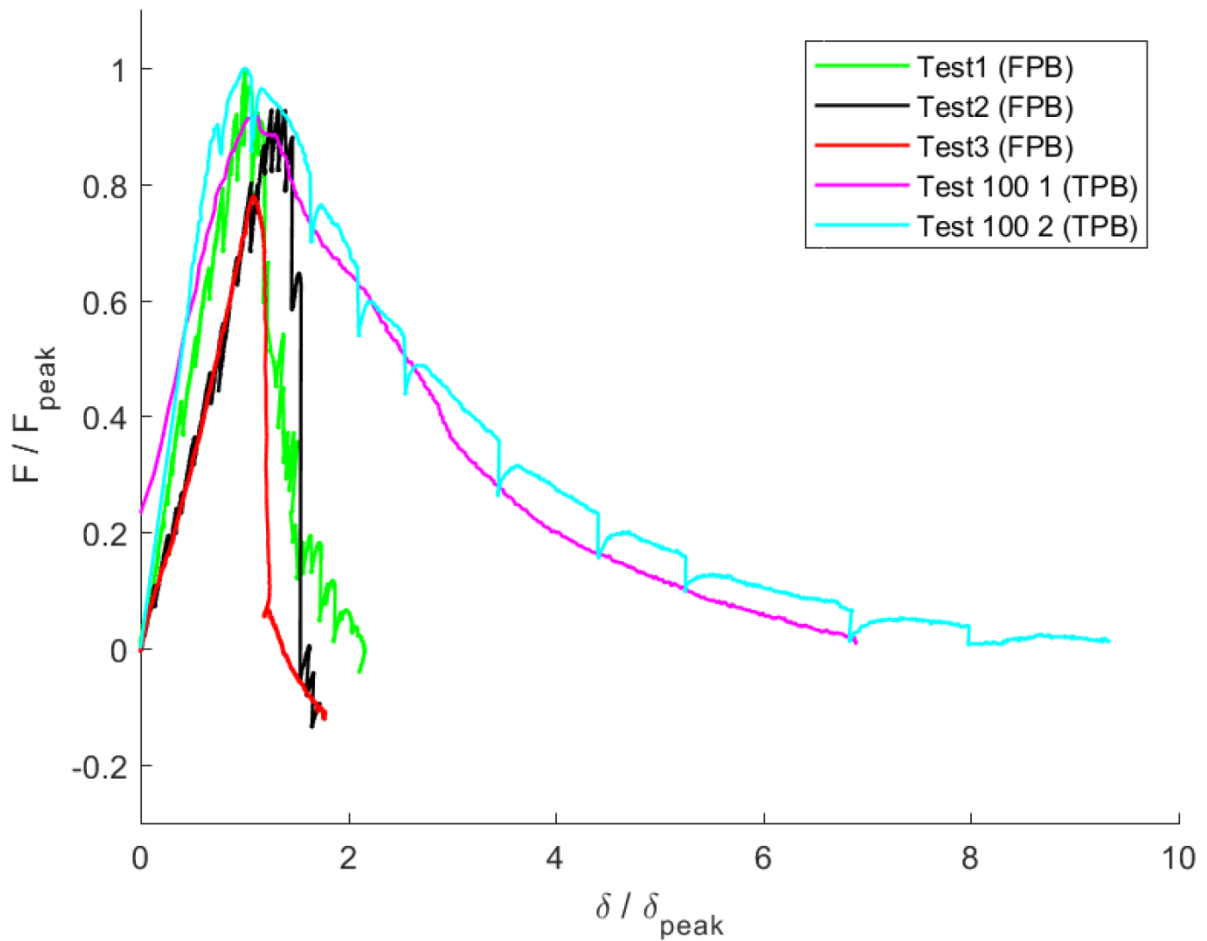


Figure 2.62: Comparison between the dimensionless load-displacement curves obtained in three and four-point bending tests on 10 cm specimens

A final observation concerns the Dynamic Identification. The reduction of natural frequencies with the damage progress in four-point bending test (Lacidogna, Piana, Carpinteri, 2007) is greater than the decreases measured in three-point bending tests (Section [2.4.2]). It happens because the section in which the crack occurs is free to vibrate in the case of four-point bending, while it is bounded in TPB tests.

## Conclusions

Three-point bending tests on plain concrete pre-notched specimens were performed in this work. Four different specimen sizes were considered, in order to investigate the scale effects on the material fracture energy and bending strength.

In addition, two non-destructive damage monitoring techniques were used during TPB tests: Acoustic Emission (AE) and Dynamic Identification (DI). The geometric characteristics of the specimens and the testing procedure were chosen according to RILEM TC 50 – FMC. This Recommendation provides an experimental method for the evaluation of the fracture energy of plain concrete.

Two mono-fractal scaling laws, proposed by Carpinteri and his collaborators, were applied to interpret the experimental results concerning the fracture energy and the bending strength.

Considering also kinematic aspects and, in particular, the scale effects on the critical rotation angle, a scale-independent cohesive law was determined for bending problem. This law is a function of the three renormalized values of fracture energy, bending strength and critical rotation angle, and it represents the true material property.

This law can be considered as an extension of the fractal cohesive laws already obtained in the case of uniaxial tensile tests (Carpinteri, Chiaia Cornetti, 2002) and uniaxial compression tests (Carpinteri, Corrado, 2009).

A further fractal scaling law was proposed in this work for the AE energy per unit area. Unlike the fracture energy, which is released on an invasive fractal domain, the AE energy resulted to be released on a lacunar fractal domain.

Finally, the advantages of the combined use of AE and DI techniques in the monitoring of full-scale structures are remarked. While the AE analysis provides damage precursor data and represents a useful alarm instrument, the DI analysis concerning the modal frequency variations allows to evaluate reductions in global rigidity of the structure and, by inverse procedure, the damage entity. In this work, an estimate of the crack advancement under loading was obtained by comparing the material frequencies measured in the lab with those obtained by a finite element model.

## References

- Barenblatt, G.I. (1959) "The formation of equilibrium cracks during brittle failure, general ideas and hypothesis, axially symmetric cracks", *Journal of Applied Mathematics and Mechanics*, **23**(3):622-636.
- Bažant, Z.P. (1984) "Size effect in blunt fracture: concrete, rock, metal", *ASCE Journal of Engineering Mechanics*, **110**:518-535.
- Bažant, Z.P. (1997) "Scaling of quasibrittle fracture: Asymptotic analysis", *International Journal of Fracture*, **83**(1):19-40.
- Bažant, Z.P., and Planas J., (1998) *Fracture and Size Effect in Concrete and Other Quasibrittle Materials*, CRC Press, Boca Raton.
- Bažant, Z.P. et al. (2004) "Quasibrittle fracture scaling and size effect", Final Report, *Material and Structures (RILEM TC QFS)*, **37**:547-568.
- Carpinteri, A. (1989a) "Post-peak and post-bifurcation analysis of cohesive crack propagation", *Engineering Fracture Mechanics*, **32**:265-278.
- Carpinteri, A. (1989b) "Size effects on strength, toughness and ductility", *Journal of Engineering Mechanics (A.S.C.E.)*, **115**:1375-1392, New York.
- Carpinteri, A. (1989c) "Softening and snap-back instability in cohesive solids", *International Journal for Numerical Methods in Engineering*, **28**:1521-1537, England.
- Carpinteri, A. (1989d) "Cusp catastrophe interpretation of fracture instability", *Journal of the Mechanics and Physics of Solids*, **37**:567-582, Great Britain.
- Carpinteri, A. (1989e) "Decrease of apparent tensile and bending strength with specimen size: Two different explanation based on fracture mechanics", *International Journal of Solids and structures*, **25**:407-429.
- Carpinteri, A. (1992) *Meccanica dei materiali e della frattura*, Pitagora Editrice, Bologna.
- Carpinteri, A. (1994a) "Fractal nature of material microstructure and size effects on apparent mechanical properties", *Mechanics of Materials*, **18**:89-101.
- Carpinteri, A. (1994b) "Scaling laws and renormalization groups for strength and toughness of disordered materials", *International Journal of Solids and Structures*, **31**:291-302.
- Carpinteri, A. (1998) *Dinamica delle strutture*, Pitagora Editrice, Bologna.
- Carpinteri, A., Accornero, F. (2018) "Multiple snap-back instabilities in progressive microcracking coalescence", *Engineering Fracture Mechanics*, **187**:272-281.

- Carpinteri, A., Chiaia, B. (1997) "Multifractal scaling laws in the breaking behaviour of disordered materials", *Chaos, Solitons & Fractals*, **8**:135-150.
- Carpinteri, A., Chiaia, B., Cornetti, P. (2002) "A scale-invariant cohesive crack model for quasi-brittle materials", *Engineering Fracture Mechanics*, **69**:207-217.
- Carpinteri, A., Chiaia, B., Ferro, G. (1995) "Size effects on nominal tensile strength of concrete structures: Multifractality of material ligaments and dimensional transition from order to disorder", *Material and Structures*, **28**:311-317.
- Carpinteri, A., Colombo, G. (1989) "Numerical analysis of catastrophic softening behaviour (snap-back instability)", *Computers & Structures*, **31**:607-636.
- Carpinteri, A., Corrado, M. (2009) "An extended (fractal) Overlapping Crack Model to describe crushing size-scale effects in compression", *Journal of Engineering Failure Analysis*, **16**:2530-2540.
- Carpinteri, A., Corrado, M., Paggi, M., Mancini, G. (2007) "Cohesive versus overlapping crack model for a size effect analysis of RC elements in bending", *Proceedings of the 6<sup>th</sup> international FraMCoS conference*, Catania, Italy 2007, vol.2, London: Taylor & Francis, 655-663.
- Carpinteri, A., Ferro, G. (1994) "Size effects on tensile fracture properties: A unified explanation based on disorder and fractality of concrete microstructure", *Materials and Structures*, **27**:563-571.
- Carpinteri, A., Ferro, G. (1998) "Scaling behaviour and dual renormalization of experimental tensile softening responses", *Material and Structures*, **31**:303-309.
- Carpinteri, A., Lacidogna, G., (2008) *Acoustic Emission and Critical Phenomena from Structural Mechanics to Geophysics*, Taylor & Francis.
- Carpinteri, A., Lacidogna, G., Corrado, M., Di Battista, E., (2016) "Cracking and crackling in concrete-like materials: A dynamic energy balance", *Engineering Fracture Mechanics*, **155**:130-144.
- Carpinteri, A., Lacidogna, G., Pugno, N. (2005) "Time-scale effects during damage evolution: A fractal approach based on acoustic emission", *Strength, Fracture and Complexity*, **3**:127-135.
- Chaia, B. (1995) "Influenza del disordine microstrutturale sulle proprietà meccaniche dei materiali eterogenei", PhD. Thesis, Scuola di Dottorato, Politecnico di Torino.
- Cornetti, P. (1998) "Frattali e calcolo frazionario nella meccanica dei solidi danneggiati", PhD. Thesis, Scuola di Dottorato, Politecnico di Torino.
- D.M. 14/01/2008 (2008) "Norme Tecniche per le Costruzioni", *Gazzetta Ufficiale della Repubblica Italiana*, 04/02/2008, n.29, S.O. n. 30 (in Italian).

- Duan, K., Hu, X.Z., Wittmann, F.H. (2002) "Explanation of size effect in concrete fracture using non-uniform energy distribution", *Materials and Structures*, **35**:326-331.
- Dugdale, D.S. (1960) "Yielding of steel sheets containing slits", *Journal of the Mechanics and Physics of Solids*, **8**: 100-104.
- Ferro, G. (1994) "Effetti di scala sulla resistenza a trazione dei materiali", PhD. Thesis, Scuola di Dottorato, Politecnico di Torino.
- Griffith, A.A. (1921) "The phenomena of rupture and flow in solids", *Philosophical Transaction of the Royal Society*, **A221**:163-198, London.
- Grosse, C., Ohtsu, M. (2008) *Acoustic Emission Testing*, Springer, Berlin.
- Guinea, G.V., Planas, J., Elices, M. (1992) "Measurement of the fracture energy using three-point bend tests: Part 3-Influence of cutting the P- $\delta$  tail", *Materials and Structures*, **25**:327-334.
- Hillerborg, A. (1984) "Additional concrete fracture energy tests performed by 6 laboratories according to a draft RILEM recommendation". (Report TVBM; Vol. 3017), Division of Building Materials, LTH, Lund University.
- Hillerborg, A., (1983) "Concrete fracture energy tests performed by 9 laboratories according to a draft RILEM recommendation: Report to RILEM TC50-FMC", *Lund Institute of Technology, Division of Building Materials*, Report TVBM-3015.
- Hillerborg, A., Modéer, M. and Petersson, P.E. (1976) "Analysis of crack formation and crack growth in concrete by means of fracture mechanics and finite elements", *Cement & Concrete Research*, **6**:773-782.
- Hu, X.Z., Wittmann, F.H. (1992) "Fracture energy and fracture process zone", *Materials and Structures*, **25**:319-326.
- Inglis, C.E., (1913) "Stresses in a plate due to the presence of cracks and sharp corners", *Transaction of the Royal Institution of Naval Architects*, **60**:219-241, London.
- Irwin, G.R. (1960) "Plastic zone near a crack and fracture toughness", *Proceedings of the 7<sup>th</sup> Sagamore Conference*, IV-63.
- Karihaloo, B.L., Abdalla, H.M., Imjai, T. (2003) "A simple method for determining the true specific fracture energy of concrete", *Magazine of Concrete Research*, **55**:471-481.
- Kirsch, G., (1898) "Die Theorie der Elastizität und die Bedürfnisse der Festigkeitslehre", *V.D.I.*, **42**:797-807.
- Kleiser, T., Bocek, M. (1986) "The fractal nature of slip in crystals", *Z. Metallkd*, **77**:582-587.

- Lacidogna, G., Piana, G., Carpinteri, A., (2017) "Acoustic Emission and Modal Frequency Variation in Concrete Specimens under Four-Point Bending", *Applied Sciences*, **7**, 339.
- Leicester, R.H. (1969) "The size effect of notches", in Proc. 2<sup>nd</sup> Australasian Conf. on Mech. of Struct. Mater., Melbourne, 4.1-4.20.
- LUSAS. *User Reference Manual (Version 15.1)*; Finite Element Analysis Ltd.: Kingstone upon Thames, UK, 2015.
- Mandelbrot, B.B. (1982) *The Fractal Geometry of Nature*, W.H. Freeman and Company, New York.
- Muralidhara, S., Raghu Prasad, B.K., Hamid Eskandari, Karihaloo, B.L. (2010) "Fracture process zone size and true fracture energy of concrete using acoustic emission", *Construction and Building Materials*, **24**:479-486.
- Muralidhara, S., Raghu Prasad, B.K., Singh, R.K. (2013) "Size independent fracture energy from fracture energy release rate in plain concrete beams", *Engineering Fracture Mechanics*, **98**:284-295.
- Mariotte, E. (1686) *Traité du mouvement des eaux*, Posthumously edited by M. de la Hire, Engl. transl. by J.T. Desvaguliers, London (1718), p. 249.
- Peirce, F.T. (1926) "Tensile strength of cotton yarns", *Journal of the Textile Institute*, **17**:355-368.
- Petersson, P.E. (1981) "Crack growth and development of fracture zones in plain concrete and similar materials", Division of Building Materials, LTH, Lund University.
- RILEM Technical Committee 50-FMC (1985) "Determination of the fracture energy of mortar and concrete by means of three-point bend tests on notched beams", Draft Recommendation, *Materials and Structures*, **18**:287-290.
- RILEM Technical Committee 212-ACD (2010) "Acoustic emission and related NDE techniques for crack detection and damage evaluation in concrete: Measurement method for acoustic emission signals in concrete", *Materials and Structures*, **43**:1177-1181.
- Ruotolo, R. (1997) "Tecniche basate sulle vibrazioni per l'identificazione del danno strutturale", PhD. Thesis, Scuola di Dottorato, Politecnico di Torino.
- Tada, H., Paris, P.C., Irwin, G. (1985) *The Stress Analysis of Cracks*, Paris Productions Incorporated (and Del Research Corporation), St. Louis, Missouri.
- Walsh, P.F. (1972) "Fracture of plain concrete", *Indian Concrete Journal*, **46**:469-470 and 476.

Weibull, W. (1939) "A statistical theory of the strength of materials", *Proceedings of the Royal Swedish Institute for Engineering Research*, **153**:1-55.